PFC/RR-89-2 DOE/ET-51013-264

Radial Ion Transport in a Nonaxisymmetric Magnetic Mirror

Daniel L. Goodman

February, 1989

Plasma Fusion Center
Massachusetts Institute of Technology
Cambridge, Massachusetts 02139 USA

Radial Ion Transport in a Nonaxisymmetric Magnetic Mirror

by

Daniel Lawrence Goodman

B.S.E., Princeton University (1982)

Submitted to the Department of Physics
in partial fulfillment of the requirements for the degree of

Doctor of Philosophy

at the

MASSACHUSETTS INSTITUTE OF TECHNOLOGY

June 1989

Signature of Author .....
Department of Physics
February 15, 1989

Certified by .....
Richard S. Post
Senior Research Scientist, Plasma Fusion Center
Thesis Supervisor

Accepted by .....
George Koster
Chairman, Departmental Graduate Committee

Radial Ion Transport in a Nonaxisymmetric Magnetic Mirror

by

Daniel Lawrence Goodman

Submitted to the Department of Physics
on February 15, 1989, in partial fulfillment of the
requirements for the degree of
Doctor of Philosophy

Abstract

An experimental study of radial ion transport in a nonaxisymmetric magnetic mirror is presented. It is found that the ion confinement time perpendicular to the magnetic field is an order of magnitude shorter than predicted by classical and neoclassical theories, and that radial transport can be the dominant ion loss mechanism.

Transport experiments are performed in hydrogen, helium and argon plasmas by measuring equilibrium radial profiles of plasma density, ionization source, end loss current, electric field, electron temperature and ion temperature. The radial profiles of the perpendicular diffusion coefficient ($D_\perp$) are presented, and range from a radial average of $\simeq 5 \times 10^3$ cm^2/sec for hydrogen to $\simeq 2 \times 10^4$ cm^2/sec for argon. These coefficients are a factor of ten larger than the maximum possible classical and neoclassical diffusion coefficients in all three gasses.

The effect of low frequency RF power in the ion cyclotron frequency range on the radial ion transport rate is also investigated. RF power increases the ion perpendicular transport, which then becomes the dominant loss mechanism. With sufficient RF power, the ion perpendicular loss rate exceeds the ionization source, with a resultant loss of plasma equilibrium. Application of RF power increases the radial transport rate of plasmas with resonant ions, which are also heated by the RF waves, as well as plasmas whose ion cyclotron resonance is not inside the confinement region. The increased transport rate during application of RF power shows up as an increased $D_\perp$. This indicates that the radial ion transport is due to a direct interaction between the ions and the RF field, rather than to radial profile changes or the enhanced ambipolar potential which are other RF effects. The effect of RF power on plasma potential is also studied, and is shown to be an electron effect, whose power scaling is consistent with theory.

Thesis Supervisor: Richard S. Post
Title: Senior Research Scientist, Plasma Fusion Center

Acknowledgements

I would like to thank my thesis adviser, Dr. Richard S. Post for overseeing the work performed in this thesis. He has taught me to to make careful experimental measurements, and not believe the results until all the details seem consistent. I have learned a great deal from Dr. Post.

I also thank Dr. Donna Smatlak, the leader of the Constance group and an experienced experimentalist, for her advice and guidance throughout this study.

TARA scientists who made helpful experimental or theoretical suggestions include Drs. Michael Gerver, Jim Irby, Jay Kesner, Barton Lane and Don Smith. I also wish to thank Professors Ron Davidson and Miklos Porkolab for serving on my thesis committee.

My colleague and friend Craig Petty deserves special thanks. As the two graduate students studying ion physics on Constance, we have collaborated on a variety of experimental and theoretical projects. Craig also built and operated several of the diagnostics used in this thesis.

I am also grateful to the other present and former graduate students who made working in the Constance group more enjoyable. They include Xing Chen, Tom Farish, Rich Garner, Gerald Gibson, Sam Hokin and Ling Wang.

I also thank my parents, Mr. Irving and Mrs. Mildred Goodman, who taught me the importance of education, hard work and a desire for understanding.

My good friends Michael Tsuk and Elana Doering have been a source of support and help throughout this endeavor, and also deserve thanks.

The Fannie and John Hertz Foundation provided financial support for this thesis. Additional support came from the U.S. Department of Energy under contract DE–AC02–78ET51013.

Contents

List of Figures

List of Tables

List of Symbols

a	Density Normalization ($10^{13} cm.^{-3}$)
B(x,y)	Emission brightness ($cm.^{-3}\ s.^{-1}$)
B	Magnetic field (kG.)
B_0	Midplane magnetic field (kG.)
b	Unit vector along **B**
C_B	Magnetic field fanning factor
D	Radial diffusion coefficient ($cm.^2\ s.^{-1}$)
D_{cl}, D_{nc}	Classical and neoclassical diffusion coefficients ($cm.^2\ s.^{-1}$)
D_{max}	Sum of classical and neoclassical diffusion coefficients ($cm^2\ s.^{-1}$)
Δr	Radial ion excursion due to geodesic curvature (cm.)
η	Normalized RF power (dimensionless)
Γ	Radial ion flux ($cm.^{-2}\ s.^{-1}$)
I/P	Ionizations per photon emission (dimensionless)
$\mathcal{J}$	Parallel adiabatic invariant (cm. C. s. kG.)
J	Ion end loss current density (mA./$cm.^2$)
κ	Magnetic field line curvature (cm^{-1})
L_B	Magnetic scale length (cm.)
L_p	Plasma length (cm.)
L_s	Ion bounce length (cm.)
m	Ion mass (g.)
μ	Radial mobility coefficient ($cm^2\ V^{-1}\ s.^{-1}$) , or Magnetic moment (kG. cm^2)
n, n_i, n_0	Electron, ion and neutral densities (cm^{-3})

$\bar{n}$	Density integrated along magnetic field line (cm^{-2})
$nl_{\perp}$	Line density, perpendicular to magnetic axis ($cm.^{-2}$)
$\mathcal{N}$	Dimensionless integral $1.25 < \mathcal{N} < 1.75$
ν_{eff}	Effective ion collision frequency ($s.^{-1}$)
ω_c	Ion cyclotron frequency ($s.^{-1}$)
P	Gauge pressure (Torr.)
P_{ECH}	ECH frequency microwave power (kW.)
ϕ	Plasma potential (V.)
ϕ_0	Electron confining potential (V.)
ϕ_1	Potential dip (V.)
ψ	Radial flux function (cm^2)
Ψ	Normalized potential ϕ_0/T_{ec} (dimensionless)
R	Magnetic mirror ratio (dimensionless)
r	Radial coordinate at midplane (cm.)
ρ_i	Ion Larmor radius (cm.)
S'	Volume ionization source function ($mA./cm^3$)
S	Line average ionization source function ($mA./cm^2$)
$< \sigma v >_{exc}$	Distribution averaged excitation cross section ($cm^3\ s.^{-1}$)
T_{ec}, T_i	Cold electron and ion temperatures (eV.)
$\tau_{\perp}$, $\tau_{\parallel}$	Perpendicular and parallel ion confinement times (s.)
τ_{ii}	Ion–ion 90 degree scattering time (s.)
θ	Azimuthal coordinate at the midplane (radians)
$v_{\parallel}$, $v_{\perp}$	Parallel and perpendicular ion velocities ($cm./s.$)
$\mathcal{A}$	Normal field line curvature (dimensionless)
IO	Geodesic field line curvature (cm^{-1})
Z	Geometrical axis coordinate (cm.)
Z_{avg}^{in}, Z_{avg}^{end}	Average ion charge states in plasma or end loss (dimensionless)

Chapter 1

Introduction

1.1 Problem Statement

In an open magnetic geometry such as the magnetic mirror, particle confinement has historically meant confinement along field lines. Unless the axial particle losses are "plugged" using potentials or by some other scheme, particle loss along field lines dominates over transport radially outward across the magnetic field. With the introduction of electrostatic end plugging in the tandem mirror, [Dimov, et al., 1976, Fowler, et al., 1977] axial loss rates were reduced to the point where radial transport became an important particle loss mechanism. A similar plugging scheme, applicable to single cell mirrors, uses hot magnetically confined electrons to create a potential dip and electrostatically confine ions [Baldwin, 1980]. This method is successfully used in the Constance B mirror, increasing the ion parallel lifetime by more than an order of magnitude.

With longer parallel lifetimes, ions have the opportunity to transport radially before being lost axially. These radial ion fluxes provide both a motivation and an opportunity. It is not exaggerating to say that control of particle losses perpendicular to the magnetic field is the central problem in magnetically confined plasma research. Despite the importance of the subject, there have been few experiments which measure loss rates and transport coefficients in a way that allow comparison

with theory.

This thesis is the first careful experimental study of radial transport in a nonaxisymmetric mirror in which all of the relevant radial plasma profiles are measured and the transport coefficients and their radial dependence deduced.

Many different plasma processes lead to radial particle transport. Particle collisions and orbit effects lead to radial ion diffusion. A major goal of this thesis is to test these classical and neoclassical transport theories and see if they adequately predict the observed ion radial transport in Constance.

A primary method of heating plasma ions is application of RF power near the ion cyclotron frequency. Experimenters have often noticed that degraded energy and particle confinement occur during ion cyclotron heating (ICH). Various theories have been proposed to explain the effect of low frequency RF waves on radial ion transport. Another important goal of this thesis is to measure the effect of low frequency applied RF power on ion radial transport.

This thesis has several subsidiary goals. Various auxiliary measurements of plasma profiles are required as pieces of the overall transport experiment. These measurements are themselves interesting and are also useful for others working on similar projects on Constance and elsewhere. Providing this information, including details of novel experimental methods and models which are needed to measure the various quantities, is a secondary goal of this thesis.

The application of low frequency RF power produces a variety of plasma effects. Describing these effects and comparing them to various theories about the interaction of plasmas with RF waves is also a secondary goal of this thesis.

1.2 Previous Work

Many of this experimental measurements in this thesis are similar to measurements done at Lawrence Livermore Laboratory on the TMX-U tandem mirror. By using an absolutely calibrated camera to measure light at 6961 $\AA$ (hydrogen H_α line), Allen

and coworkers inferred the radial and axial positions at which atoms are ionized [Allen, et al., 1987]. By combining this information with the axially directed ion current at the end wall, they made the first measurement of the ambipolar component of the radial ion flux. This is a difficult measurement because unlike the nonambipolar component, ambipolar transport causes no net electrical current to flow to the end wall, as the ions move radially with their neutralizing electron counterparts. In these experiments, Allen found that the ambipolar current is smaller than the nonambipolar current in the plasma core.

These measurements built on previous TMX-U transport experiments and on nonambipolar transport measurements in other tandem mirrors. Hooper and colleagues used segmented end wall plates to measure the net current in the end loss [Hooper, et al., 1985]. They found nonambipolar confinement times in the range from one to 100 ms depending on parameters. Their results were presented as scaling laws using density or central cell potential as the independent parameter.

Because they did not measure the radial profiles of either potential or density, modelling the data and comparison with theory proved difficult. Instead they assumed parabolic profiles for density, temperature and potential and claimed agreement within a factor of five with resonant neoclassical transport theory. They also modelled the data with an *ad hoc* ϕ^{-2} law which was a better fit to the data, and was used in numerical computations. (The ϕ used for scaling was the plasma potential in the central cell.)

End wall plates were also used in several other devices to measure nonambipolar radial transport. GAMMA 10 in Tsukuba, Japan used end wall plates connected to ground through variable resistors to simultaneously change the central cell plasma potential and modify the nonambipolar loss rate [Cho, et al., 1986]. They found perpendicular confinement times of 10 ms to 1 s depending on end wall termination resistance, and claimed that the scaling of perpendicular confinement time with potential agreed with neoclassical theory. They modelled their potential profile using a transport code which assumed classical and neoclassical forms for the transport

coefficients.

Earlier work at Livermore also used end wall plates to collect the net current [Drake, et al., 1982]. The 80 $\pm$ 40 A. of negative net current flowing from the core plasma to the end wall implies a very large nonambipolar transport rate, considering that the axial ion current from the same volume is only 100 A. They believed that the measured nonambipolar radial flux was of the same order, with large uncertainties.

Measurements of transport have also been made in the two other U. S. mirror machines: TARA at M. I. T. and Phaedrus at the University of Wisconsin. The ionization source measurements in TARA utilized an absolutely calibrated CCD camera to measure H_α light [Brau, et al., 1988]. These measurements were similar to those done in TMX–U. Substantial radial transport was observed in the TARA central cell even operating in a purely axisymmetric configuration. The axisymmetric operation ruled out neoclassical contributions to the transport, and an inward convective term was required in order to satisfy the observed fueling and loss rates.

Large radial transport rates have also been observed in the Phaedrus Tandem Mirror. End plugging in Phaedrus causes large radial transport in the central cell [Persing, et al., 1988]. They found that the large transport in the edge plasma cannot be explained classically, and postulate that the transport results from $E \times B$ driven convection due to azimuthal asymmetries in the potential structure. The ionization source was measured using a single rotatable light diode with an H_α filter. Unfortunately, this technique made it difficult to know the exact plasma volume being surveyed.

The complexity of these large experiments increases the difficulty of radial transport measurements. In the tandem mirror, the various cells have completely different plasma parameters. The radial transport at one axial location may be primarily due to charge exchange collisions, whereas resonant neoclassical losses may dominate at a different location. Radial transport experiments in smaller machines have produced some very interesting results in systems which are easier to analyze.

For example, Tsushima [Tsushima, et al., 1986] showed that measuring, and even

controlling plasma radial profiles is possible in his axisymmetric mirror at Tohoku University. By applying voltages to three circular concentric segmented electrodes, he convincingly modified both the density and potential profiles. This allowed him to measure the perpendicular ion transport rate as a function of radial electric field. He found that until he modified the plasma profiles, the transport could be explained by ion–neutral collisions and charge exchange. When he steepened the potential gradient density fluctuations appeared, and the ion mobility was enhanced by up to five times the classical value. This result is similar to that seen in the OGRA-3B minimum B mirror at the Kurchatov Institute in Moscow, where the combination or collisions and low frequency fluctuations caused radial particle transport [Putvinskij and Timofeev, 1975,Zhil'tsov, et al., 1979].

The effect of RF power near the ion cyclotron frequency on plasma profiles in mirrors has been studied extensively, although the effect of RF on transport is not as well known. RF power can produce plasmas through ionization, [Okamura, 1986], [Post, 1987] stabilize an axisymmetric mirror configuration against MHD instabilities, [Ferron, et al., 1983] enhance the ambipolar potential, [Hershkowitz, et al., 1985, Smith, et al., 1986] and of course heat ions. Ion transport also accompanies these processes as predicted in tokamaks by several authors, [Whang and Morales, 1983, Riyopoulos, et al., 1986,Chen, 1988] and in mirrors [Myra and Catto, 1982]. Although the approaches to the problem range from single particle models to quasi–linear theory, the common feature of these works is that the calculated diffusion coefficient $D_\perp$ is proportional to $|E_{rf}|^2$.

Enhanced radial transport by RF waves can be caused by several effects. The momentum transferred by the wave to the resonant particles, the change in particle orbits during heating and increased radial particle fluxes due to profile changes all can affect the radial transport rate. One experimental study using a single axisymmetric mirror showed increased loss of ions both axially and radially during application of nonresonant RF power [Kuthi, et al., 1988]. Kuthi believes that enhanced potentials due to the interaction of electrons with the parallel electric field accelerated ions out

of the mirror as well as increasing their radial transport rate. He also blames the azimuthally asymmetric potentials generated by the antenna for causing convective transport.

Theories which predict or explain ion radial transport rates and diffusion coefficients differ in details but have one basic premise in common. Somehow stochasticity is introduced to break the constancy of the parallel adiabatic invariant $\mathcal{J}$ and allow particles to move radially. Particle collisions are a stochastising agent and combine with a finite ion gyroradius to produce classical diffusion [Chen, 1974]. Geodesic curvature leads to radial excursions off flux surfaces, and when combined with collisions leads to neoclassical transport [Ryutov and Stupakov, 1978]. If the drift and bounce frequencies are similar, orbital resonances occur which lead to the loss of particles near resonance. Even without collisions, stochasticity is achieved in this Hamiltonian system in the vicinity of orbital resonances in velocity space [Lieberman and Lichtenberg, 1983]. These ideas were extended by other authors, [Lee, 1978,Cohen, et al., 1979,Myra and Catto, 1982] producing the analytical neoclassical model used in this thesis.

A completely different type of transport mechanism, convective transport, leads to an actual directed radial particle flow. Believed to be important in 2XIIB and OGRA, it is a much more difficult theoretical problem than even neoclassical theory [Cohen, et al., 1983].

Thus a great deal of experimental and theoretical work has been done on radial transport in mirror systems and the effects of low frequency RF waves on particle transport in mirrors and tokamaks. Yet despite this effort, there are many fundamental questions which remain unanswered.

In general, these questions remain because of the difficulties in experimentally measuring radial diffusion coefficients, which are the quantities predicted by theory. In some cases, this is due to the complexity of an experiment with many regions, each with its own plasma parameters. In other cases, it is because plasma profiles are not measured, but instead determined "self–consistently" using classical and neoclassical

transport models—a clear case of circular reasoning.

Measuring the effect of low frequency RF power including ion cyclotron heating (ICH) on ion radial transport is a difficult experiment. In many experiments, ICH is also the principle plasma production mechanism. Turning off the RF power in such an experiment to determine how much of the transport is due to ICH is not possible because then the plasma leaves the device on the timescale of a particle confinement time.

In the experiment described in this thesis many of these difficulties are bypassed or overcome. Constance B is a single cell quadrupole mirror whose plasma is produced by electron cyclotron resonance heating (ECRH). All of the relevant plasma profiles have been measured, allowing determination of the transport coefficients.

1.3 Experimental Motivation

It would be nice to establish the importance of radial transport in determining the ion confinement lifetime without the need for sophisticated profile measurements and computer codes. A measure of the importance of radial transport is the ratio $\tau_\perp(\psi)/\tau_\parallel(\psi)$. where $\tau_\perp$ and $\tau_\parallel$ are the ion perpendicular and parallel lifetimes defined in Equation 4.48. Fortunately there are several measurements which give order–of–magnitude estimates of this ratio, which can be deduced directly from raw data without any fancy processing. These qualitative transport measurements are also useful because they motivate and make plausible the more quantitative (and difficult) transport measurements presented in this thesis.

An estimate of the non–ambipolar contribution to the perpendicular ion current can be found using segmented end wall plates. Figure 1-1 is a schematic of the aluminum plates which were installed in both the north and south fan tanks, rotated 90 degrees with respect to each other to match the elliptical end loss and flux surfaces. The net current in $\mu A/cm^2$ for each plate is also shown in Figure 1-1. Note that all the currents shown for these plates are negative. These plates map to the core plasma.

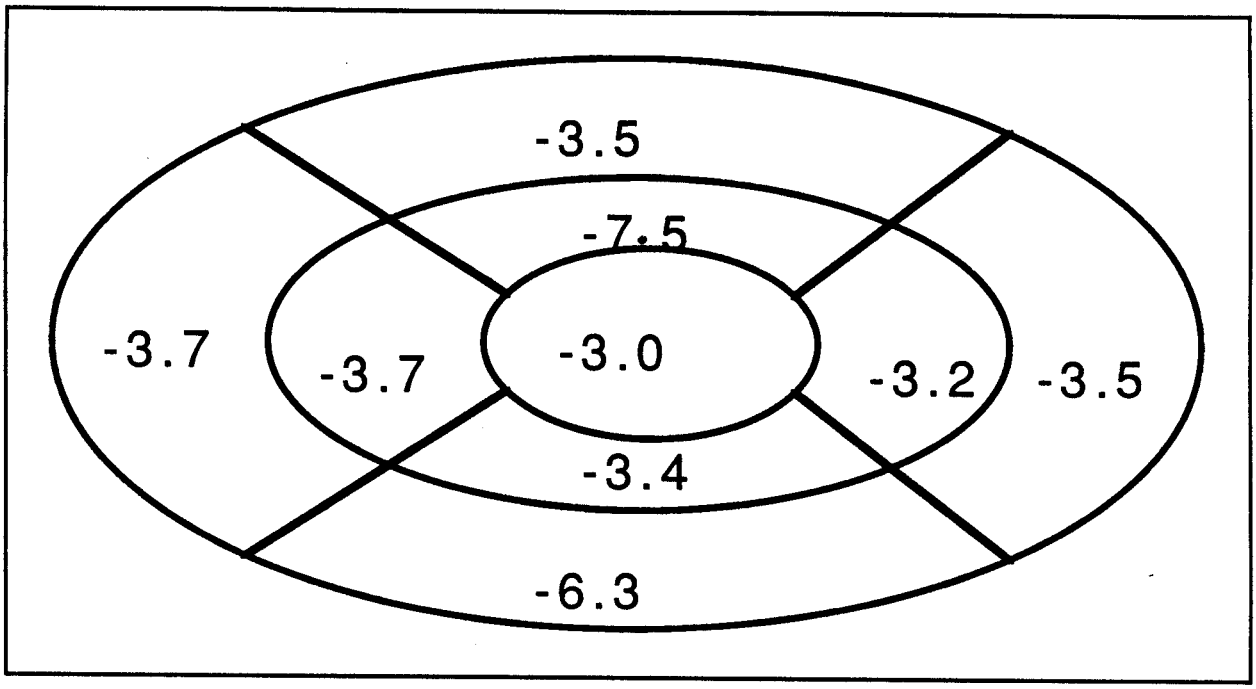

Figure 1-1: The net current plates measure negative net current in the end loss which maps to the plasma core. Current density is in $\mu A./cm^2$ measured at the plate.

(The outer ring maps to 7 cm. at the midplane.) The net current shown is within a factor of two of the average ion current for each plate. The net current was also measured outside the core plasma using net current probes, and found to be positive, with the ion end loss current exceeding the electron end loss at large radius.

A negative net current the same size as the ion end loss current is consistent with outward ion transport and a ratio $\tau_\perp/\tau_\parallel$ of order unity. Inward electron transport, or a combination of electron and ion transport may also be responsible for the large net current, so other types of experiments are necessary to measure the ion transport rate. The large net current is also useful to motivate these additional experiments.

In a machine heated by electron cyclotron heating (ECH), the plasma density and source function are to a great extent determined by the magnetic geometry. The plasma is much smaller when operating at high magnetic field than at low field

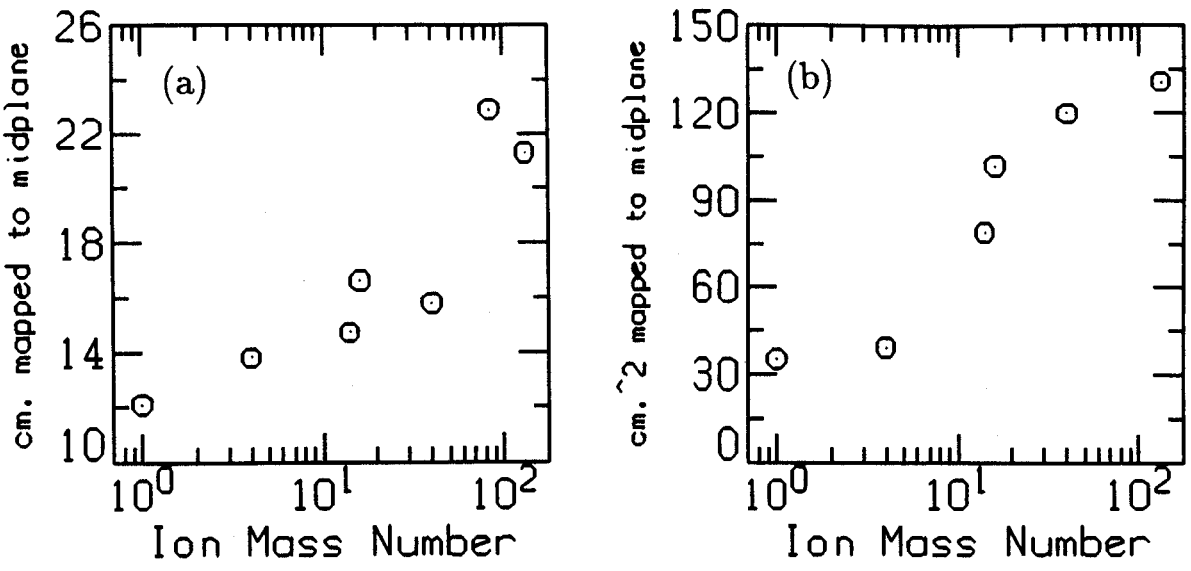

Figure 1-2: End loss widths and variance are shown for plasmas from hydrogen to xenon. (a)FWHM. (b)$< x^2 >$.

because the ECH resonant mod–B surface is much smaller. Since the plasma size is determined by electron physics, the size is almost the same for hydrogen, argon, or even xenon plasmas. In contrast, the ion end loss profiles are measured to vary substantially, depending on which gas is used for back fill and plasma fueling.

Figure 1-2(a) shows the full–width at half maximum (FWHM) as a function of ion mass as measured by a faraday cup. The width in cm. represent distances mapped to the midplane. Figure 1-2(b) is the end loss second moment $< x^2 >$, an alternate description of the width useful when comparing distributions with large "tails". (The broad end loss profiles from high mass number plasmas exhibit these large "tails".)

Note that the end loss width of the high mass plasmas are double the width of hydrogen, indicating an increase in the ion radial transport rate with mass. This scaling is only slightly less dramatic when Finite–Larmor–Radius (FLR) effects are

included in inverting the end loss profiles.

Although this second qualitative transport measurement does not allow direct measurement of the transport coefficients, we see that during their lifetime, the heavy ions are moving radially outward a large fraction of the plasma radius. This requires the ratio $\tau_\perp/\tau_\parallel$ to be of order unity, and helps motivate the more quantitative transport measurements presented in this thesis.

1.4 Thesis Organization

This thesis is divided into six chapters and two appendices. Following the introduction and motivation of Chapter 1, the Constance B experiment is described in Chapter 2. Included in this chapter is a description of the plasma and the diagnostics used in the measurements. Chapter 3 explains how the diagnostics introduced in Chapter 2 are used to measure radial plasma profiles. The raw data collected by the diagnostics is processed to obtain the information necessary for transport measurements. The methods and models used in this process, as well as an error analysis are all included in Chapter 3. Chapter 4 presents the theory applicable to these measurements. The ideas about transport mechanisms and the effect of RF power which have been presented in Chapter 1 are detailed in Chapter 4, including calculations of transport coefficients using Constance parameters. Chapter 5 presents the experimental results in a form which can be compared with the theory of Chapter 4. The various plasma profiles which are themselves interesting are also presented. The main results of this thesis are included in Chapter 5. Chapter 6 summarizes the results and presents conclusions. Suggestions for future work are also included in this chapter. Appendix A contains the atomic physics calculations and data used to convert visible emission data into plasma profiles. Diagnostic calibration data is also included in the appendix. Appendix B provides details of the absolute source measurement, including camera calibration data and a test of particle balance.

Chapter 2

The Constance B Experiment

This chapter describes the Constance B experiment, including the magnetic geometry, plasma parameters and principle plasma diagnostics. The Constance B mirror experiment began operation in October 1983, as a continuation of the M.I.T. Constance I and Constance II programs. Until this thesis, Constance B experiments have mainly focused on electron physics. Theses completed to date on Constance B include *Electron Microinstabilities in an ECRH, Mirror–Confined Plasma* [Garner, 1986], *Electron Velocity–Space Diffusion in a Micro–Unstable ECRH Mirror Plasma* [Hokin, 1987], and *Hot Electron Plasma Equilibrium and Stability in the Constance B Mirror Experiment* [X. Chen, 1988]. Recent experiments have concentrated on ion physics, with the results applicable to the fusion program, ECR ion source development and basic plasma physics research.

2.1 Basic Systems

The Constance B magnetic field is generated by a copper conductor magnet shaped like the seam of a baseball. The magnet produces a midplane magnetic field of 2.8–3.8 kG., with a typical shot lasting two seconds.

Figure 2-1 shows the shape and fluxtube of a baseball magnet. Figure 2-2 shows some field lines and mod–B contours at the horizontal symmetry plane for the Con-

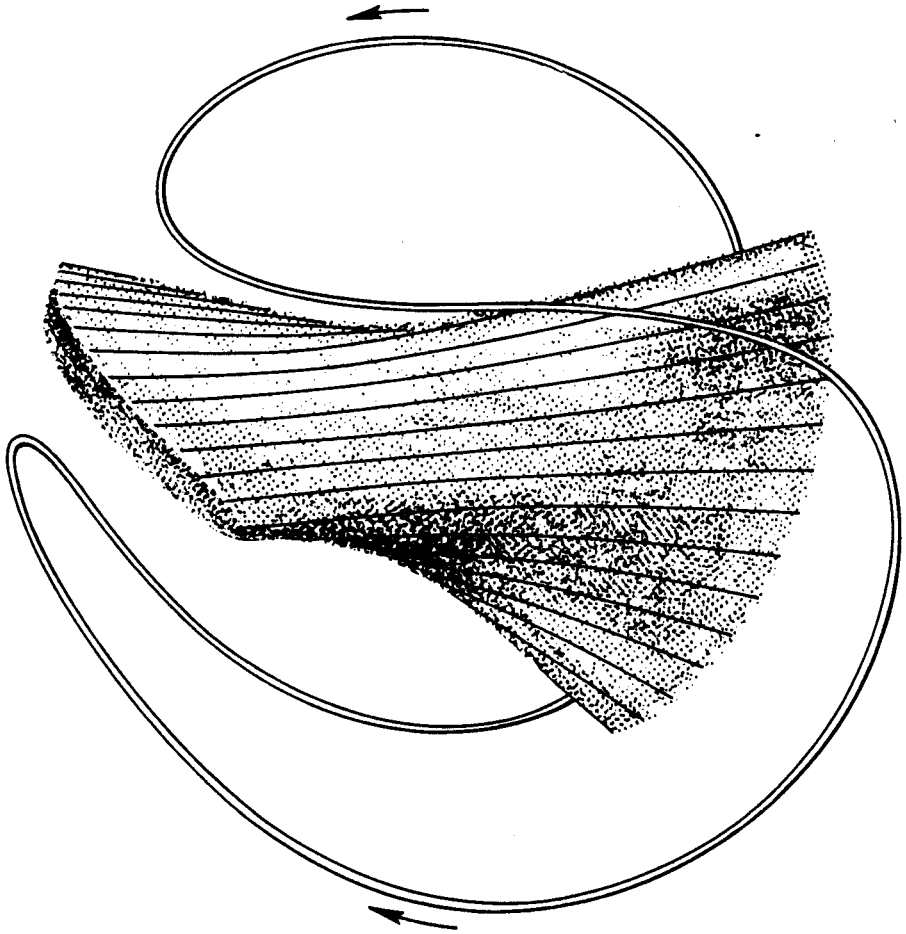

Figure 2-1: A "baseball coil" magnet has winding the shape of the seam of a baseball. The field lines and plasma for this magnetic geometry is also shown.

stance baseball magnet. The field has quadrupole symmetry, and is highly nonaxisymmetric. The flux surfaces are elliptical, with the north and south ends rotated by 90 degrees with respect to each other. This is shown in Figure 2-4. The magnetic mirror ratio is 1.89 on axis, with 80 cm. between the mirror peaks. Constance is a minimum B mirror, meaning that the magnitude of the field increases in all directions outward from the center. The mod–B surfaces are egg shaped, with an ellipticity (ratio of major to minor axis) of 1.6:1 at the ECH resonance zone. The machine has been operated with a magnetic field in the center in the range from 2.7 to 3.8 kG. Most of the work in this thesis used a central magnetic field of 3.5 kG.

The plasma is produced by the breakdown of gas using microwaves resonant with the electron cyclotron frequency (ECRH). Various gasses including hydrogen, helium, argon, oxygen, nitrogen, neon, krypton, xenon and carbon dioxide have been used.

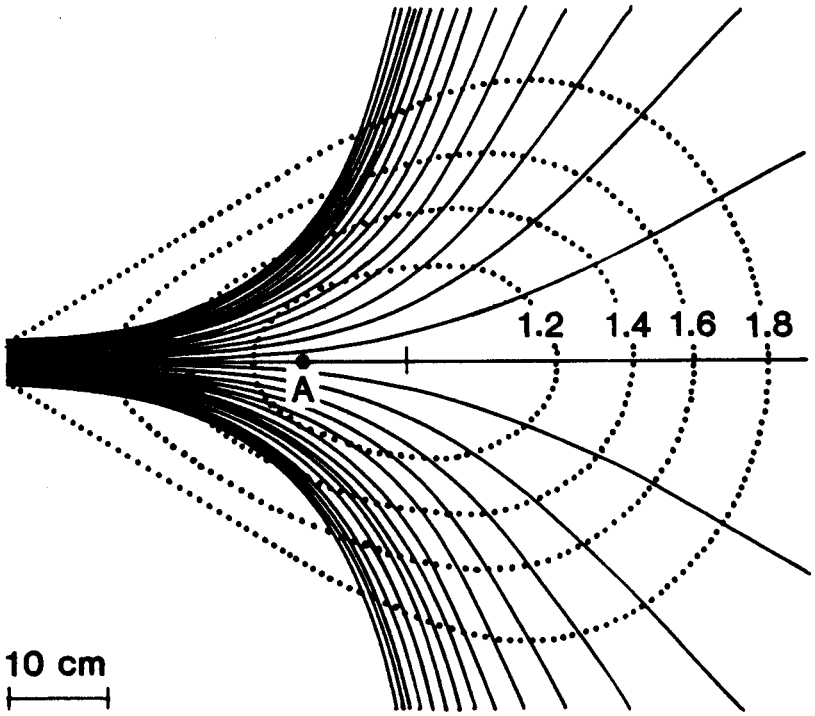

Figure 2-2: The Constance magnetic field line and mod–B contours are shown. The system has quadrupole symmetry and is highly nonaxisymmetric, resulting in the large field line fanning shown in this figure.

Experiments in hydrogen, helium and argon plasmas are described in this thesis. The microwaves are produced by a 10.5 GHz CW klystron (Varian Model VA–911) with up to 5 kW power available. Most of the data in this thesis was collected using 2 kW of forward ECH power.

The vacuum is maintained by a turbomolecular pump, (Airco Model 514), titanium getters, and a cryogenic LHe pump, resulting in a base pressure of 1–4 $\times 10^{-8}$ Torr. The background gas, which during the shot consists mostly of hydrogen, produces approximately 4 percent hydrogen impurity in helium and argon plasmas.

The vacuum chamber consists of three sections. (See Figure 2-3) The central chamber is welded from two pieces to fit inside the baseball magnet, and is long enough in Z to contain both mirror peaks. Two large cylindrical fan tanks, about

1.5 meters in diameter and 2 meters long, are located at the ends of the machine and oriented at 90 degrees with respect to each other, to accommodate the highly elliptical end loss. These large tanks, with fast neutral pumping, were designed to minimize the plasma cooling that results when secondary electrons from the walls stream back along field lines. This is in contrast to the early INTEREM results [Haste, et al., 1968] where line tying to the nearby vacuum chamber end wall was important and the plasma potential much smaller.

The shot timing sequence is controlled by an industrial process controller (Gould model 484) which controls the magnetic field ramp–up, the back–fill gas timing and the ECH timing. During a typical shot, the back–fill gas and magnet current reach steady state within a few seconds. The ECH is turned on for about two seconds. Halfway through this period, the ICH is pulsed for 150 ms. Finally, the ECH, gas puffing and magnet are turned off. Data is collected during the full two second shot.

A CAMAC–based data acquisition system is used in Constance in conjunction with a VAX 11/750 computer. It uses the VAX/VMS data acquisition software package MDS [Fredian and Stillerman, 1986] to set up and control the data system and process and display the signals. Many of the signals were digitized using a LeCroy Model 8212 digitizer, running at a 2 kHz sampling rate. Other CAMAC modules used in this thesis include a phase digitizer (Jorway 1808) for the microwave interferometer, a 100 MHz digitizer and hardware signal averager for the Time–of–Flight Analyzer (DSP T2001AS and T4100) and a camera control module for the CCD camera (Data Design Corp. AC100).

RF System

Low frequency RF power in the range from 1–5 MHz is applied by a double half–turn antenna centered on the midplane. Ground straps parallel to Z make the antenna geometry similar to a Nagoya Type III configuration [Watari, et al., 1978]. The RF system consists of a transmitter, capacitor bank, transmission line, matchbox, vacuum feedthrough and antenna, as shown in Figure 2-3. Two different transmitters have

been used. Originally a triode (Eimac 3CW40,000H3) operating as an oscillator in a tuned grid–tuned plate configuration provided 50 ms of RF power at up to 10 kW. Subsequently, the system was upgraded using an Eimac 4CW100,000E tube running as an amplifier to produce longer pulses. An HP 3325A synthesizer/function generator and ENI Model 2100 RF power amp were used to excite the amplifier. Most of the data in this thesis was obtained using 150 ms pulses of RF at 1.4 MHz, with power levels at the antenna of up to 10 kW and RF antenna voltages of up to 12 kV peak. A directional coupler monitors the forward and reflected power flowing to the matchbox and antenna systems. A capacitively coupled voltage divider and RF diode are used to monitor the RF antenna voltage. The antenna voltage as a function of low voltage divider signal was calibrated using a high voltage probe.

2.2 Diagnostics

Photon Diagnostics

Camera System

The camera system consists of a charge coupled device (CCD) light integrating camera (EG&G Reticon Model MC9128) controlled by a CAMAC module. The camera has 16,384 detectors mounted in a square 128 $\times$ 128 array. Each pixel is digitized on a scale from 0–255. Frame integration times can be set from 3 ms to several seconds. The AC100 control module can accept up to 16 frames per shot, which is then down loaded to the VAX computer between shots.

By using optical bandpass filters, the camera can record the emission of a single atomic transition line. The camera was absolutely calibrated at three wavelengths used in this thesis for density and ionization source measurements, using a tungsten lamp with known light output. The results are shown in Table 2.1, with the calibration details described in Appendix B. The camera system was also checked for linearity with respect to integration time and light level. An f/1.8 50mm. camera lens was

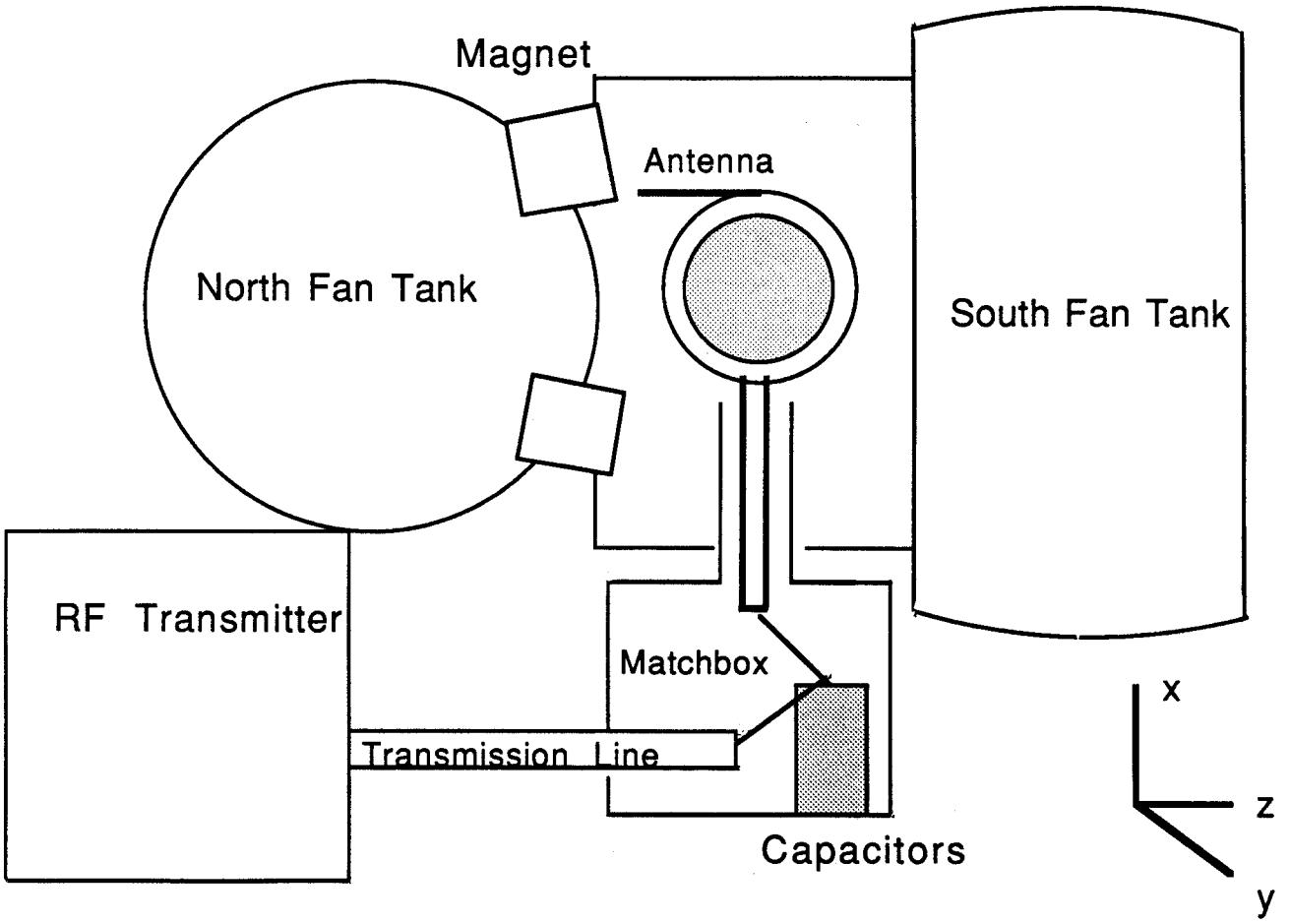

Figure 2-3: The system used to apply low frequency RF power and the Constance vacuum chamber are shown.

mounted in front of the CCD camera, and used for all measurements, including the absolute calibration. Under low light conditions, an image intensifier (Electrophysics Model 9100) was mounted between the lens and camera. The gain of the image intensifier under the various plasma conditions was calibrated using a photomultiplier tube, described below.

Optical Multichannel Analyzer (OMA)

The OMA system[1] consists of a 0.62 meter spectrometer (ISA Instruments), a detector controller (Princeton Instruments ST-110), and a microchannel plate image

[1]The OMA system was set up and calibrated by Craig Petty.

Wavelength ($\mathring{A}$)	Photons per Pixel Level
6963 (H_α)	1.57×10^5
4922 (He I)	3.43×10^5
6965 (Ar I)	2.60×10^5

Table 2.1: Using a tungsten lamp with known light spectrum, the camera system including lens, filters and CCD camera, was absolutely calibrated. The absolute calibration allows an absolute measurement of the ionization source function, as described in Chapter 5.

intensified photodiode array (Princeton Instruments IRY–512). The photodiode array consists of 512 detectors whose response is digitized to obtain complete optical spectrums. The system has been calibrated using a mercury vapor lamp so that the inherent spectral resolution as a function of wavelength is known. The instrumental resolution is then taken into account when ion line widths are used to measure the Doppler broadened ion temperatures.

Photomultiplier Tube (PMT)

A photomultiplier tube (Hamamatsu R329) was used for low light signal measurements and for measurements where the full two dimensional camera pictures were unnecessary. The PMT was also used to calibrate the gain of the image intensifier to allow absolute measurements of the ionization source function, even at the lowest light levels. The details of this method are described in the next chapter. Both the camera and PMT were mounted outside the fan tank, looking along the machine z axis. The OMA was mounted outside the central chamber, viewing along the x axis. The placement of the various diagnostics used in this thesis is shown in Figure 2-4.

Microwave Interferometer

A single channel 24 GHz. interferometer[2] is used to measure the line integrated plasma density. The interferometer is located on the midplane, oriented at 45 degrees with respect to the symmetry plane. The microwaves are launched perpendicular to the magnetic axis, with the electric field polarized along the z axis. The index of refraction for the O–mode waves is approximately:

$$\epsilon = 1 - \frac{\omega_p^2}{\omega^2} < \frac{1}{\gamma} > \tag{2.1}$$

where $\frac{1}{\gamma}$ is an approximate relativistic correction to the plasma dielectric caused by the relativistic mass shift [Mauel, 1985]. The interferometer is used to normalize the plasma density profile, as described in Chapter 3.

Particle Diagnostics

Faraday Cup

A Faraday cup was mounted on a long shaft and used to collect ions. Particles entering the 3.2 mm. diameter aperture in the aluminum housing encounter a copper disk biased at -2 kV Ions and energetic electrons which proceed through the hole in the repelling disk are then collected by a copper cup. The copper repelling disk also inhibits the secondary emission of electrons from the cup. The signal current due to the energetic electrons is less than ten percent of the signal and is subtracted when the data is processed. The effect of secondary electrons can be measured by biasing the collection cup at various voltages and measuring the change in collected current. When the copper disk was biased a few hundred volts negative, secondary electron current is no longer detectable. A sketch of the Faraday cup probe is shown in Figure 2-5 (a).

[2]The microwave interferometer was set up by Donna Smatlak

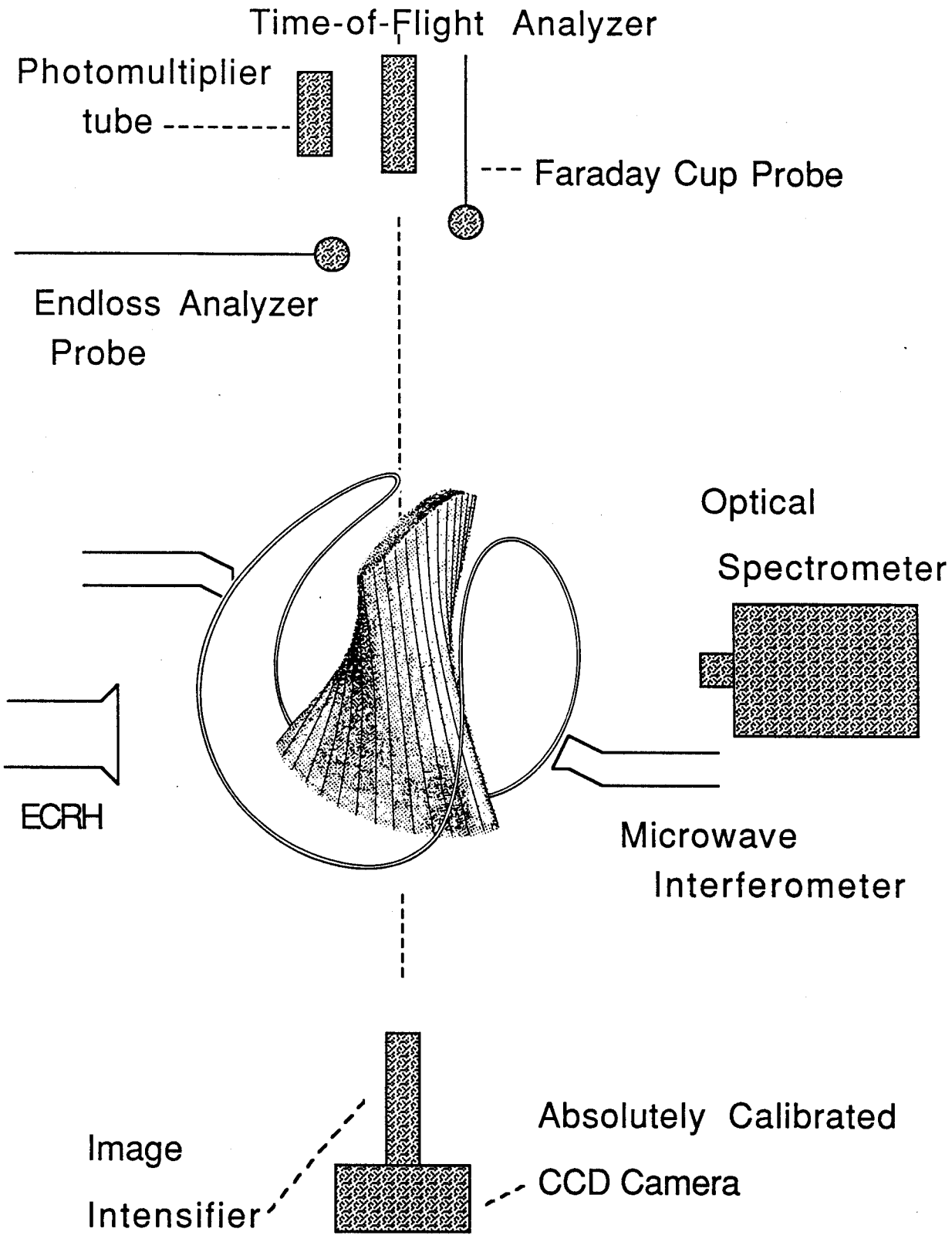

Figure 2-4: Diagnostics used in this thesis

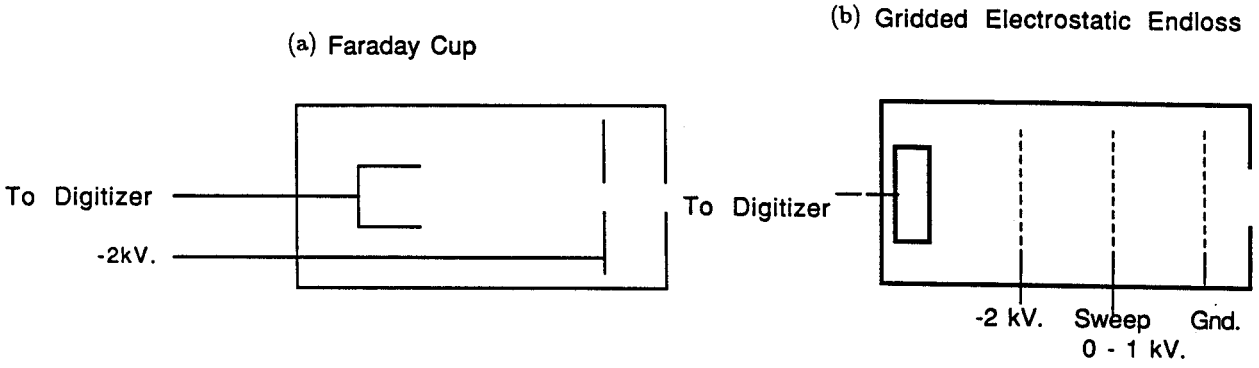

Figure 2-5: (a) The Faraday cup probe uses a copper disk to repel electrons and collects ions in a copper cup. (b) The electrostatic end loss analyzer repels electrons with one grid, and allows ions of various energies to pass using a second grid. The outside grid is either grounded, so keep the electric fields inside the ELA, or removed to increase the particle current collected.

Gridded Electrostatic End Loss Analyzer (ELA)

An electrostatic analyzer with three partially transparent grids[3] was mounted on a long shaft and used to measure the electron confining potential. A sketch of the ELA probe is shown in Figure 2-5 (b). By repelling electrons with one grid and sweeping the voltage on the ion repeller grid with a high voltage amplifier (TREK Model 609–6), the potential difference which accelerated the ions can be measured.

Time–of–Flight Analyzer (TOFA)

The Time–of–Flight Analyzer (TOFA)[4] measures the charge state distribution of the end loss ions as well as the parallel temperature of each charge state. The time required for an ion of mass m, charge q and energy E to traverse a distance L is:

$$\tau = L\sqrt{\frac{m}{2[q(\phi + V_b) + E]}} \tag{2.2}$$

[3]Rich Garner [Garner, 1986] calibrated this End Loss Analyzer and found the grids to have a 60 percent transparency)

[4]The Time–of–Flight Analyzer was designed and built by Craig Petty.

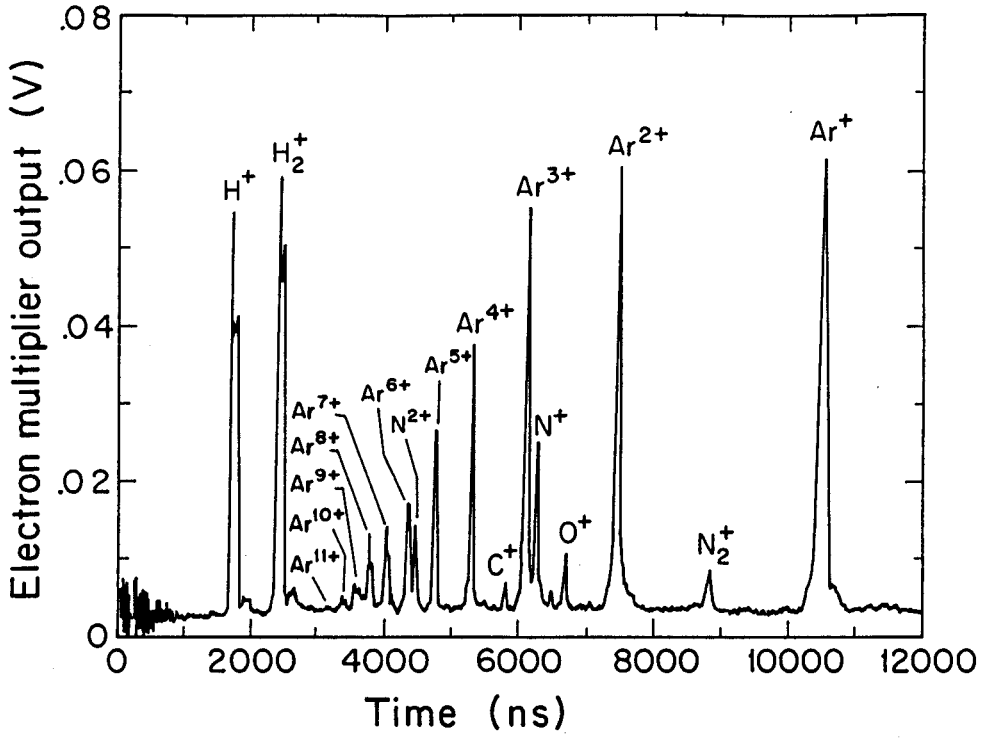

Figure 2-6: The charge state present in the end loss of an argon plasma are shown. The Time–of–Flight analyzer is used to measure the charge state distribution and parallel ion energy in the end loss.

where ϕ is the plasma potential and V_b is the acceleration potential between the ends of the analyzer. An electrostatic gate allows a pulse of ions to enter the analyzer. The pulse spreads out during passage through the one meter long analyzer tube. The delay time given by Equation 2.2 allows identification of the charge species and their initial energies. Details about this diagnostic are given in [Petty, 1987]. A typical charge state end loss spectra for an argon plasma is shown in Figure 2-6.

Chapter 3

Experimental Method

Using the diagnostics introduced in chapter 2, various plasma profiles can be measured. The typical plasma parameters in Constance are shown in Table 3.1. In general, the raw data collected by the diagnostics has to be processed to obtain the profiles relevant to transport measurements. The processing may be simple, such as mapping the position of a probe back along the magnetic field lines to the midplane position which "labels" the field line. The processing can also be quite complicated, such as the calculation of the number of particles ionized on a field line, deduced from the brightness of a group of pixels in a camera picture. Such a calculation involves subsidiary measurements (cold electron temperature, camera calibrations), geometrical corrections, and the calculation of a variety of atomic physics processes.

The processing and models that allow plasma profiles to be measured are the subject of this chapter. An analysis of the expected uncertainties in the measured profiles due to both experimental error and to the necessary processing of the data is also included in this chapter.

3.1 Electron Temperature Measurements

While the cold electron temperature (T_{ec}) profile is not directly used to calculate the ion transport rate or diffusion coefficients, it is an auxiliary measurement required to

Source Gas	Helium
n_{ec}	$3 \times 10^{11} cm^{-3}$
n_{eh}	$2 \times 10^{11} cm^{-3}$
T_{ec}	100 eV.
T_{eh}	400 keV.
T_i	8 eV.
B_0	3.5 kG.
P_{ECH}	2 kW.
P (gauge)	5×10^{-7} Torr.
r_P	10 cm.
L_P	40 cm.
Pulse length	2 s.

Table 3.1: Typical plasma parameters in Constance are shown.

find the ionization source and density profiles. We thus describe the T_{ec} measurements before presenting the profile measurements needed for transport measurements. The experimental method of measuring T_{ec} and the results of the measurement are also interesting in their own right. As shown in [X. Chen, 1988], electrons in Constance are primarily heated along a baseball seam shaped curve where the field lines and mod–B surfaces are tangent. When viewed axially from the fan tanks, this heating profile results in a concentration of hotter electrons in four balls located at 45, 135, 225 and 315 degrees at a radius corresponding to the ECH resonance surface. The measurement of T_{ec} shows the same symmetry, (see Figure 3-3) lending confidence both to this measurement and to other measurements which use the CCD camera.

Although the use of visible line ratios to measure electron temperature is a common technique, this measurement of T_{ec} is the first two dimensional T_{ec} measurement. Bandpass filters and the CCD camera are used to take pictures of the emission from a singlet (4922 $\AA$) and triplet (4713 $\AA$) He^I line and from the continuum background. After subtracting the background and smoothing, the line–of–sight average cold electron temperature is found from the triplet–singlet ratio, using data from the curve of Figure 3-1. The theoretical derivation of this curve is given in Appendix A, and

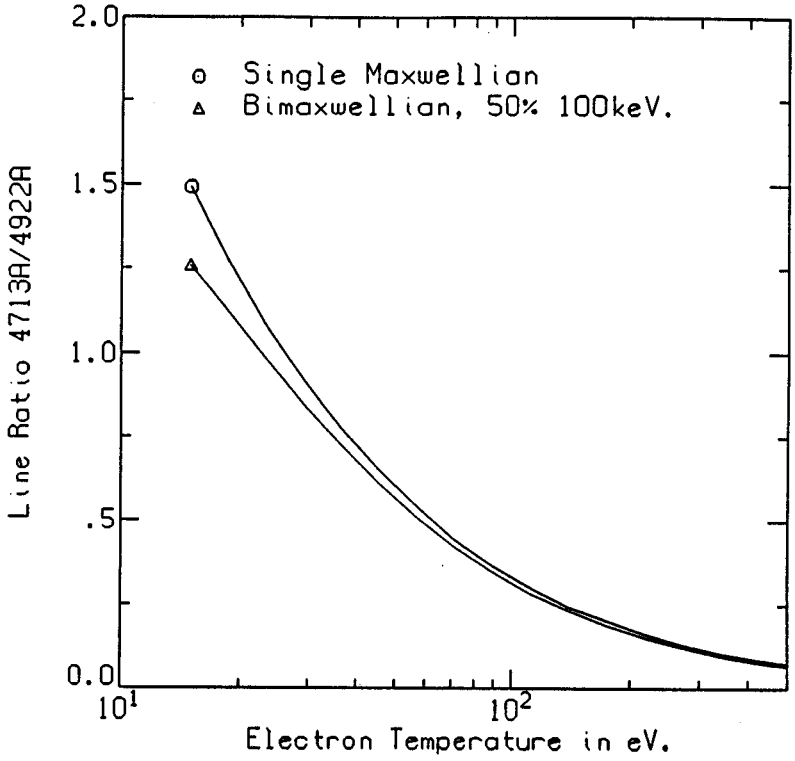

Figure 3-1: T_{ec} can be found from the helium singlet–triplet line ratio. The derivation of this curve is found in Appendix A.

requires a knowledge of the excitation cross section of the helium 4^1D and 4^3S states.

Contours of constant brightness for a helium plasma viewed through the 4922 $\AA$ and 4713 $\AA$ bandpass filters are shown in Figure 3-2 (a) and (b) respectively. Note that the 4713 $\AA$ picture is diamond shaped and the 4922 $\AA$ picture is more round. Warmer electrons tend to be more deeply trapped; confined close to the the midplane. The coldest electrons extend out further in z, to the region where the flux surfaces are highly elliptical. These colder electrons produce a characteristic "cross" which shows up as diamond shaped contours on the 4713 $\AA$ picture. The excitation cross section to the singlet state is less sensitive to T_{ec}, and so the 4922 $\AA$ picture more strongly weights the hotter electrons inhabiting nearly circular flux surfaces near the midplane.

Combining Figure 3-1 and 3-2 gives the T_{ec} contours of Figure 3-3. Note the

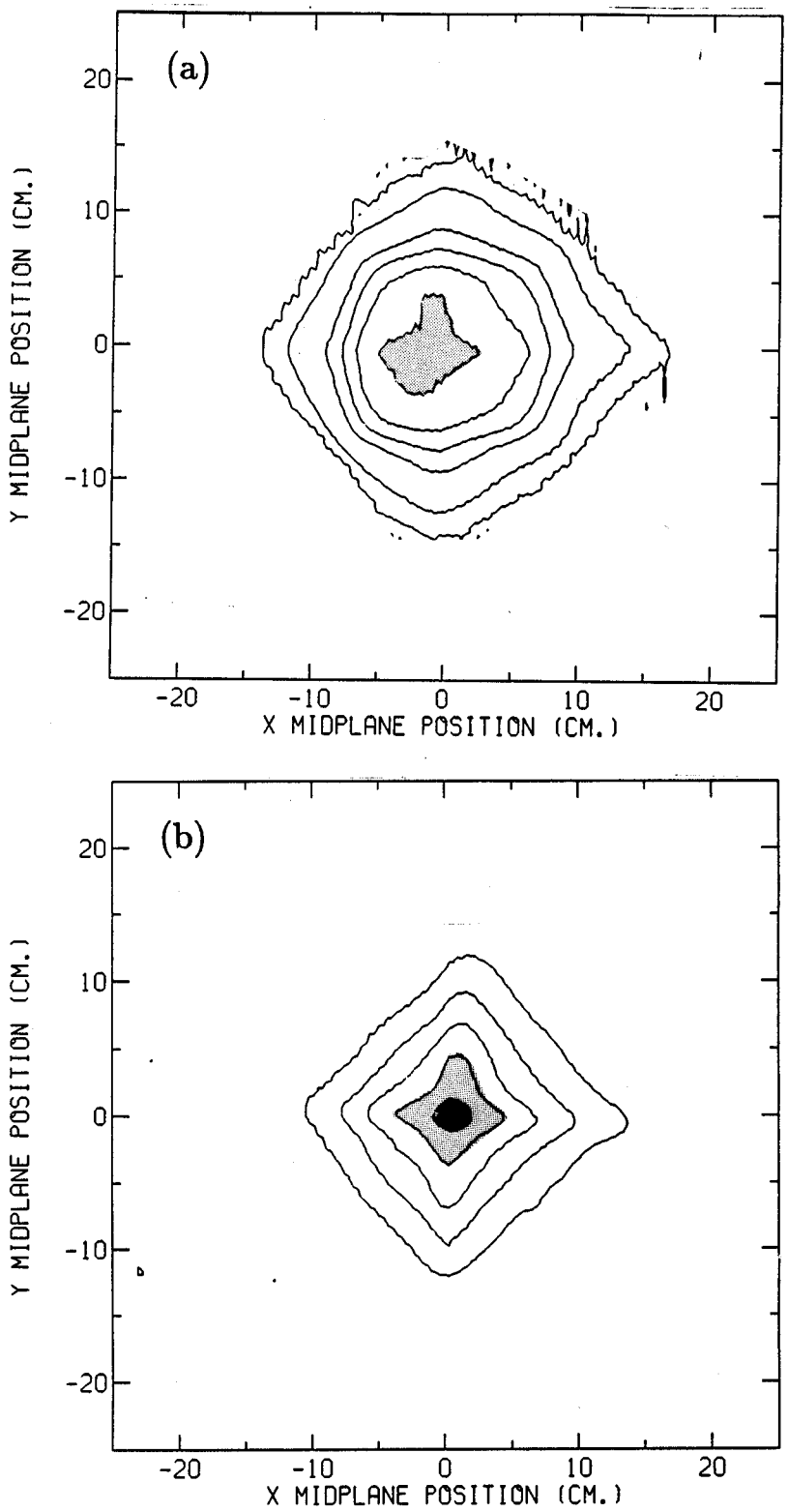

Figure 3-2: (a) A helium plasma ($B_0 = 3.0kG.$, $P_{ECH} = 2kW$, P(gauge)=6×10^{-7} Torr) viewed through a 4922 $\AA$ filter is round, whereas, (b) the plasma appears more diamond shaped when viewed through a 4713 $\AA$ filter. The latter is more sensitive to the cold electrons in the elliptical fanning region.

presence of the four hot electron balls. After averaging T_{ec} over each flux surface, we find that T_{ec} rises from about 30 eV. on axis to 150 eV. at the ECH resonant surface, and then decreases out to the plasma edge. This is shown in Figure 3-4. The abscissa is the magnetic flux variable ψ , which to lowest order equals r^2 at the midplane.

Error Analysis

The measurement of the line ratio R has a high degree of precision (3–5 percent from shot–to–shot variation, and less than this from the photomultiplier wavelength dependence because the 4922 $\AA$ and 4713 $\AA$ lines are close in wavelength), but the T_{ec} measurement has much less accuracy due to the uncertainties in the cross section on which the model is based. Using Figure 3-1 to calculate the derivatives:

At 30 eV. $\Delta R/R = 5\% \Rightarrow \Delta T/T = 7\%$.

At 70 eV. $\Delta R/R = 5\% \Rightarrow \Delta T/T = 5\%$.

Thus $\Delta T/T \leq 7\%$ directly due to uncertainties in R. Using the differences between the calculated and experimental cross section described in Appendix A gives an absolute accuracy error in $T_{ec}(\psi)$ of approximately 40 percent.

Although we know the absolute value of T_{ec} only to within 40 percent, the relative value of T_{ec} (profile shape) is much better known. Fortunately, the T_{ec} profile shape is more important than the absolute value of T_{ec} in doing transport measurements as is shown in the next several sections.

3.2 Density Measurements

The ion density profile n(ψ) can be obtained from the emission brightness profile, requiring also the excitation cross sections, cold electron temperature, geometrical factors and the average ion charge state. If we assume a uniform neutral background n_0=constant (a good assumption for the low density and small plasma radius of Constance where the neutral mean free path is more than ten times the plasma

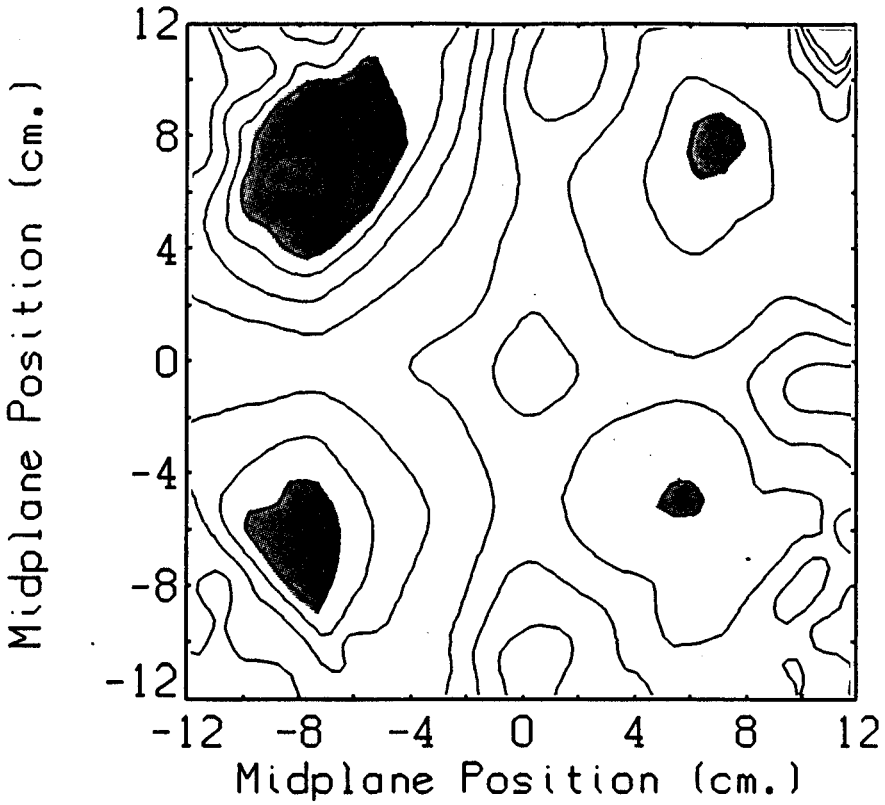

Figure 3-3: Contours of cold electron temperature are made using a CCD camera and optical bandpass filters. Note the presence of the four hotter regions due to the ECH electron heating geometry.

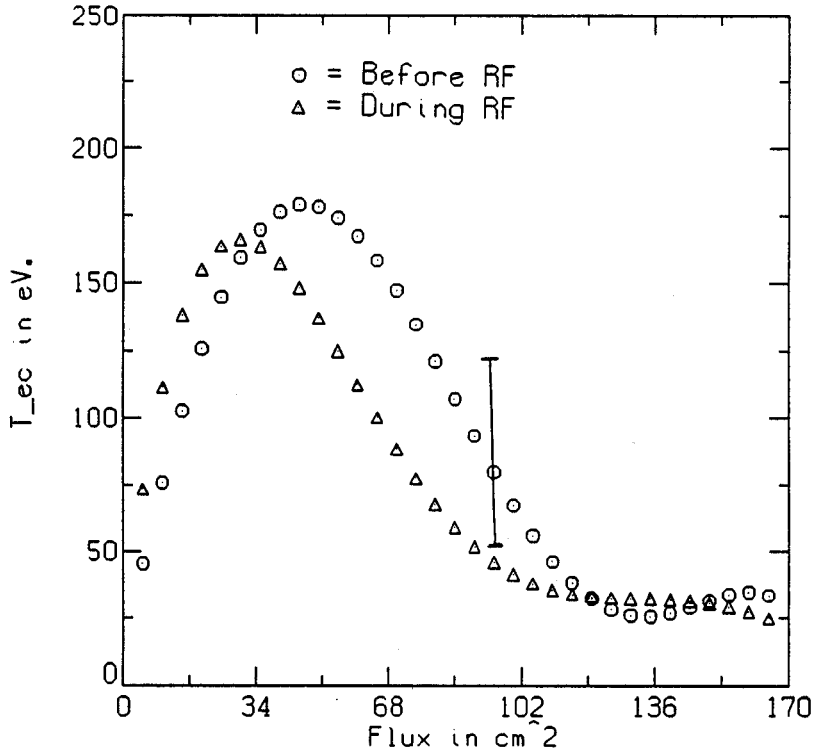

Figure 3-4: The $T_{ec}(\psi)$ profile shows a maximum temperature at the radius where the maximum electron heating occurs.

radius), then the ion density is:

$$n(\psi) = \frac{\int B(x,y)dz}{n_0 < \sigma v >_{exc}(\psi)} \frac{\int n\, dl / \int n\, dz}{Z^{in}_{avg}\, L_p(\psi)} \tag{3.1}$$

where $\int B(x,y)dz = \int n_e n_0 < \sigma v >_{exc} dz$ is the brightness profile measured by the CCD camera through an optical bandpass filter,

$< \sigma v >_{exc}$ is the temperature dependent electron distribution averaged cross section for excitation from the ground state to the atomic state of interest,

Z^{in}_{avg} is the average charge state, and

$\int n\, dl / \int n\, dz$ is a geometrical correction to compensate for the difference between line of sight quantities and field line integrated quantities.

The choice of which emission line to use for density measurements depends on several factors. The line should be strong and far removed in wavelength from competing lines. The excitation cross section should be well known, and not too strongly dependent on T_{ec}. In the limit of $< \sigma v >_{exc}$ independent of T_{ec}, the errors in measuring the $T_{ec}(\psi)$ profile would not contribute at all to the error bars of n(ψ).

The lines chosen for the density measurements are the H_α (6963 $\AA$) line in hydrogen, the 4^1D (4922 $\AA$) He^I line and the $4S[\frac{3}{2}]^0 - 4p'[\frac{1}{2}]$ (6965 $\AA$) Ar^I line. The excitation cross sections for these three lines are relatively independent of T_{ec}, varying roughly as T_{ec} to an inverse fractional power for energies greater than about twice the threshold energy. The cross sections for these lines are shown in Appendix A.

The geometrical correction in Equation 3.1 is calculated using an equilibrium code (PLINEINT) developed by Chen [X. Chen, 1988]. The code includes an accurate model of the complicated Constance magnetic field geometry. By varying 10 free parameters, a best fit to the experimental line–of–sight integrated brightness profile can be found. This allows a very close fit to the experimental data. The program then calculates the ratio $\int n\, dl / \int n\, dz$, and averages this value over each flux surface.

Figure 3-5 (a) shows contours of constant brightness for the 4922 $\AA$ line of a helium plasma under standard conditions. ($B_0 = 3.5kG$, P_{ECH}=2kW, P=5 $\times$ 10^{-7} Torr.) Figure 3-5 (b) is an "X–cut" of Figure 3-5 (a), showing the intensity along the

x axis. Figure 3-6 (a) and (b) are the code calculated brightness contours and "X–cut" using the best fit plasma parameters. The experiment and simulation are similar in shape and both have full width at half maxima (FWHM) corresponding to 16.3 cm. at the midplane. Figure 3-7 shows the geometrical correction ratio $\int n\, dl / \int n\, dz$ computed using this best fit plasma model.

The contribution of hot electrons (E $\geq$ 10 keV.) to the electron density profile is not included in Figure 3-5 because these electrons are much less effective than cold electrons at exciting neutral helium. Chen has measured the pressure profile due to the hot electrons, using a variety of diagnostics, and found it to be hollow. At 3.5 kG., the ECH resonant surface is at $r_0 < 3$ cm. or $\psi < 9cm^2$, so the hot electrons peak close to the magnetic axis. The pressure outside the peak decreases with flux, with a scale length similar to that of the cold electron density. The correct total density is the sum of the hot and cold densities: $n_e = n_h + n_c$. However, by operating at 3.5 kG. these profiles are almost the same for most of the profile. Thus we use the measured n_e profile for transport calculations, normalized using the microwave interferometer to include both n_h and n_c.

The average charge state Z^{in}_{avg} in Equation 3.1 is obtained using the Time–of–Flight analyzer (TOFA) and parallel ion confinement modelling. For hydrogen Z^{in}_{avg} is identically one. For helium and argon, parallel ion confinement is assumed to be due to a combination of flow and Pastukhov confinement [Rognlien and Cutler, 1980, Pastukhov, 1974]. Rognlien and Cutler found that the best fit to Fokker–Planck codes was an ion confinement time equal to the *sum* of the flow and Pastukhov times:

$$\tau_\perp(\phi 1) = \tau_P(\phi_1) + \tau_F(\phi_1) \tag{3.2}$$

where:

$$\tau_P(\phi_1) \simeq \tau_{ii} \frac{Z_i \phi_1}{T_i} \exp(\frac{Z_i \phi_1}{T_i})$$

$$\tau_F(\phi_1) = L_P R \sqrt{\frac{\pi m}{2T_i}} \exp(\frac{Z_i \phi_1}{T_i})$$

$L_P(\psi)$ = plasma length,

$R(\psi)$ = the magnetic mirror ratio,

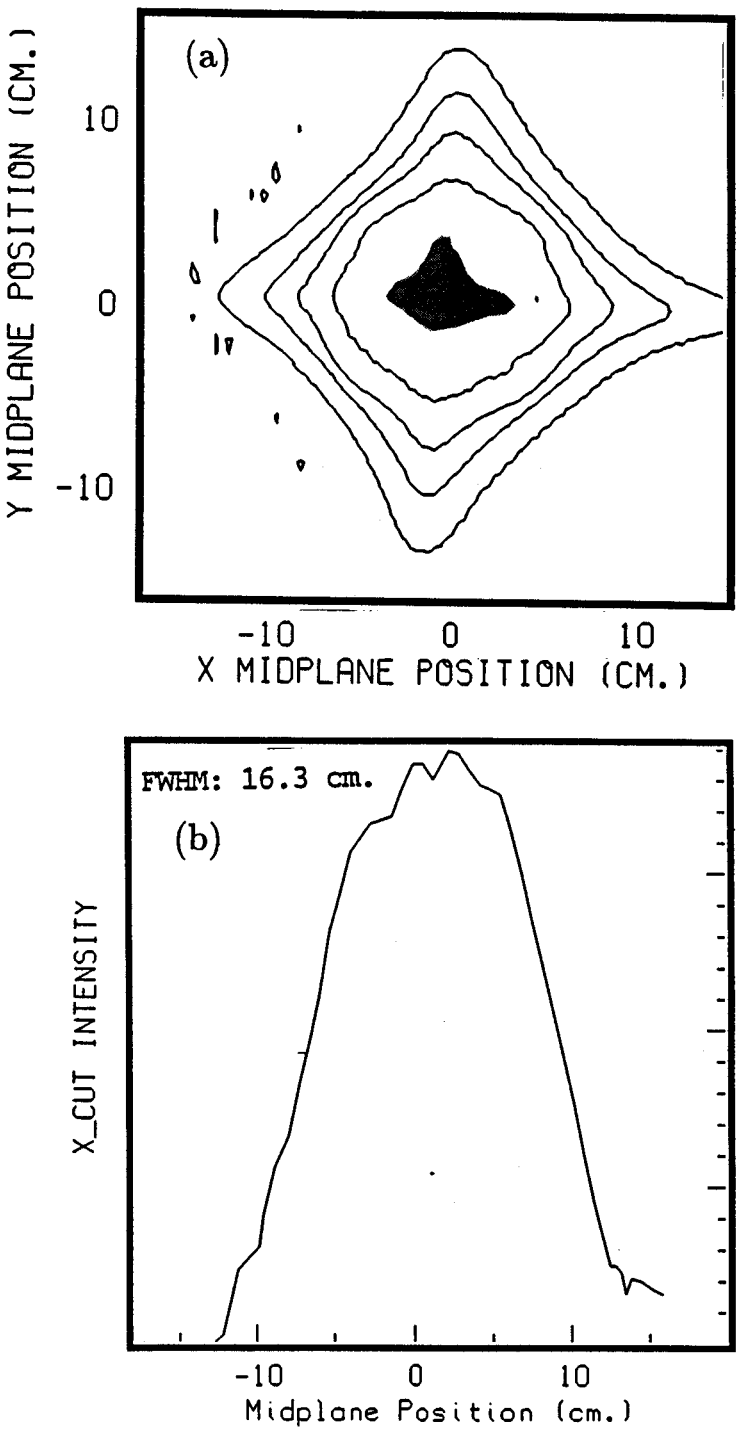

Figure 3-5: (a) This picture of a helium plasma under standard conditions ($B_0 = 3.5kG.$, $P_{ECH} = 2$ kW, P=5×10^{-7} Torr gauge pressure) was taken through a 4922 $\AA$ filter, and is used to calculate density and ionization source profiles. (b) The intensity of the contours of (a) along the x axis is plotted.

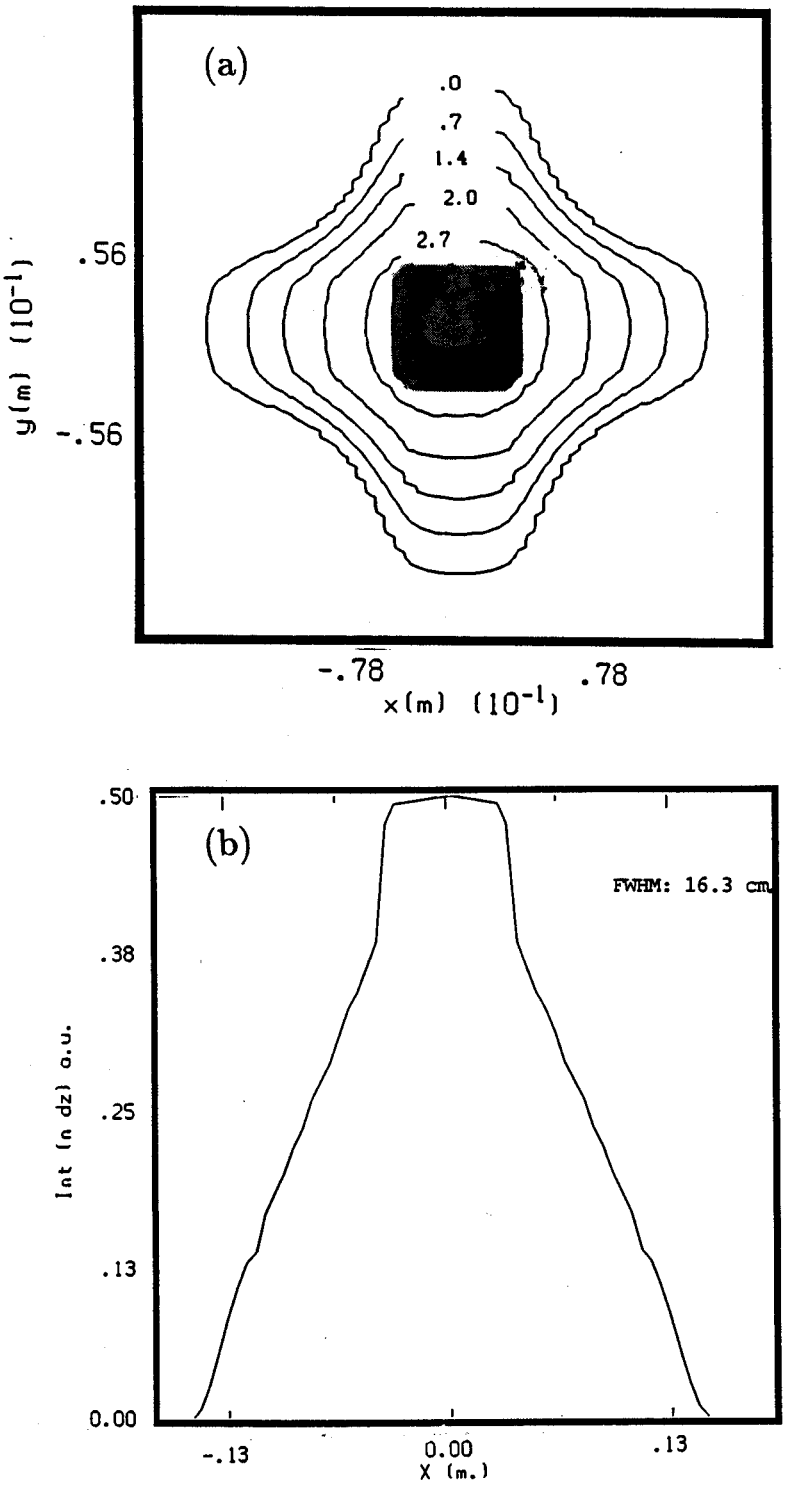

Figure 3-6: (a) The PLINEINT code generated this line–of–sight density average. The code is used to determine the geometrical corrections that arise due to the difference between averages along field lines and averages along the line–of–sight. (b) Intensity of (a) along the x axis.

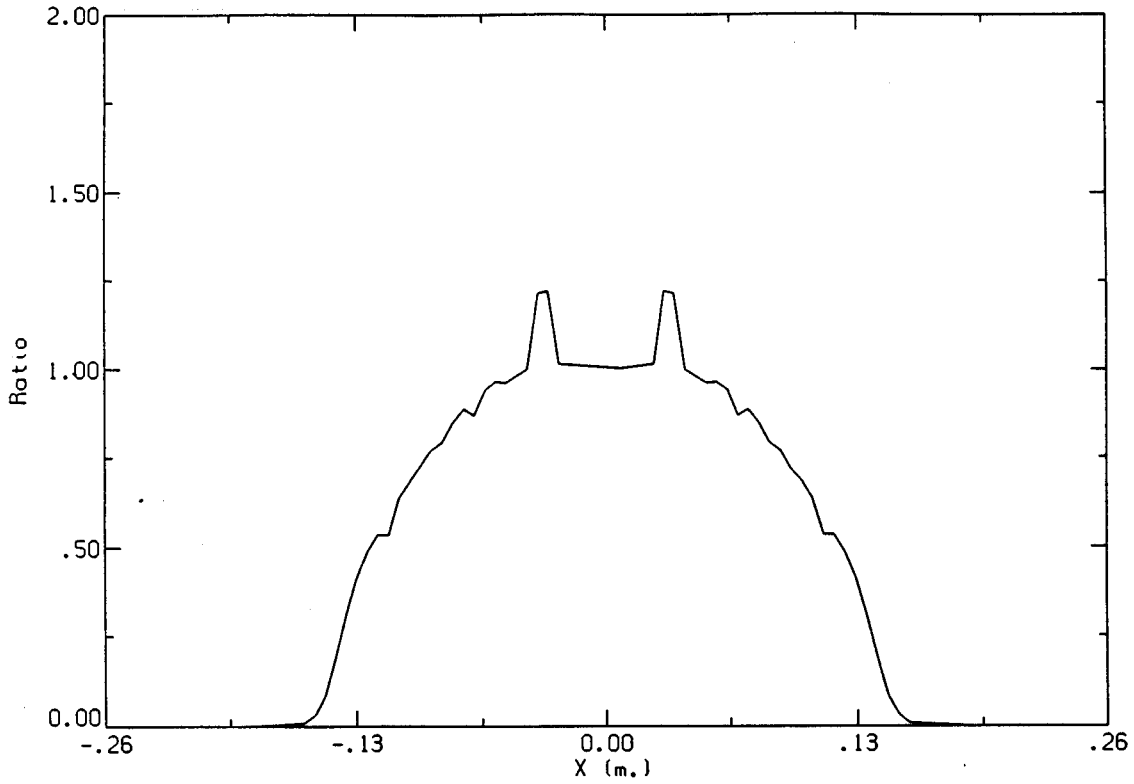

Figure 3-7: The geometrical correction ratio $\int n\ dl / \int n\ dz$ is shown for the best fit plasma model in a helium plasma under standard conditions.

$\tau_{ii}(Z^{in}_{avg}, \bar{n}, T_i)$ = the ion–ion scattering time, and

ϕ_1 is the ion confining potential dip due to the hot electrons, as described in section 3.4.

Although the model is complicated, the result is easy to understand. The average charge state in the end loss is measured by TOFA, and found to be 1.3 for helium and 3.2 for argon. The potential dip increases the lifetime of the higher charge states, thus increasing their density fraction. Using this data and the model of Equation 3.2 we find $Z^{in}_{avg} \simeq 1.5$ for helium and 3.8 for argon. This is found using a code which varies the charge state distribution in the plasma and the potential dip ϕ_1 in order to match the end loss charge state distribution measured by TOFA. Except for the very edge of the plasma, the charge state is independent of flux to within experimental error.

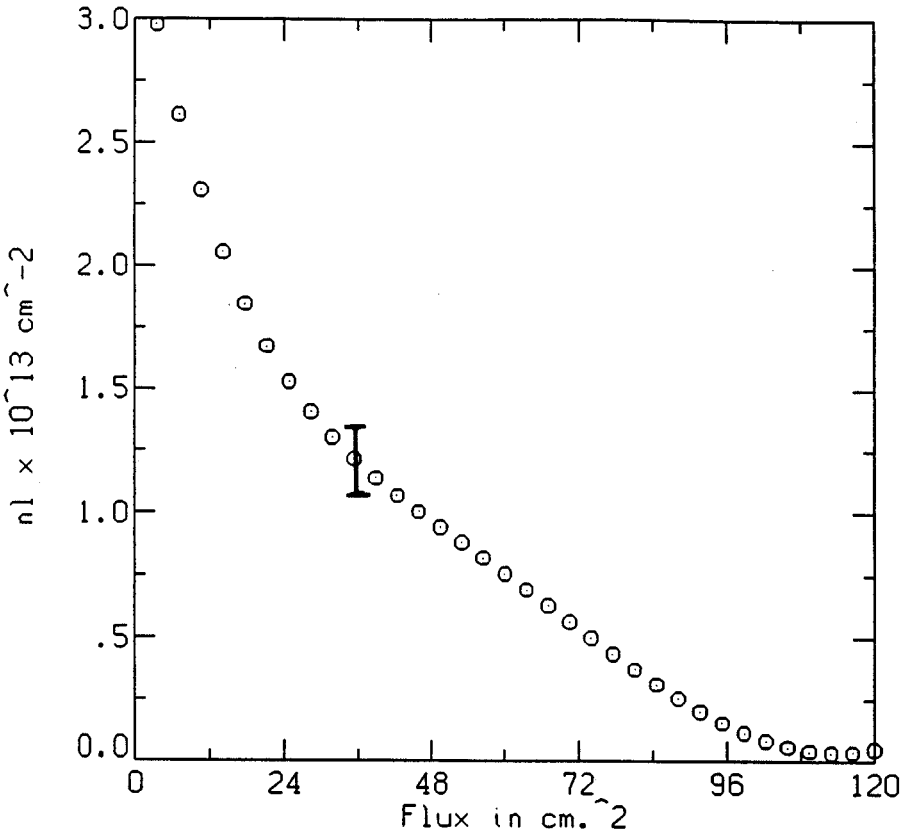

Figure 3-8: The axial line density $\bar{n}$ in helium is measured using the CCD camera, T_{ec} profile, geometrical corrections and excitation cross sections.

Combining the brightness profile of Figure 3-5, the geometrical corrections provided by the PLINEINT code, the excitation cross sections of Appendix A, and Z^{in}_{avg} from TOFA, we find the density profile shown for helium in Figure 3-8. Radial density profiles in hydrogen and argon are similar, as shown in Figures 3-9(a) and (b), and coefficients for constructing these profiles are tabulated at the end of this chapter.

Error Analysis

The density profile depends on several subsidiary measurements and models:

$$n = n(B, < \sigma v >_{exc}(T_{ec}), geometry, Z^{in}_{avg})$$

where B = measured brightness, and the other symbols are defined above. In this subsection, we discuss the errors in each term, finally combining the errors into an

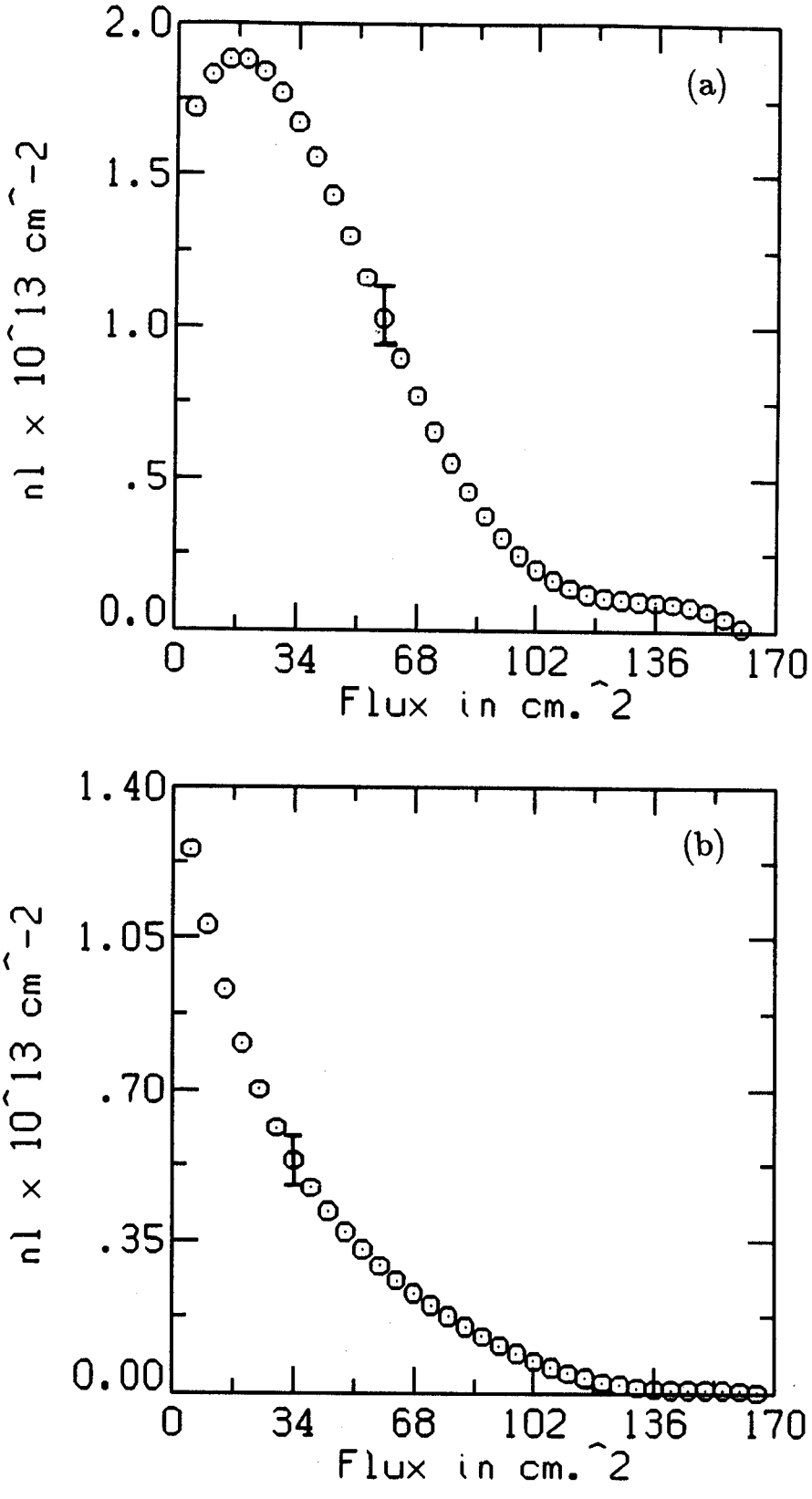

Figure 3-9: Axial line density profiles in (a) hydrogen and (b) argon plasmas are shown.

overall error estimate for the density profile.

- Brightness

  Because we are normalizing the overall density profile using the microwave interferometer, we need only consider the errors in the brightness B which arise from nonuniformity or shot–to–shot variations, and not the errors in the absolute calibration of the CCD camera. The pixel–to–pixel nonlinearity is measured at less than one percent. Shot–to–shot intensity variation is less than five percent.

- $< \sigma v >(T_{ec})$

  Because the dependence of $< \sigma v >$ on T_{ec} for the lines chosen is weak, the 40 percent uncertainty in the value of T_{ec} is reduced by a factor of four or more when the partial derivatives are calculated:

$$\frac{\Delta < \sigma v >}{< \sigma v >} = \frac{\partial < \sigma v >}{\partial T_{ec}} \frac{T_{ec}}{< \sigma v >}$$

  For example at 100 eV. in helium, $< \sigma v >$ is completely independent of T_{ec}. (The excitation cross section curves are shown in Appendix A.)

- geometry

  The ratio $\int n\, dl / \int dz = 1$ on axis, and deviates substantially from one only at the plasma edge. This leads to error bars which increase with magnetic flux. At the extreme edge ($\psi > 150 cm^2$ in helium) where the density is almost zero, the error in the density profile due to the geometrical term dominates, and the density is only known to within a factor of two. The profile error is much smaller ($<$ 10 percent) for the plasma region of interest ($\psi \leq 150 cm^2$). Changing the best fit parameters in the PLINEINT code changes the geometrical ratio by less than five percent near the center of the plasma.

- Z_{avg}^{in}

  Because we find that Z_{avg}^{in} is nearly independent of flux, an error in determining the correct value of Z_{avg}^{in} will have no effect on the density profile. Errors in

Z_{avg}^{in} will however have some smaller effect on the magnitude of the transport coefficients and confinement times, as discussed in Chapter 5.

- Normalization

  There would be considerably more error in the density normalization if we relied on the absolute calibration of the CCD camera to find the absolute density. Instead, we use the microwave interferometer, whose normalization has a much smaller error than that of the CCD camera.

Combining the sources of error discussed in this section produces the ten percent relative error bars shown in Figures 3-8 and 3-9.

3.3 Ionization Source Measurements

The ionization source is the number of atoms or molecules ionized by electron impact, per unit volume, per unit time. We are more interested in the field line averaged, flux averaged ionization source function:

$$S(\psi) = Z_{avg}^{end} \int n_0 n_e < \sigma v >_{ion} dl \tag{3.3}$$

$S(\psi)$ can be found from the line averaged brightness B(x,y) in a manner similar to the ion density measurement. The one additional quantity required in addition to those needed for the density measurement is the function I/P(T_{ec}), the number of ionization events which occur for each photon emission. The function I/P depends on the cold electron temperature and density, and can be calculated if the cross sections for all relevant atomic processes are known.

The value of I/P for Constance parameters is approximately 10 for the hydrogen H_α line, 750 for the helium 4922 $\AA$ line and 125 for the argon 6965 $\AA$ line. These three lines were chosen to make I/P as independent of T_{ec} as possible, thereby reducing the error in the ionization source function measurement. The function I/P for the 4922 $\AA$ line is shown in Figure 3-10, and scales approximately as $(T_{ec})^{1/2}$. I/P for other helium

lines depend more strongly on T_{ec}: For example I/P using 5876 $\mathring{A}$ line increases as $(T_{ec})^3$ in the region 40–80 eV. The detailed calculation of I/P is included in Appendix A, and is especially complicated for hydrogen, with its many atomic and molecular processes.

Once I/P and $T_{ec}(\psi)$ are known, the source function can be calculated by multiplying the photon emission rate on each flux surface by the number of ionizations per photon for that flux surface:

$$S(\psi) = Z_{avg}^{end} < \int B(x,y)\, dz (\int n\, dl / \int n\, dz) > I/P(T_{ec}(\psi)) \qquad (3.4)$$

where <> denotes an average over the flux surface. The total ionization source in Constance is in the range 200 mA. to 2 A. for the gasses and plasma parameters of this thesis. The ionization source profile is shown for a helium plasma under standard conditions in Figure 3-11. The source profile shape and magnitude in hydrogen and argon are similar to those in helium. They are shown in Figure 3-12. The coefficients needed to plot S(ψ) for all three gasses and also during application of low frequency RF power are tabulated at the end of this chapter.

Error Analysis

Similar to the density profile, the ionization source profile depends on several subsidiary measurements and models:

$$S = S(B, I/P(T_{ec}[R(\psi)], geometry)$$

Except for the function I/P, these are the same quantities whose errors were described in the previous section. The error in the function I/P is much less that the 40 percent error in the absolute value of T_{ec}. Since I/P is only a slowly varying function of T_{ec} as shown in Figure 3-10, the relative error is less than that in T_{ec}. After evaluating the partial derivatives, we find $\Delta(I/P)/(I/P)$ due to uncertainty in the temperature to be less than 25 percent if we desire absolute I/P, and less than 10 percent if we need only relative I/P. The error bars for the absolute and relative measurements of I/P are:

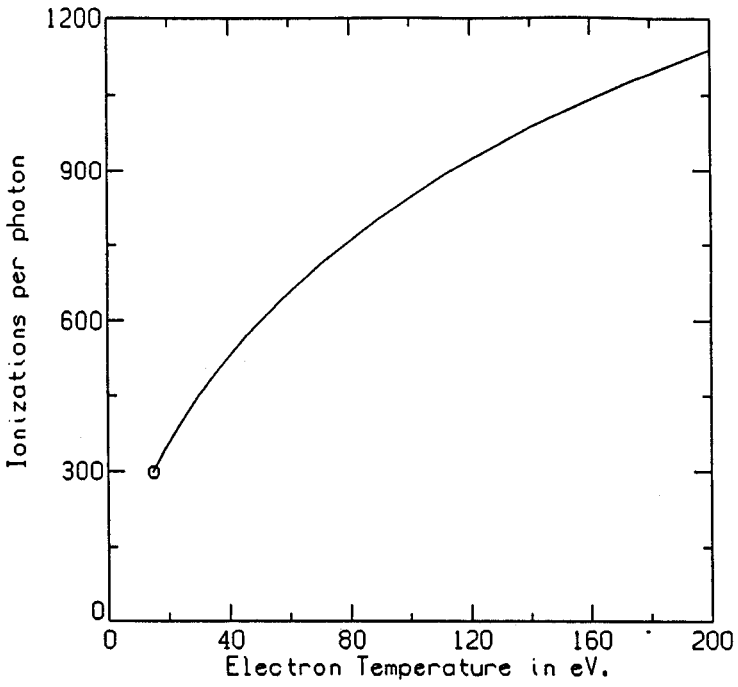

Figure 3-10: The number of ionizations per 4922 $\AA$ photon emitted in a helium plasma in Constance is used to calculate the ionization source. This curve, and similar ones for hydrogen and argon are calculated in Appendix A.

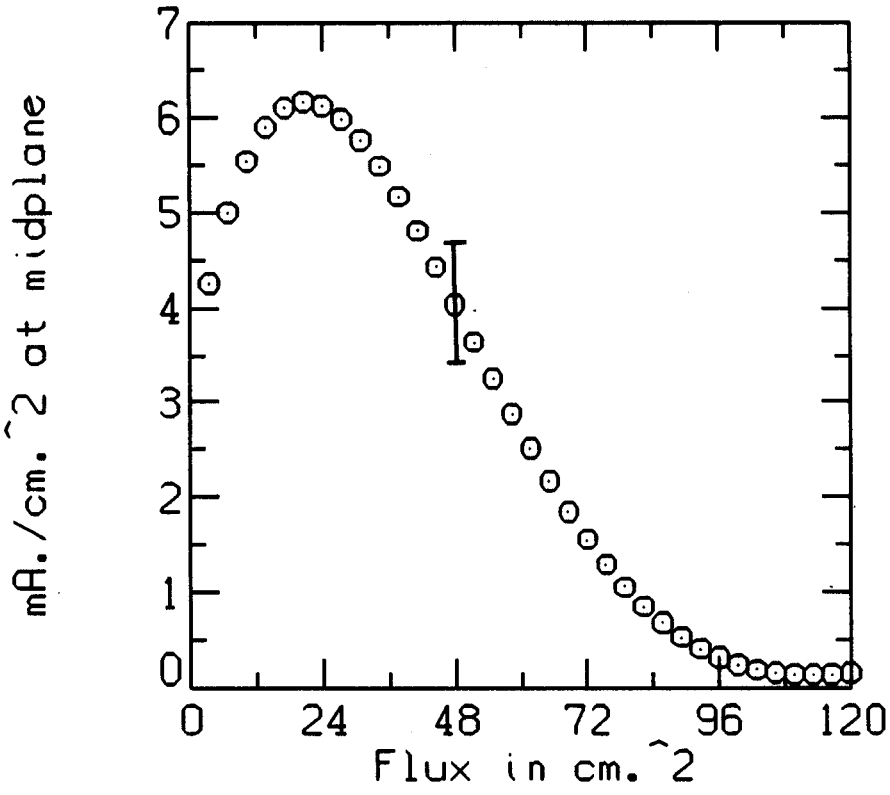

Figure 3-11: Ionization source profile in a helium plasma under standard conditions is shown.

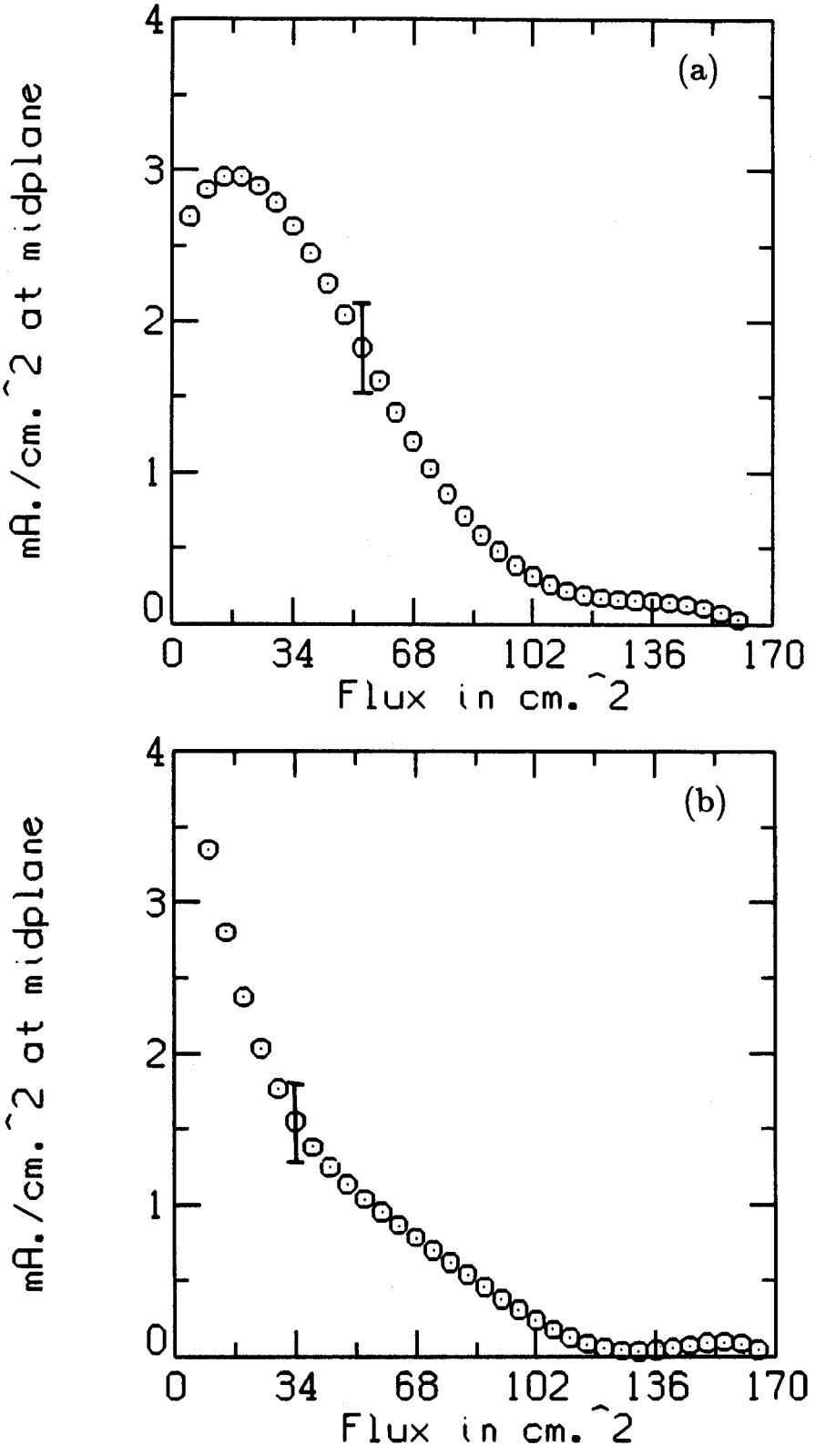

Figure 3-12: The ionization source profiles for (a) hydrogen and (b) argon plasmas are shown.

Absolute I/P:

$$\frac{\Delta(I/P)}{(I/P)} = \frac{\partial(I/P)}{\partial T_{ec}} \frac{\Delta T_{ec}}{(I/P)}$$

Relative I/P:

$$\frac{I/P(T_1 - \Delta T_{ec})}{I/P(T_2 + \Delta T_{ec})} < \frac{I/P(T_1)}{I/P(T_2)} < \frac{I/P(T_1 + \Delta T_{ec})}{I/P(T_2 - \Delta T_{ec})}$$

where T_1 and T_2 are two cold electron temperatures and ΔT_{ec} is the error T_{ec} error bar.

There is also an error in I/P due to the uncertainty in the experimental and theoretical cross sections used in calculating I/P. Although the uncertainty in magnitudes of $< \sigma v >_{exc}$ and $< \sigma v >_{ion}$ range from 10 percent for hydrogen to 50 percent for argon, the shapes of the cross sections are what really matter. The error in I/P due to uncertainties in cross sections is found to be also about 10 percent.

Combining the errors in brightness, I/P and geometrical effects leads to the 15 percent error bars shown in Figures 3-11 and 3-12.

3.4 Potential Measurements

The plasma potential ϕ inside the mirror throat is difficult to measure directly. If the axial potential profile is qualitatively the shape sketched in Figure 3-13 as suggested by Baldwin, [Baldwin, 1980] then ϕ at the midplane may be found by measuring ϕ_1 and ϕ_0. Here ϕ_1 is the ion confining potential dip due to the hot electrons, ϕ_0 is the maximum or "ambipolar" potential which confines electrons, and $\phi = \phi_0 - \phi_1$.

We can measure ϕ_0 using a gridded electrostatic end loss analyzer (ELA) with a swept ion repeller grid, as shown in Figure 2-5. The probe was mounted on a stalk and aligned using a laser beam and plumb bob as shown in Figure 3-14. When controlled by an electro–mechanical probe positioner, the ELA position could be controlled and monitored to within one mm.

Raw data from the ELA for a helium plasma under standard conditions, and a

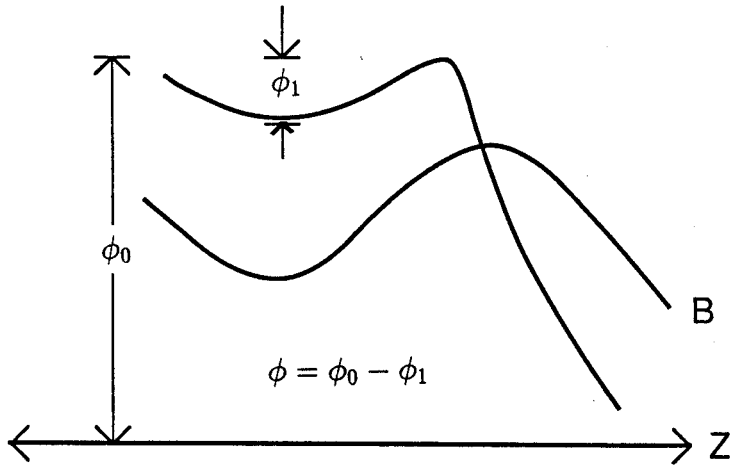

Figure 3-13: The assumed axial potential profile is shown. ϕ_0 is the ambipolar electron confining potential and ϕ_1 is the potential dip due to the hot electrons.

nonlinear least squares fit is shown in Figure 3-15. The fitting program[1] assumes flow confined ions. However, the "break" or "knee" voltage which determines ϕ_0 from the data is nearly independent of which ion confinement model is used.

The ambipolar potential ϕ_0 in helium is measured to be approximately 150 V. on axis, falling to about 130 V. at the plasma edge. During application of low frequency RF power, these values jump to 300 V. on axis and 270 V. at the edge. Figure 3-16 shows the radial profile of ϕ_0 both before and during application of RF power in helium. The values of ϕ_0 in hydrogen and argon are substantially different because the ion mass and charge state determine to a great extent the ion confinement time. ϕ_0 then adjusts itself to equilibrate the electron and ion confinement times. Coefficients which represent the ϕ_0 radial profile data in all three gasses are included at the end of this chapter.

The ion confining potential ϕ_1 can be deduced from the ion charge state, end loss and density profiles. Using the model described in section 3.2, a combination flow and Pastukhov confinement time is used to calculate ϕ_1 from the ion end loss and density

[1]The ELA fitting program was written by Craig Petty.

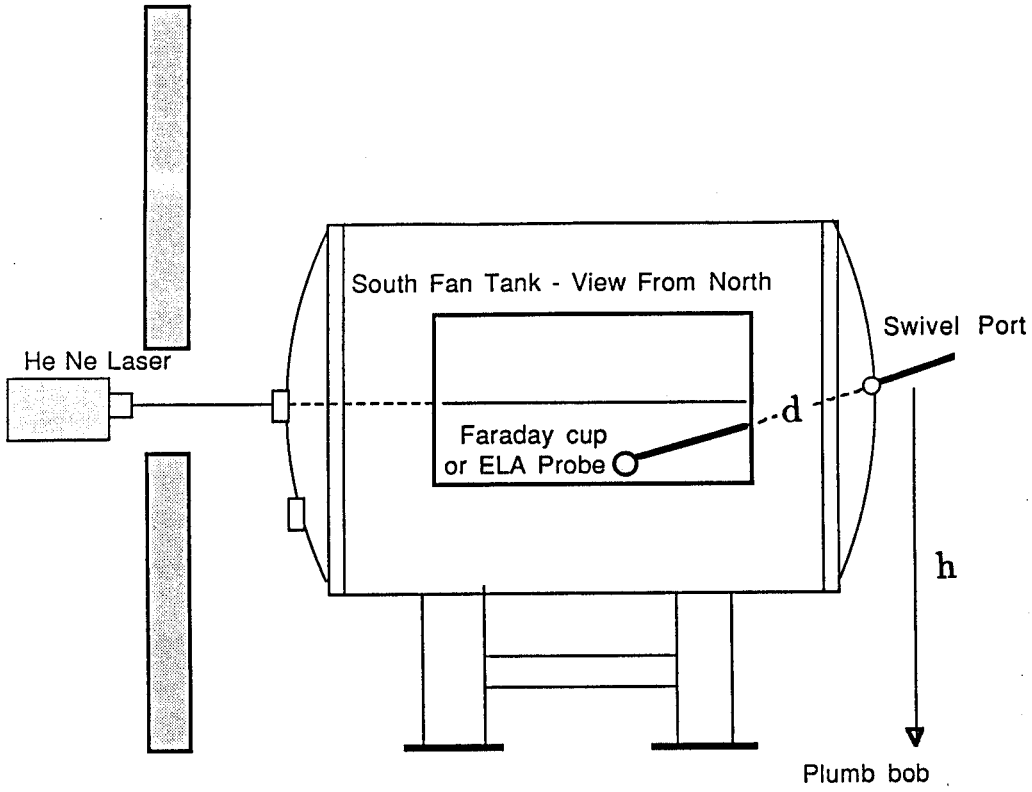

Figure 3-14: Faraday cup and ELA probes are aligned using a laser beam and a plumb bob.

profiles. The profile of ϕ_1 is found to be peaked on axis, with a value ϕ_1/T_i of order unity, falling to zero at the radius where the hot electron density is also essentially zero. The profile of ϕ_1 for helium is shown in Figure 3-17.

The potential ϕ obtained by combining ϕ_0 measured by the ELA and ϕ_1 deduced from ion end loss and density measurements is shown in Figure 3-18.

Error Analysis

Although the profile directly found from experimental measurements is the radial potential $\phi(\psi)$, it is the derivative of this profile, the radial electric field, which is used for transport calculations.

The estimate of the error in the radial electric field is the most important and the most difficult in the error analysis. Suppose the error in $\phi(\psi)$ is known, and the

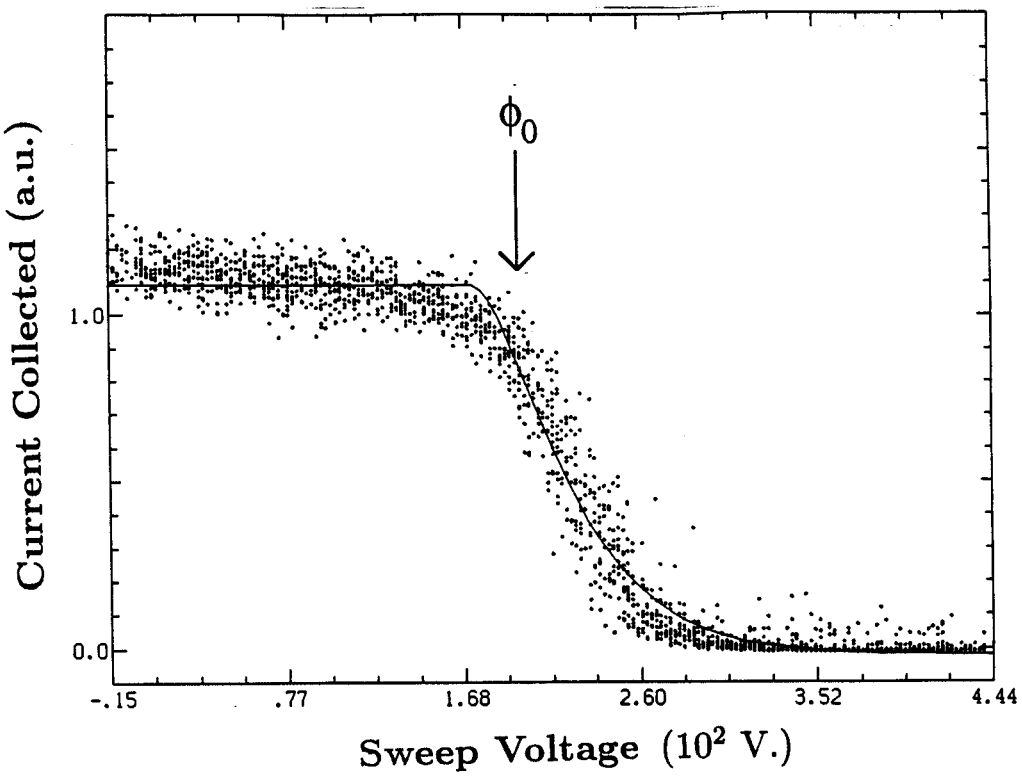

Figure 3-15: The I–V characteristic from the ELA probe is shown, along with a nonlinear least square fit which assumes flow confined ions. Because the ions "fall down" the electron confining potential ϕ_0 on their way out the mirror, ϕ_0 shows up as the break point in the curve.

variance is σ_ϕ^2. The average value of the radial electric field between ψ_1 and ψ_2 is:

$$\phi\prime(\psi) = \frac{\phi(\psi + \Delta\psi)}{\Delta\psi} \equiv \frac{\phi_2 - \phi_1}{\Delta\psi} \tag{3.5}$$

and using the formula for propagation of errors [Bevington, 1969]

$$\sigma_{\phi\prime}^2 = (\frac{1}{\Delta\psi})^2(\sigma_1^2 + \sigma_2^2 + 2\sigma_{12}^2) \tag{3.6}$$

Since the errors are independent and equal:

$$\sigma_{\phi\prime} = \sqrt{2}\sigma_\phi/\Delta\psi \tag{3.7}$$

This means that to keep the error bars in $\partial\phi/\partial\psi$ a reasonable size one can only speak of the average electric field over a region $\Delta\psi$. The larger the region one averages over, the smaller the error.

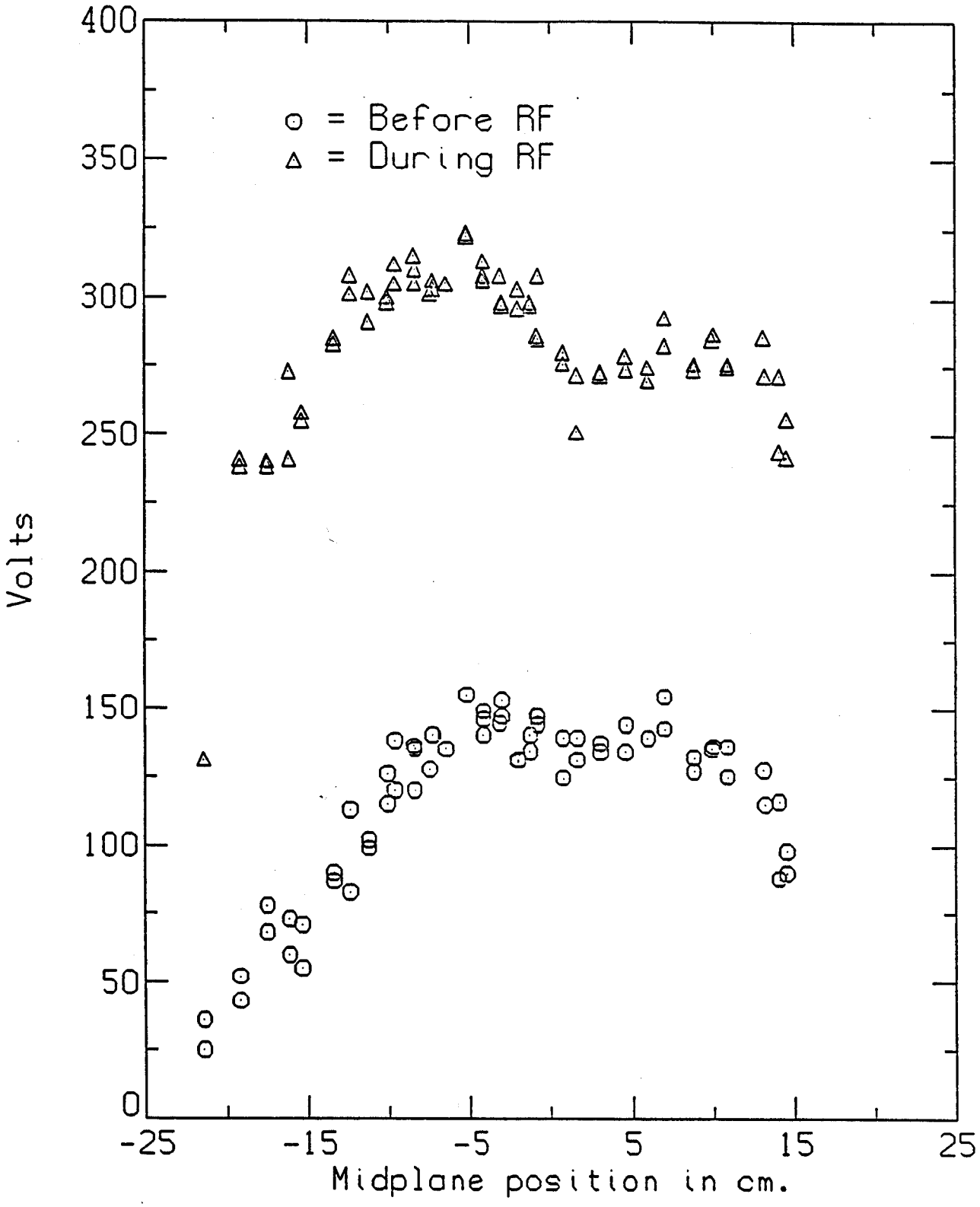

Figure 3-16: The electron confining potential as measured by an ELA probe in helium is shown. The potential increases when low frequency RF power is applied.

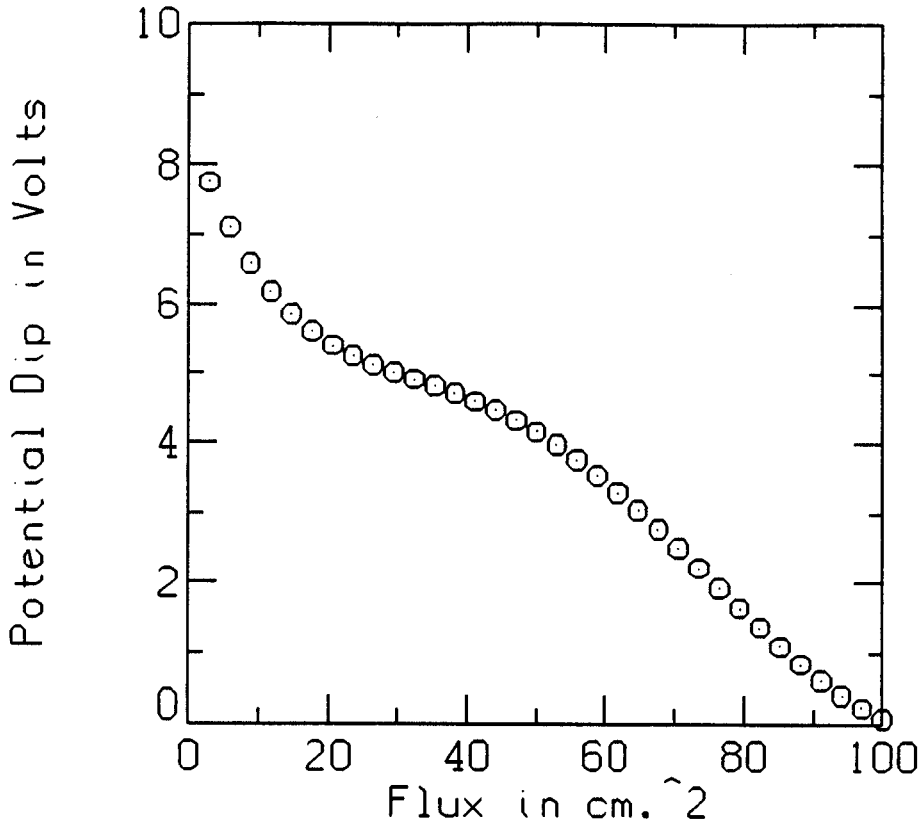

Figure 3-17: The potential dip ϕ_1 due to hot electrons increases the ion parallel confinement time. It is deduced from the ion density and end loss, and shown here for helium.

The variance $\sigma^2_{\phi'}$ is due to errors in both ϕ_0 and ϕ_1, but the error from ϕ_0 is usually the dominant contribution. The scatter in Figure 3-16, is about σ = 10–15 Volts, or 10 percent. The error in positioning the ELA probe is $\leq$ 0.5 cm. at the midplane for each measurement. Again, averaging over flux tubes makes this error negligible.

At the plasma edge the swept ELA signal has more scatter and is not as well fit by a function which is flat out to the break point. We have shown this to be at least partially due to the increased angle between the field lines and the ELA probe. At the plasma edge $\sigma_\phi \simeq 10$ V. or $\Delta\phi/\phi < 10$ percent. The shot–to–shot variation in ϕ_0 for these plasmas is < 5 percent.

The ion confinement potential ϕ_1 also contributes to σ^2_ϕ, but the logarithmic dependence of ϕ_1 on parameters and the small value of ϕ_1 usually causes ϕ_0 to be the

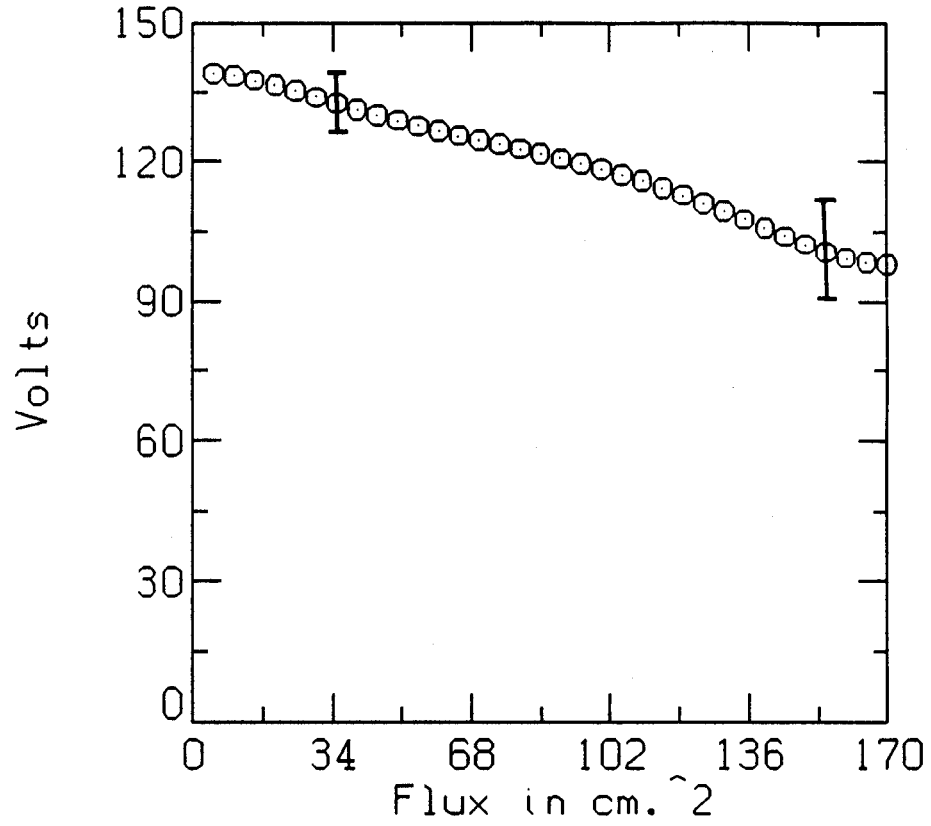

Figure 3-18: Combining the previous two figures gives the potential in helium: $\phi = \phi_0 - \phi_1$.

dominant term. Solving the Pastukhov formula for ϕ_1:

$$\frac{\phi_1}{T_i} \exp \frac{\phi_1}{T_i} = l(\psi) n(\psi) T_i^{-3/2} Z_{eff}^2 J^{-1}(\psi) \tag{3.8}$$

For error analysis, an upper limit on $\sigma_{\phi 1}$ is obtained by approximating:

$$\phi_1/T_i \sim \ln(Z_{eff}^2 n l T_i^{-3/2}/J) = \ln u \tag{3.9}$$

The error bars for ϕ_1/T_i are: [Bevington, 1969]

$$\sigma_{(\phi 1/T_i)} = \sigma_u/u \tag{3.10}$$

Here $l(\psi)$ is the effective plasma length found by integrating a best fit density profile in the PLINEINT code, which should be quite accurate ($\Delta l/l < 20$ percent). If the other two terms have accuracies < 25 percent, as believed, then Equation 3.10 gives:

$$\sigma_{\phi 1/T_i} \leq 0.3 \tag{3.11}$$

T_i is measured to be independent of radius. For helium it would take a ΔT_i of 50 percent for the error in ϕ_1 to be larger than that in ϕ_0, so this uncertainty is probably not important. This conclusion turns out to also be true in hydrogen and argon even though the contribution of ϕ_1' to the radial electric field is larger than in helium. The total error is then:

$$center : \Delta\phi = \sqrt{(\Delta\phi_1)^2 + (\Delta\phi_0)^2} = \sqrt{9 + 25} \simeq 6V.$$

$$edge : \Delta\phi = \sqrt{9 + 100} \simeq 10V.$$

Combining with Equation 16. leads to the error bars of Figure 3-18.

3.5 End Loss Measurements

To determine the ion end loss profile in Constance, a two–dimensional faraday cup scan was performed in the south fan tank. A one–dimensional scan was also done in the north fan tank to ensure that the end loss is north–south symmetric with quadrupole symmetry. The end loss profiles in the north and south fan tanks were found to be indistinguishable within the error bars of the measurement. Data presented in this thesis is therefore only from the 2-d south faraday cup scan.

The experimental setup is sketched in Figure 3-14. Laser alignment keeps z constant as the probe is moved along y. (z is the magnetic axis direction., x the thin direction of the fan, as shown in the figure.) A plumb bob, when compared against a line drawn on the floor, ensures that z is constant when x is changed. Measuring d and h as shown then determine the probe coordinates to within 0.5 cm. at the center of the fan tank and to within 0.25 cm. at the edge.

Raw data using this setup is shown in Figure 3-19. The center of the fan tank is defined as (x,y)=(0,0). The magnetic y axis in the center of the fan tank was found to be at a 2.3 degree angle with respect to the horizontal, and the data is plotted and analyzed using the magnetic rather than geometric axis.

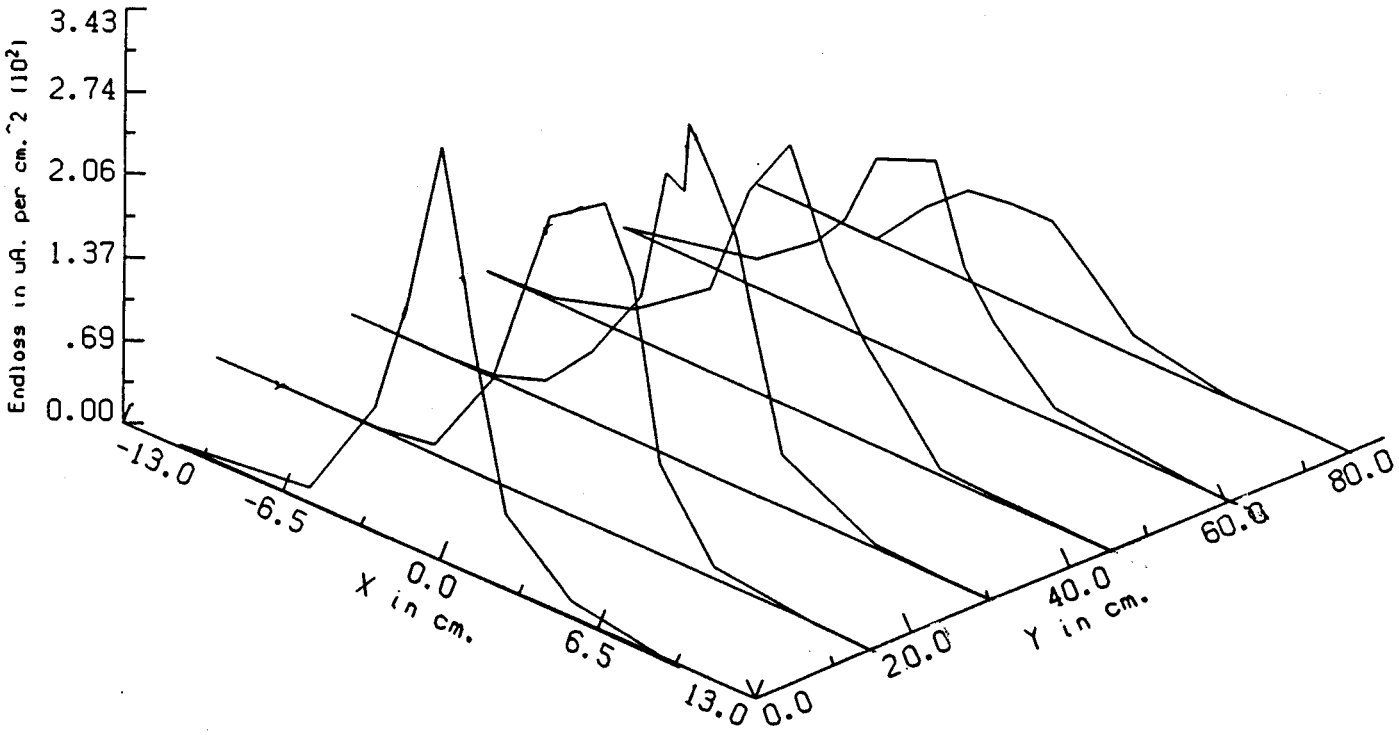

Figure 3-19: Raw end loss ion current collected by a faraday cup probe in the south fan tank is shown.

At large Y, field lines intersect the faraday cup probe at an angle, reducing the current collected. This angle is shown in Figure 3-20. Figure 3-21 shows the result of a calibration experiment to correct for this effect.

For the calibration experiment, the faraday cup probe, located on axis, was moved and tilted in such a way that the flux directed at the entrance aperture was held constant, while the angle between the flux and the probe was changed. An ideal probe, negligible in depth, would have a $\cos\theta$ angular dependence. For the positions available in the fan tank, a $\cos\theta$ distribution matches the calibration data fairly well. The raw data and a $\cos\theta$ fit are shown in Figure 3-21. Contours of end loss are shown in Figure 3-22. A two–dimensional spline fit produced these contours.

We would like to plot the end loss current $J(\psi)$ mapped back to the midplane, to compare with the source function in the plasma. This mapping was done using the

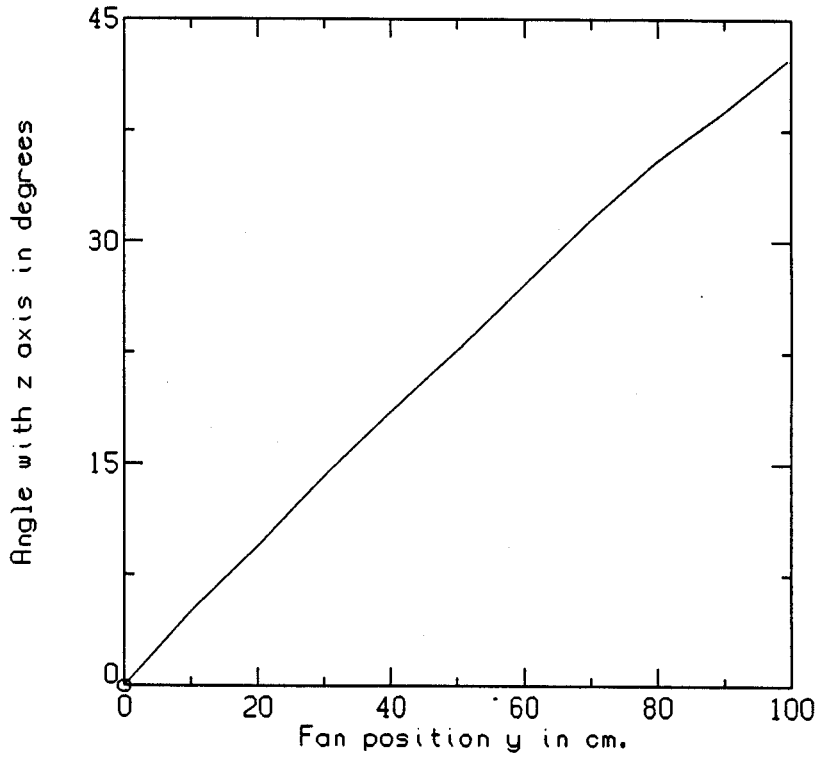

Figure 3-20: The angle at which field lines hit the probe is shown.

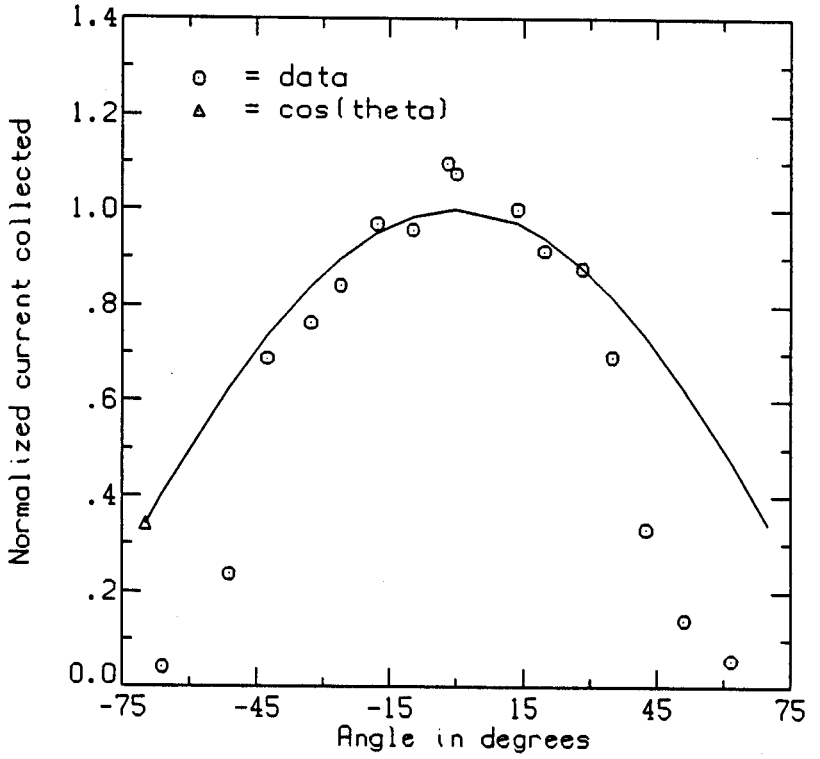

Figure 3-21: Calibration data and a $\cos\theta$ fit are shown.

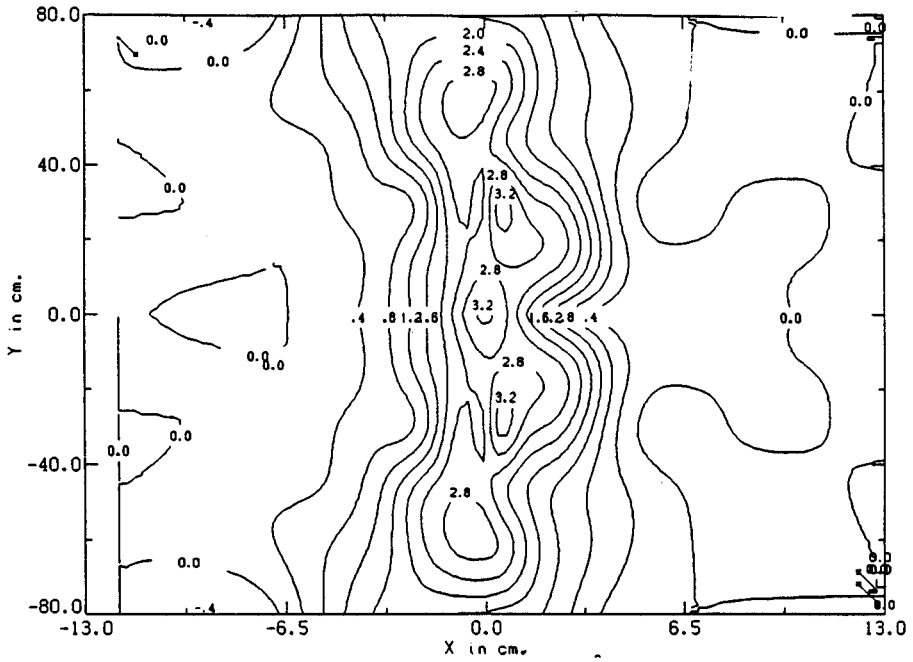

Figure 3-22: Contours of constant ion end loss current in the fan tank for a helium plasma under standard conditions are shown.

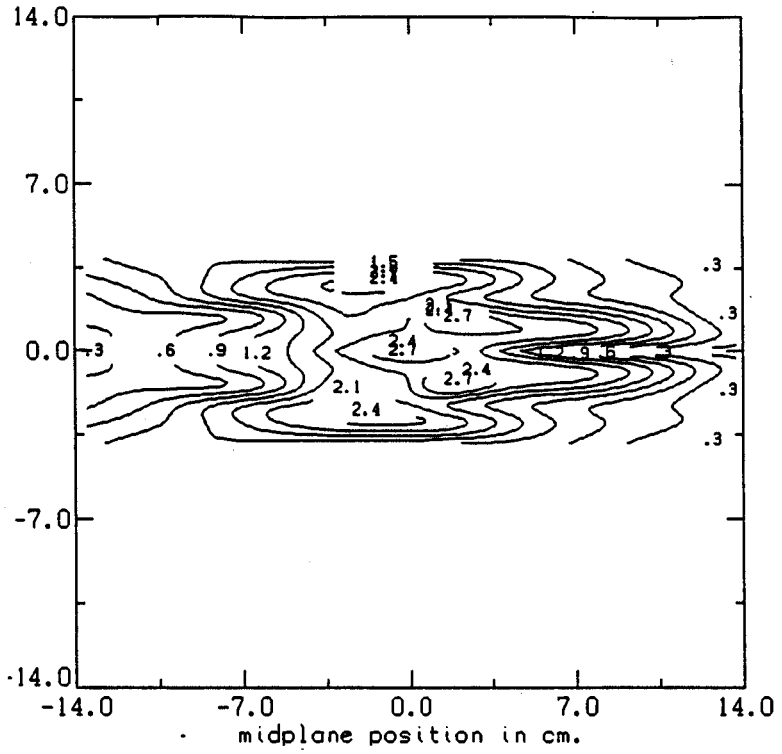

Figure 3-23: Contours of constant ion end loss current mapped to the midplane for a helium plasma under standard conditions are shown.

code EFFI, [Sackett, 1978] by numerically following field lines in the Constance magnetic field. The end loss was measured in two dimensions to allow a self consistency check of this mapping. For a given Z, EFFI (and a long-thin calculation) predict that the midplane position (x_0, y_0) should map to (ax_0, by_0) where a and b are nearly independent of midplane radius $r_0 = \sqrt{x_0^2 + y_0^2}$.

The ellipticity $\epsilon = b/a$ predicted by EFFI for the position of the entrance aperture of the faraday cup probe is 64.1. (b=20.7, a=0.32) The maximum y value accessible in the fan tank is 80 cm., so the ellipticity of the closed contours of end loss flux for $r_0 < 80/b = 3.9cm.$ is a quantity obtainable from the data. The end loss data shows an ellipticity of approximately that predicted by EFFI. Figure 3-23 shows the two dimensional end loss contours mapped back to the midplane using the EFFI mapping. The central 3.9 cm. have closed contours with effective ellipticity near 1. This again shows consistency between the end loss data and the EFFI mapping.

Figure 3-24 is a plot of the end loss which averages the splined data of Figure 3-22 over flux surfaces. This is the data that can be used to compute transport coefficients. End loss current profiles $J(\psi)$ for hydrogen and helium plasmas are shown in Figures 3-25(a) and (b). Note that the argon endloss profile is much wider than the hydrogen or helium end loss.

Error Analysis

Random errors in the end loss profile $J(\psi)$ come from inaccuracies in positioning of a faraday cup probe and random shot–to–shot variations. Using the physical setup sketched in Figure 3-14 we can position the probe to within 0.5 cm. on axis, which maps to 1.5 cm. at the midplane. Since the current profile changes by 50 percent in 5 cm., this leads to < 15 percent error bars for each point. Shot–to–shot variation is substantially smaller than this, and we also average over many shots.

We have no reason to distrust the output from the EFFI code, and our confidence is bolstered by the self consistency check described earlier in this section.

Finite Larmor Radius (FLR) effects are not important for the hydrogen and helium

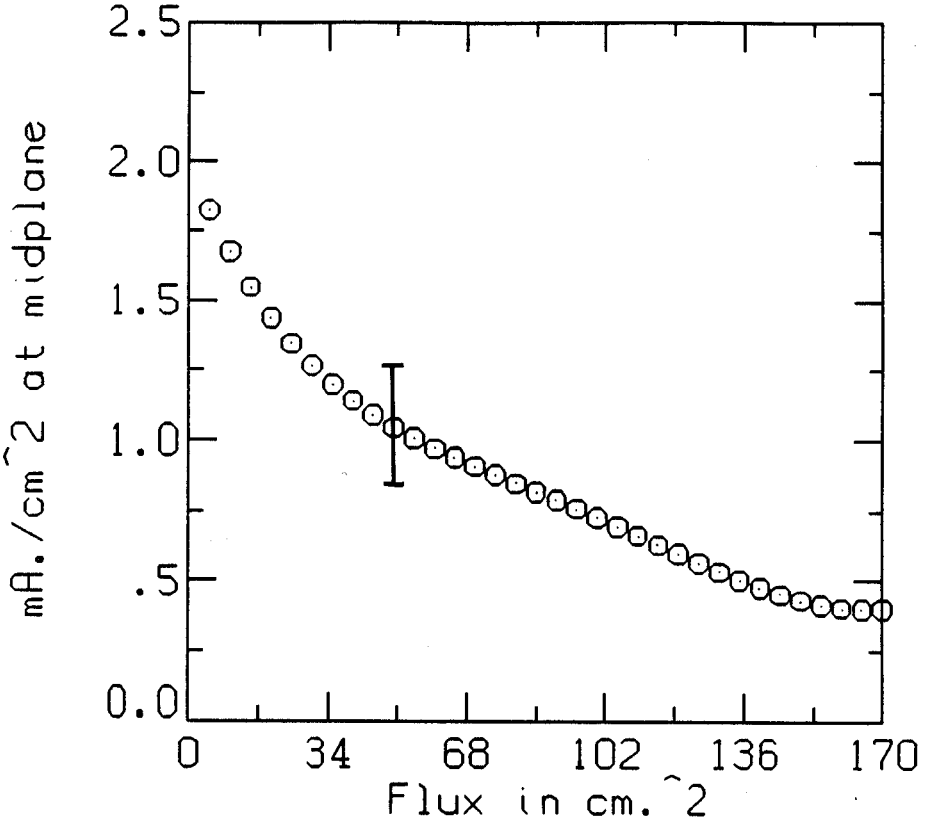

Figure 3-24: Flux averaged ion end loss current $J(\psi)$ for a helium plasma under standard conditions are shown.

ions. (As tabulated in Table 4.1, ρ_i for these ions is measured in mm.) The Larmor radius for argon ions is close to a cm., so the argon end loss profile is inverted to take into account FLR effects. The resulting profile is slightly more peaked than the raw data. In general the error introduced by using an uninverted argon end loss profile is in the 10 percent range at the center and practically zero at the edge.

The drift of the guiding center off field lines due to curvature in the fan tank is less than 1 mm. (This was calculated both analytically and using the GCDRIFT code) [Devoto, 1986]. The $\cos\theta$ model of Figure 3-21 is only an approximation to the actual angular correction. At the largest angles in the fan tank the data of Figure 3-21 indicates the actual correction is within 15 percent of $\cos\theta$. The error is less than this at small angles.

Combining all these uncorrelated errors leads to the error bars of Figure 3-24.

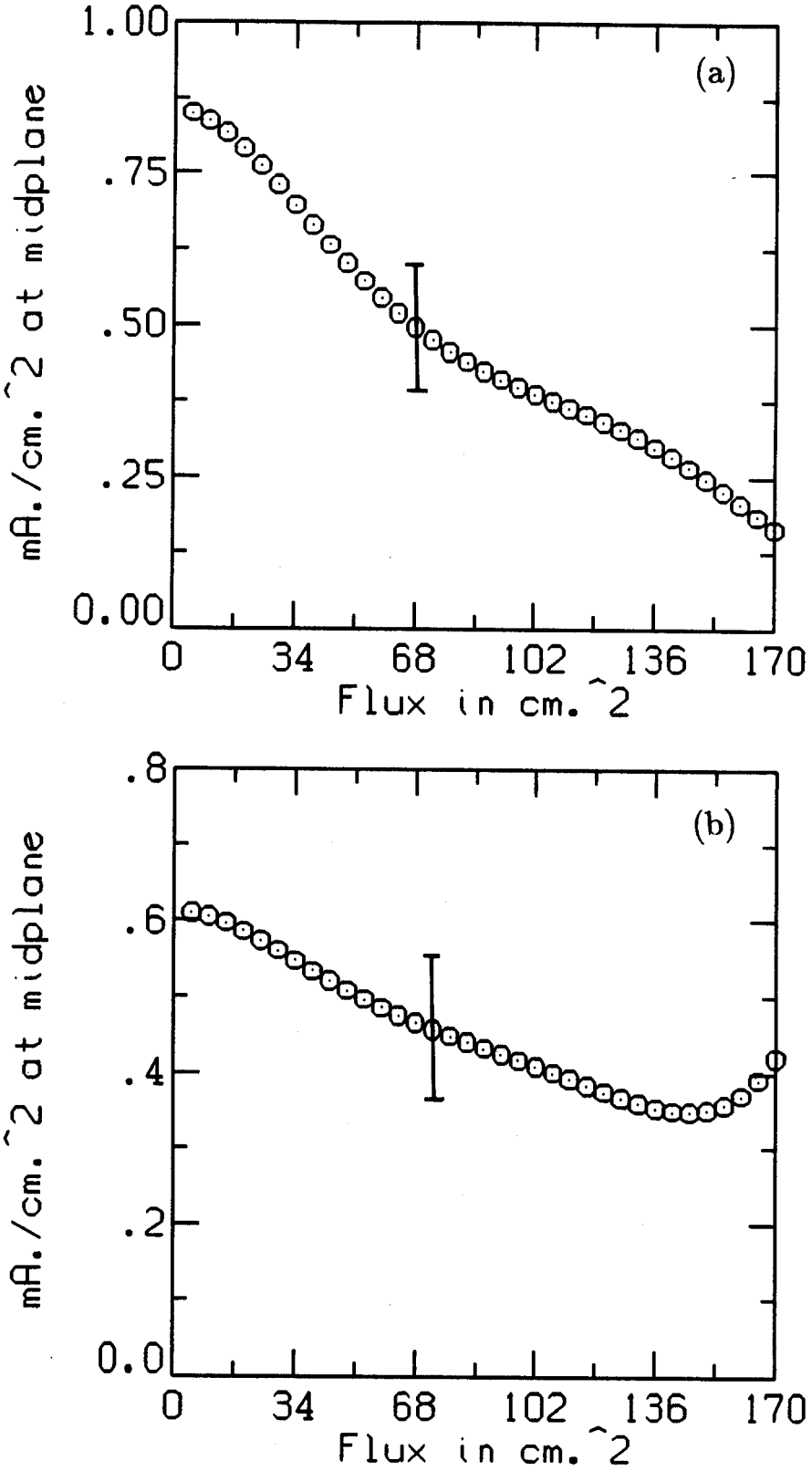

Figure 3-25: Ion end loss profiles $J(\psi)$ for (a) hydrogen and (b) argon plasmas are shown.

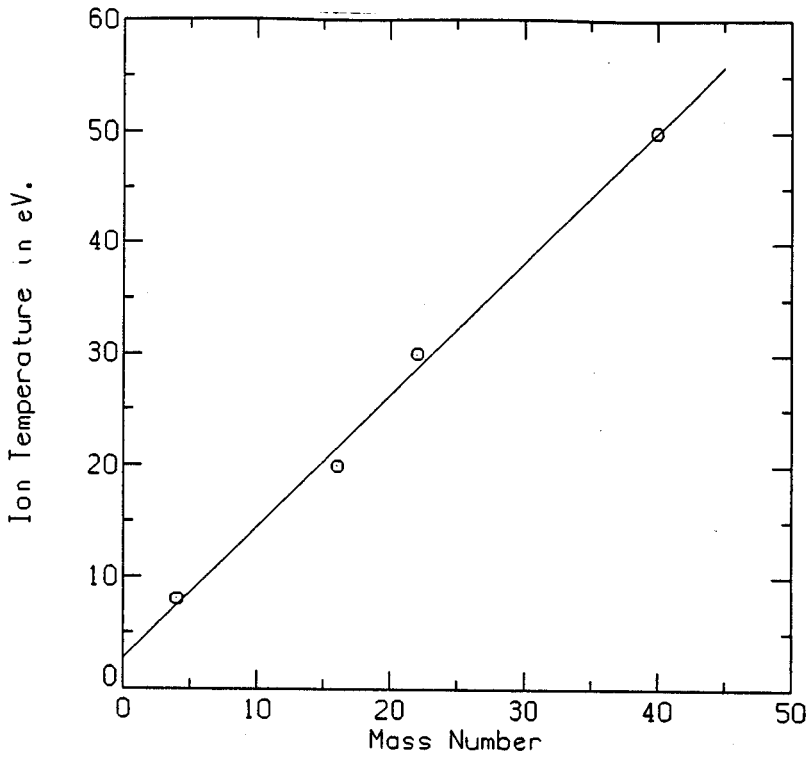

Figure 3-26: Ion temperatures measured using the Optical Multichannel Analyzer (OMA) are shown. These temperatures scale linearly with mass, and agree with Time–of–Flight (TOFA) rise times [Petty, 1988].

3.6 Ion Temperature Measurements

The ion temperature was measured using two methods. The Optical Multichannel Analyzer (OMA) was used to record emission spectra from many ion lines. The Doppler broadening of these lines due to finite ion temperature was found after the inherent instrumental resolution was taken into account. The resultant temperatures for the first charge state are shown in Figure 3-26. The ion temperatures increase linearly with mass. Higher charge states are measured to be slightly hotter (maybe 20 percent) than the first charge state [Petty, 1988].

For hydrogen, whose ions of course have no electrons and thus no emission lines to measure, a temperature of 5 eV. is used in this thesis. This is based on an extrapo-

lation of the least squares linear fit to the data in Figure 3-26, as well as the rise time for hydrogen ions measured in the end loss by the Time–of–Flight analyzer. (TOFA)

From Equation 2.2, the signal from TOFA spreads out if there is a spread in the ion energies. The ion temperatures obtained in this fashion agree with those found using the OMA Doppler line broadening. We find temperature of 5, 8, and 50 eV. for the first charge states of hydrogen, helium and argon, respectively.

During application of low frequency RF power, the temperature of ions whose cyclotron frequency is resonant with the applied frequency increases by a factor of 2–20 depending on plasma parameters and RF power. Nonresonant ions are not heated by the low frequency RF power.

Figure 3-27 shows the temperature of He^{+1} ions versus time as measured by Doppler broadened spectral lines. The figure clearly shows heating by resonant RF waves, increasing T_i by a factor of 3.5.

3.7 Polynomial Fits

Polynomials were fit to the radial profiles of end loss, ionization source, density and potential to describe the many profiles in a compact way. The polynomials are of the form:

$$F(\psi) = \sum_{n=0}^{n=nmax} C_n \psi^n \tag{3.12}$$

The degree of the polynomial used (nmax) ranges from two to five. Data which has less scatter justifies fitting by a higher order polynomial which preserves more of the curves detailed features. The coefficients for hydrogen, helium and argon are given in Tables 3.3, 3.4 and 3.5. The line density coefficients are given in dimensionless units in the table. To convert to units of $10^{13} cm^{-2}$, the line density coefficients must be multiplied by the coefficient a given in Table 3.2. This parameter is found using the microwave interferometer, whose signal for a helium plasma is shown in Figure 3-28 (a), with the end–of–shot decay expanded in Figure 3-28 (b). From the ratio of fast and slow decays we find the hot electron fraction is 0.48 for these parameters. This

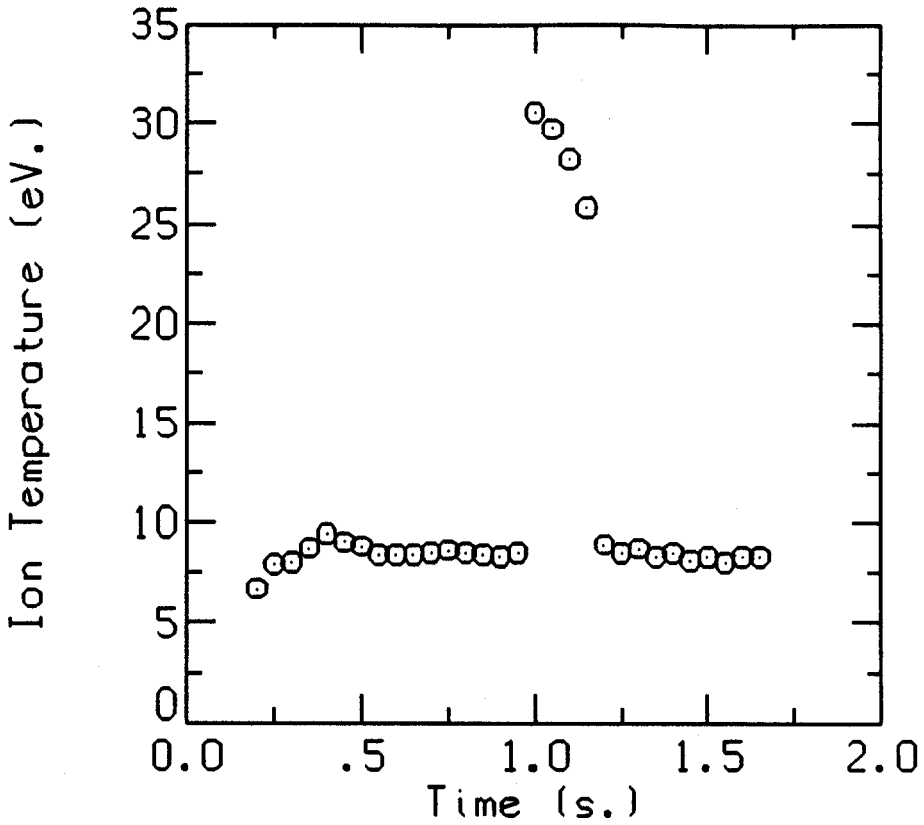

Figure 3-27: Helium ion temperature as measured by Doppler broadened spectral lines is shown. The increase in T_i is due to the application of resonant RF power.

process is described in theses by Garner and Hokin [Garner, 1986,Hokin, 1987].

The interferometer signal in helium, averaged over several shots gives a perpendicular line density $nl_\perp = 0.684 \times 10^{13} cm^{-2}$. The line density in hydrogen are argon are smaller than in helium, usually half to 75 percent the helium value.

The plasma length $L_p = 40 - 1.33\psi^{1/2}$ is a least squares fit to EFFI data for the length of a field line inside the mod–B surface with mirror ratio $R_m = 1.37$. This length was chosen to be consistent with the best fit plasma parameters in the PLINEINT code.

Combining the interferometer signal, the plasma length and axially integrated density profile from the CCD camera, the constant a is:

$$a = \frac{nl_\perp}{\int_{\psi=0}^{\psi_{edge}} \sum_0^5 C_n \psi^n d\psi / (40\psi^{1/2} - 1.33\psi)}$$

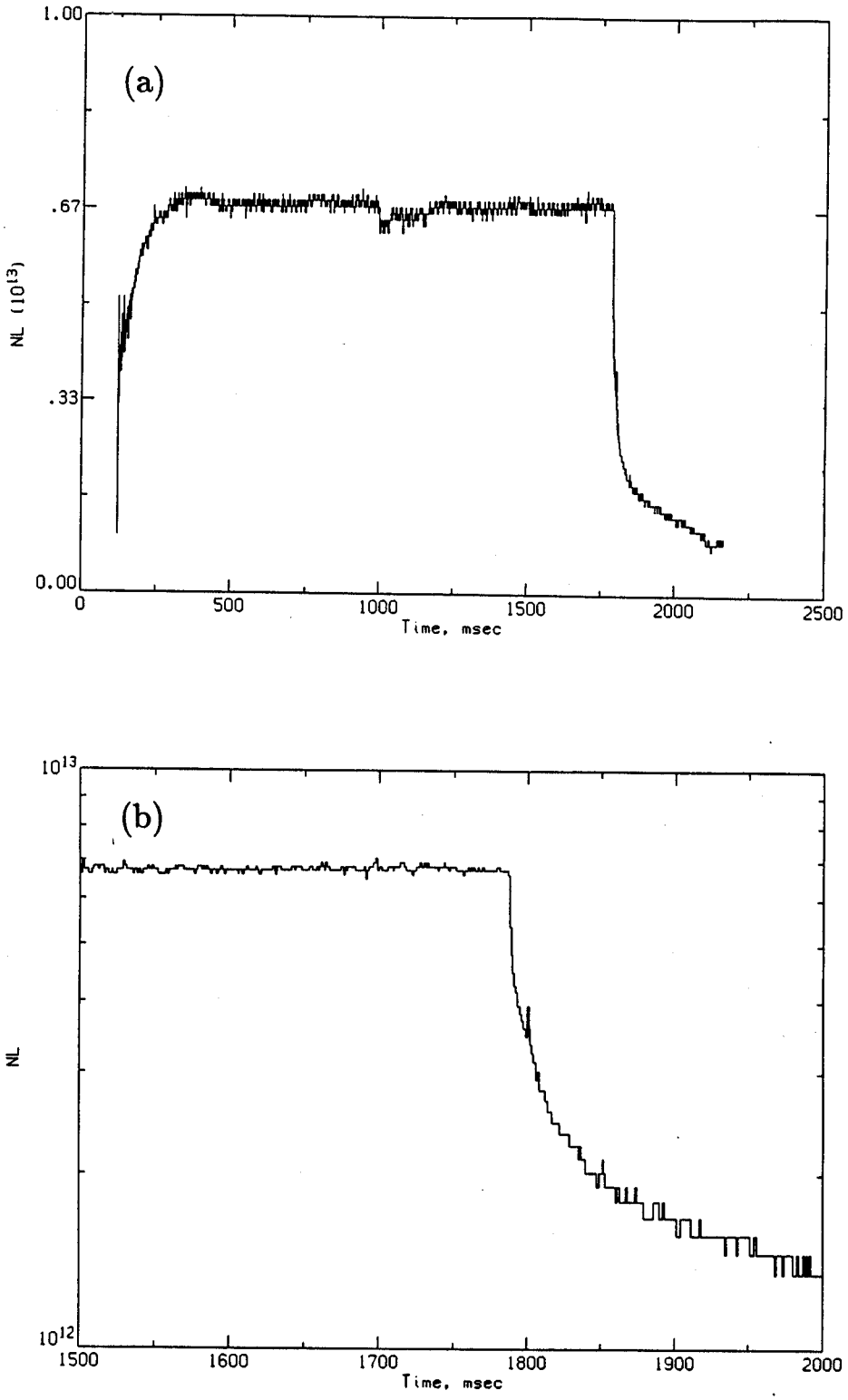

Figure 3-28: (a) The microwave interferometer measured the perpendicular line density. (b) The decay of the interferometer shows two decay times: The cold electrons leave the machine within a millisecond, whereas the hot electrons leave on a 100 ms timescale. The decay shape therefore allows an estimate of the hot and cold electron fractions.

Source Gas	a before RF $(10^{13} cm^{-2})$	a during RF $(10^{13} cm^{-2})$
Hydrogen	1.92	1.68
Helium	4.05	3.37
Argon	1.51	1.60

Table 3.2: The line density $\bar{n}$ is multiplied by these coefficients to convert from normalized units to physical units.

where ψ_{edge} is the value of ψ at the plasma edge, $\psi \simeq 169 cm^2$.

Substituting the interferometer values for $nl_\perp$ gives the normalization results shown in Table 3.2.

and other ions. Like–like ion collisions cause no displacement of the average guiding center location of the two ions, and thus lead to very little radial diffusion. Collisions between ions of different masses or charge states do lead to displacement of the average guiding center and to diffusion. We define an effective collision frequency:

$$\nu_i = \sum_{j \neq i} \nu_{ij} + \nu_{ie} + \nu_{in} \tag{4.1}$$

where ν_{ij} is the collision rate of ion species i with ion species j:

$$\nu_{ij} \simeq 5 \times 10^{-8} n_j Z_i^2 Z_j^2 \ln \Lambda T_i^{-3/2} sec^{-1}$$

ν_{ie} is the ion–electron collision frequency, ν_{in} is the ion–neutral collision frequency, the density is in cm^{-3} and T_i is in eV.

Using this simple model for collisions, the classical diffusion coefficient is:

$$D_{\perp i} = \rho_i^2 \nu_i \tag{4.2}$$

where ρ_i is the ion Larmor radius.

For Constance parameters, the first term in Equation 4.1 dominates. This is true even in hydrogen, because there are two ion species (H^+ and H_2^+) with approximately equal densities. Equation 4.2 is consistent with a careful multi–component fluid derivation of the classical diffusion coefficient [Braginskii, 1965]. Classical diffusion is then equivalent to a one dimensional random walk with a step size of an ion Larmor radius.

Table 4.1(a) shows the Larmor radius and effective collision frequency on axis for several ion species under typical Constance parameters. Table 4.1(b) shows the value of D_{cl} on axis for hydrogen, helium and argon plasmas after averaging over charge state. Since the classical diffusion coefficient is proportional to density, and the density falls off radially, the entries in Table 4.1(b) represent a maximum value. The average over charge states is computed using:

$$D_{avg} = \frac{\sum D_i \, dn_i/d\psi}{dn/d\psi} \tag{4.3}$$

Hydrogen Before RF	C_0	C_1	C_2	C_3	C_4	C_5
ϕ_0 (Volts)	138.5	-0.1858	5.9614e-5			
Normalized Line Density	0.8011	2.359e-2	-9.096e-4	9.403e-6	-3.907e-8	5.538e-11
ϕ_1/T_i dimensionless	2.40	1.439e-2	2.856e-4	-1.738e-5	1.591e-7	-4.28e-10
Endloss Flux/2 (mA./cm^2) midplane	0.8537	2.284e-4	-2.397e-4	3.508e-6	-1.988e-8	3.922e-11
Ionization Source/2 (mA./$cm.^2$)	1.200	3.665e-2	-1.410e-3	1.472e-5	-6.222e-8	9.089e-11
During RF						
ϕ_0 (Volts)	368.2	-2.903e-2	-2.043e-3			
Normalized Line Density	0.9609	-2.726e-3	-6.248e-4	1.179e-5	-7.910e-8	1.806e-10
ϕ_1/T_i dimensionless	2.878	8.099e-2	-4.590e-3	7.282e-5	-4.754e-7	1.095e-9
Endloss Flux/2 (mA./cm^2) midplane	0.2868	-3.718e-3	9.566e-5	-1.3797e-6	8.644e-9	-1.947e-11
Ionization Source/2 (mA./$cm.^2$)	0.8920	-1.9342e-3	-6.027e-4	1.1253e-5	-7.5234e-8	1.7148e-10

Table 3.3: Hydrogen polynomial coefficients

Helium Before RF	C_0	C_1	C_2	C_3	C_4	C_5
ϕ_0 (Volts)	147.7	-0.3005	1.4405e-4			
Normalized Line Density	0.8422	-3.306e-2	8.029e-4	-1.068e-5	6.655e-8	-1.515e-10
ϕ_1/T_i dimensionless	1.069	-3.761e-2	1.287e-3	-2.193e-5	1.557e-7	-3.808e-10
Endloss Flux/2 (mA./cm^2) midplane	1.998	-3.734e-2	5.499e-4	-4.418e-6	1.548e-8	-1.665e-11
Ionization Source/2 (mA./$cm.^2$)	1.636	0.1619	-5.660e-3	6.512e-5	-3.197e-7	5.74e-10
During RF						
ϕ_0 (Volts)	298.3	-0.129	-9.462e-5			
Normalized Line Density	0.8747	-1.742e-2	1.2754e-4	-7.305e-7	5.208e-9	-1.6447e-11
ϕ_1/T_i dimensionless	0.722	-1.050e-2	9.81e-5	-2.117e-6	2.087e-8	-6.21e-11
Endloss Flux/2 (mA./cm^2) midplane	0.9751	1.378e-3	-3.481e-4	5.942e-6	-3.939e-8	9.214e-11
Ionization Source/2 (mA./$cm.^2$)	1.986	0.1286	-5.797e-3	7.839e-5	-4.418e-7	8.988e-10

Table 3.4: Helium polynomial coefficients

Argon Before RF	C_0	C_1	C_2	C_3	C_4	C_5
ϕ_0 (Volts)	264.3	-5.355e-2	-7.281e-5			
Normalized Line Density	0.9662	-3.035e-2	5.016e-4	-4.803e-6	2.364e-8	-4.546e-11
ϕ_1/T_i dimensionless	0.560	-1.882e-2	4.813e-4	-6.324e-6	3.665e-8	-7.615e-11
Endloss Flux/2 (mA./cm^2) midplane	0.6103	5.162e-4	-1.265e-4	2.125e-6	-1.489e-8	3.785e-11
Ionization Source/2 (mA./$cm.^2$)	2.440	-9.664e-2	2.0577e-3	-2.3282e-5	1.2652e-7	-2.5907e-10
During RF						
ϕ_0 (Volts)	481.3	4.616e-2	-4.632e-5			
Normalized Line Density	0.956	-3.787e-2	8.064e-4	-9.124e-6	4.958e-8	-1.0153e-10
ϕ_1/T_i dimensionless	0.5381	-1.8142e-2	4.5198e-4	-5.875e-6	3.403e-8	-7.094e-11
Endloss Flux/2 (mA./cm^2) midplane	0.6185	5.278e-3	-2.623e-4	2.868e-6	-1.359e-8	2.471e-11
Ionization Source/2 (mA./$cm.^2$)	2.8696	-0.1137	2.4205e-3	-2.7387e-5	1.4882e-7	-3.047e-10

Table 3.5: Argon polynomial coefficients

Chapter 4

Theoretical Analysis

In this chapter a theoretical framework is presented with which to examine and understand radial ion transport in mirror machines. Radial transport is due to a variety of processes, acting simultaneously. The expected effects of these processes is calculated in this chapter.

The chapter is organized into four sections. In Section 4.1, the various transport mechanisms are described and their contribution to radial transport coefficients calculated for Constance parameters. The expected effects of low frequency RF power on transport are examined in Section 4.2. The basic equations which allow determination of transport coefficients from plasma profiles are given in Section 4.3. Section 4.4 contains a summary of the theoretical predictions to be compared with experimental data in Chapter 5.

4.1 Transport Mechanisms

Classical Diffusion

The most basic radial ion transport mechanism, present in any magnetic confinement geometry, is classical diffusion. The stochastizing agent which breaks the constancy of the parallel adiabatic invariant $\mathcal{J}$ is ion collisions with neutral atoms, electrons

$$\mu_{avg} = \frac{\sum \mu_i n_i}{n}$$

where $n = \sum n_i$. Figures 4-1(a),(b) and 4-2 show the radial profile of the computed D_{cl} for hydrogen, helium and argon plasmas. Because the charge state distribution in the plasma is difficult to measure, it is important to know how sensitively the calculation of D_{cl} depends on the exact distribution. This is especially true in argon plasmas, where the Time–of–Flight analyzer shows at least seven charge states. (See Figure 2-6.) Figure 4-2 shows D_{cl} in argon for two charge state distributions. Distribution 1, which is found using TOFA data and modelling, has Ar^{1+} through Ar^{7+} in the ratio (2234321). Distribution 2 has uses the unrealistic ratio (7654321). Note that the two D_{cl} curves in Figure 4-2 are nearly identical, showing that the calculation of D_{cl} is not sensitive to the exact charge state distribution. This result is expected, because the decrease of ρ_i in Equation 4.2 with charge state is partially cancelled by an increase in ν_{eff}.

Neoclassical Diffusion

In a nonaxisymmetric system, field line curvature leads to particle drifts off flux surfaces. If the equilibrium magnetic field is written as:

$$\mathbf{B} = \nabla\psi \times \nabla\theta \tag{4.4}$$

where ψ and θ are flux coordinates, then the field line curvature can be written:

$$\kappa = \mathcal{A}\nabla\psi + IO\nabla\theta \tag{4.5}$$

where $\mathcal{A}$ is the normal curvature perpendicular to the flux surface and IO is the geodesic curvature in the plane of the flux surface. The latter is nonzero only for nonaxisymmetric systems. The curvature drift off the flux surface is $V_{\kappa\perp}$:

$$V_{\kappa\perp} = \frac{v_\parallel^2}{\omega_c}\frac{IO\nabla\theta \times \mathbf{B}}{B} = \frac{v_\parallel^2 IO\nabla\psi}{\omega_c B} \tag{4.6}$$

Ion	H^+	He^+	He^+ (RF)	Ar^+	Ar^{++}
$T_i(eV.)$	5	8	28	50	50
ρ_i (cm.)	0.07	0.2	0.3	1.4	0.71
$\Delta r/r$	0.02	0.05	0.1	0.45	0.24
$d\phi/d\psi(\mathrm{V}/cm^2)$	0.2	0.36	0.36	0.15	0.15
$\Delta\theta$ (radians)	0.35	0.92	0.55	0.53	0.53
$\nu_{i,eff}$ (sec^{-1})	1.3×10^4	3.6×10^4	4.1×10^3	2.9×10^4	4.3×10^4

Table 4.1: (a)Ion parameters are shown for typical operating conditions in Constance. $\Delta r/r$ are radial excursions due to geodesic curvature. $\Delta\theta$ is due to the radial electric field $d\phi/d\psi$. Ion effective collision frequency is due to all other ion species. (b) The classical diffusion coefficient averaged over charge states on axis.

Plasma	Hydrogen	Helium	Argon
D_{cl} (cm^2/sec) (on axis)	200	570	3800

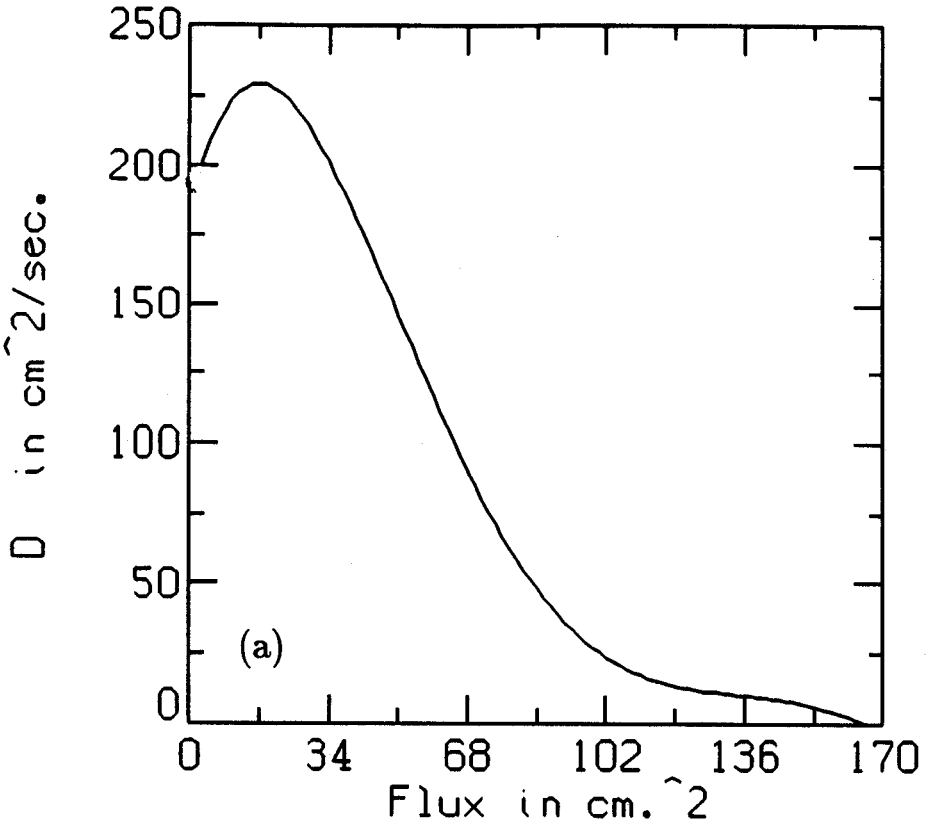

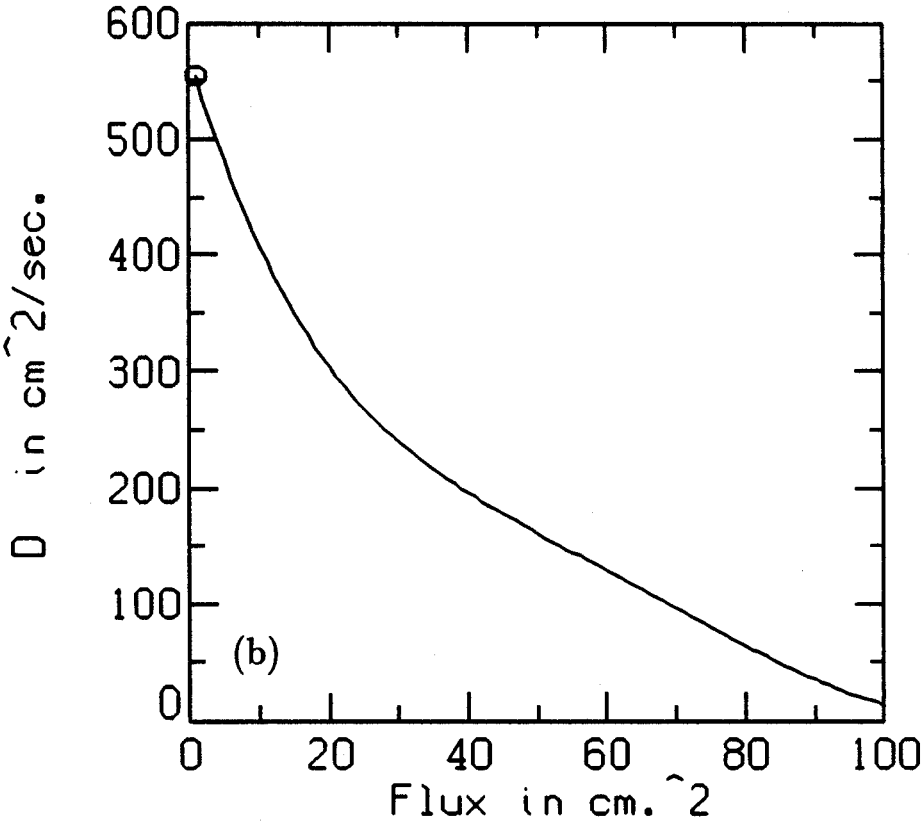

Figure 4-1: The classical diffusion coefficients for (a) hydrogen and (b) Helium plasmas in Constance are shown.

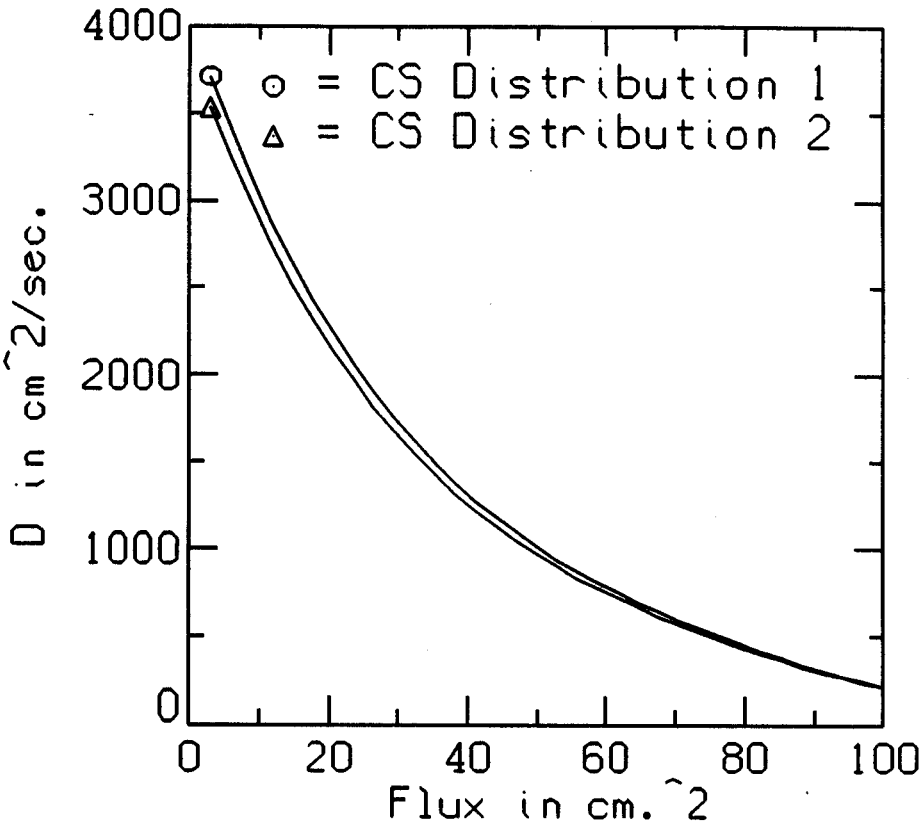

Figure 4-2: The classical diffusion coefficient in an argon plasma in Constance is shown. The calculation of D_{cl} is not sensitive to the exact charge state distribution.

Because the fanning flux surfaces have quadrupole symmetry and are rotated 90 degrees with respect to each other, IO is an odd function of Z. Thus the radial excursions which result from Equation 4.6 cancel when integrated over a bounce.

$$\oint \frac{dl}{|v_{\|}|} V_{\kappa\perp} = 0 \tag{4.7}$$

However, these radial excursions can lead to an increased transport rate. Neoclassical theory is the term for calculation of transport caused by particle orbit effects. The analogous effects in other confinement geometries are "banana" transport in tokamaks and "banana", "super–banana" and "ripple" transport in stellarators. The transport rates calculated by these theories are a result of particle–orbit effects combined with stochasticity generated from particle collisions.

For a nonaxisymmetric geometry, the flux function of Equation 4.4 is a function of both r and θ. Calculations of $\psi(r,\theta)$ for Constance have been done by Chen and by Goodman [X. Chen, 1988,Goodman, et al., 1986]. Chen calculates ψ from Constance $\mathcal{J}$ surfaces (where $\mathcal{J}$ is the parallel adiabatic invariant) by combining the orbits of deeply trapped electrons and the EFFI magnetic field line following code [Sackett, 1978] to obtain:

$$\psi(r,\theta) = r^2[1. - ((r/17)^2 - (r/18.4)^2 \cos 4\theta)] \tag{4.8}$$

Working from MHD theory using a long–thin expansion, Goodman found:

$$\psi(r,\theta) = r^2[1 - (r/18)^2 \cos 4\theta] \tag{4.9}$$

where r is in units of cm. at the midplane. The end loss, source and density profiles were analyzed using these complicated expressions for ψ as well as the simpler $\psi = r^2$. Because the complicated expressions deviate from circles only at large radius, and because experimental error causes a "smoothing" of the experimental quadrupole dependence, the results using Equations 4.8, 4.9 or $\psi = r^2$ were indistinguishable. Therefore all results in this thesis are analyzed using the simple expression $\psi = r^2$.

If the effective collision frequency of Equation 4.1 is sufficiently slow so that the parallel adiabatic invariant is a conserved quantity,

$$\mathcal{J}(\epsilon,\mu,\psi,\theta) = 2\int dl\sqrt{\epsilon - \mu B - q\phi} \tag{4.10}$$

then the guiding center drift equations [Northrop, 1963,Bernstein, 1971] lead to a drift off the flux surface of size:

$$\Delta r = \frac{c}{qBr}\frac{\partial \mathcal{J}}{\partial \theta} \tag{4.11}$$

We can calculate $\partial\mathcal{J}/\partial\theta$ if we use the long–thin analytic expansion for the Constance vacuum field [Goodman, et al., 1986].

$$\frac{\partial B}{\partial \theta} \simeq [B_0(1 + \frac{B_{T1}^2}{2B_0^2})] = \frac{1}{B_0}(r^2 A\frac{dB_0}{dz}\sin 2\theta) \tag{4.12}$$

where $B \equiv |\mathbf{B}|$ and

$$B_z = B_0 + B_{z2} + \ldots$$

$$\mathbf{B}_T = \mathbf{B}_{T1} + \mathbf{B}_{T3} + \ldots = \nabla_T^2 (\frac{-r^2}{4}\frac{dB_0}{dz} + A\frac{r^2}{2}\cos 2\theta) + \ldots$$

is the magnetic field expansion in the long thin parameter λ. Substituting Equation 4.12 into Equation 4.10 yields

$$\frac{\partial \mathcal{J}}{\partial \theta} = m\psi L_B^{-1} c_B \sin(2\theta) \int dl \frac{v_\perp^2}{v_\parallel} \tag{4.13}$$

where

$$c_B = 0.069 cm^{-1}$$

is the fanning factor and

$$L_B = (\frac{1}{B_0}\frac{dB_0}{dz})^{-1} \simeq 40cm$$

is the magnetic scale length.

If we define the function K:

$$K(v_{\parallel 0}^2/v_{\perp 0}^2) \equiv \int \frac{dl}{L_s v_{\perp 0}} \frac{v_\perp^2(l)}{v_\parallel(l)} \tag{4.14}$$

then

$K = 1$ for a square well model and

$K = \pi(1 + 0.5 v_{\parallel 0}^2/v_{\perp 0}^2)$ for a quadratic well with $R_m = 2$, and $v_{\parallel 0}$, $v_{\perp 0}$ are midplane velocities. Substituting Equations 4.14 and 4.13 into Equation 4.11 gives:

$$\Delta r = \rho_i r c_B (L_s/L_B) \sin(2\theta) K(V_{\parallel 0}^2/v_{\perp 0}^2) \tag{4.15}$$

where $L_s \simeq 40$ cm. is the full bounce length. The radial excursions $\Delta r/r$ for several ions under Constance parameters is shown in Table 4.1.

This calculation gives results similar in form to those obtained for TMX by Cohen [Cohen, et al., 1979]. The function K of Equation 4.14 differs from Cohen's expression because nonzero geodesic curvature was found only in the TMX MHD anchors, so ions trapped in the central cell were for the most part confined to an axisymmetric system. All ions in Constance, even deeply trapped ions, sample a nonaxisymmetric magnetic field.

Because Δr calculated in Equation 4.15 is approximately the size of the ion gyroradius, the new step size Δr and the effective collision frequency produce a diffusion coefficient which is close in magnitude to the classical coefficient.

Under some cases, the effective collision frequency can be enhanced by a resonance phenomenon, leading to a much larger diffusion coefficient. If during a bounce an ion also drifts azimuthally in θ, the bounce average cancellation of radial excursion expressed by Equation 4.7 may not occur. The resonance condition is:

$$\Delta\theta = \frac{(2n+1)}{2}\pi \tag{4.16}$$

Azimuthal rotation is caused by $E \times B$ and ∇B drifts, with the former dominating for ions in Constance. Particles exactly in resonance leave the machine radially in a few bounces, and particles near resonance execute radial excursions larger than Δr of Equation 4.15. The parameter which determines whether resonant neoclassical transport is an important effect is the angular change per bounce:

$$\Delta\theta(\psi, \epsilon, \mu) = \frac{2L_s c}{v_{\|} B}\frac{d\phi}{d\psi} \tag{4.17}$$

If $\Delta\theta \ll 1$, then only nonresonant neoclassical transport contributes to the diffusion coefficient. If $\Delta\theta \geq 1$, then resonant effects are important. The stochastic regime is defined as $\Delta\theta \gg 1$.

Typical values of $\Delta\theta$ for ions in Constance range from 0.3–1, as shown in Table 4.1. Values of $d\phi/d\psi$ are also shown in the table.

Analytical approximations to the resonant neoclassical transport coefficients in the plateau regime (the regime applicable to the high collisionality of Constance) have been calculated by Cohen [Cohen, et al., 1979]. Using his method and Δr from Equation 4.15 we obtain a diffusion coefficient which is the sum over resonances.

$$D_0 = \sum_{n=0}^{\infty} D_{0n} \tag{4.18}$$

$$D_{0n} = A_0\left(\frac{M}{2\pi T_i}\right)^{3/2}\frac{\exp(-W_{0n}/T_i)}{(n+1/2)^3}\left(\frac{T_i}{B}\right)^2$$

$$W_{0n} = \frac{8ML^2c^2(d\phi/d\psi)^2}{\pi^2(2n+1)^2B^2}$$

$$A_0 = \frac{8}{\pi}\frac{LC_B^2c^2K^2(d\phi/d\psi)^2}{M^2\Omega_i^2}\psi$$

where

n = resonance number as defined in Equation 4.16,

W_{0n} = energy of nth resonance ion,

L = ion bounce length, and

Ω_i is the ion cyclotron frequency.

For Constance parameters, $W_{0n} \leq$ 1eV., so only the coldest ions in the distribution function are resonant. This is also why $\Delta\theta < 1$ in Table 4.1(a), and causes the $n = 0$ term in Equation 4.18 to be the only important term.

An upper limit to the diffusion coefficient of Equation 4.18 as calculated by Ryutov [Ryutov and Stupakov, 1978] is:

$$D_{nc} = (\Delta r)^2/\tau_b \tag{4.19}$$

where Δr is from Equation 4.15 and τ_b is the ion bounce time. This upper limit gives approximately the correct D_{nc} when the bulk ions satisfy the resonance condition of Equation 4.16 or equivalently $W_{0n} \simeq T_i$. Figures 4-3(a) and (b) and 4-4 are plots of the diffusion coefficient of Equation 4.19 representing the upper limit to the neoclassical diffusion coefficient for hydrogen, helium and argon plasma in Constance.

Another effect, also falling under the heading of neoclassical transport, is due to the departure of the equilibrium from omnigenity. If the drift surfaces of deeply trapped and shallowly trapped particles do not coincide, then pitch angle scattering in velocity space will also lead to diffusion in real space. The omnigenous nature of the magnetic drifts in Constance was verified using the GCDRIFT code [Devoto, 1986]. The review article by Post [Post, 1987] described the same result for the Baseball II experiment, whose coil is nearly the same as the Constance coil. As long as we can describe the potential profile as $\phi = \phi(\psi)$ then the adiabatic invariant $\mathcal{J}(\epsilon, \mu, \psi, \theta)$ will be independent of θ and the ion drifts will remain omnigenous.

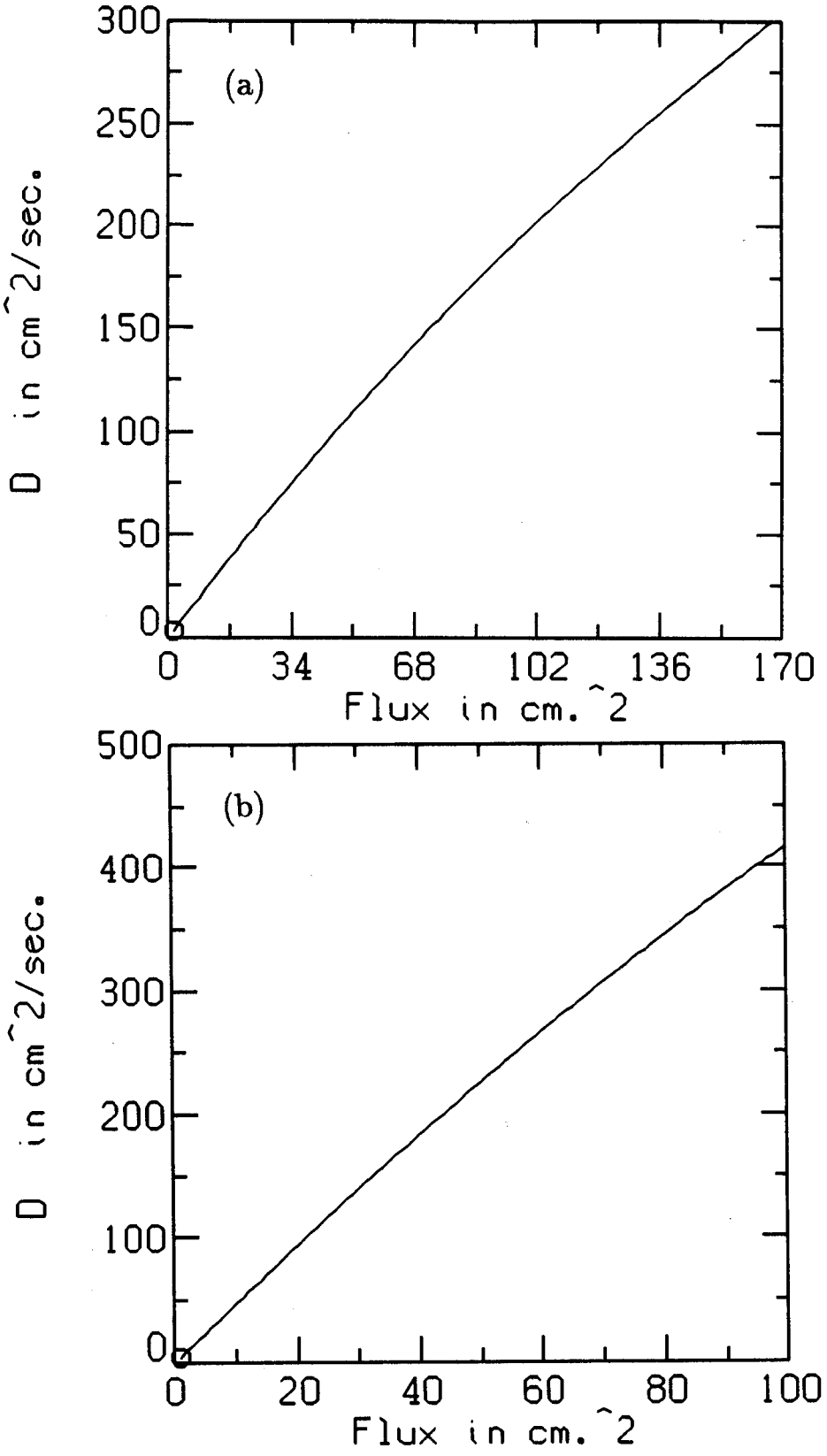

Figure 4-3: The neoclassical diffusion coefficients in (a) hydrogen and (b) Helium shown here represent upper limits, given by Equation 4.19

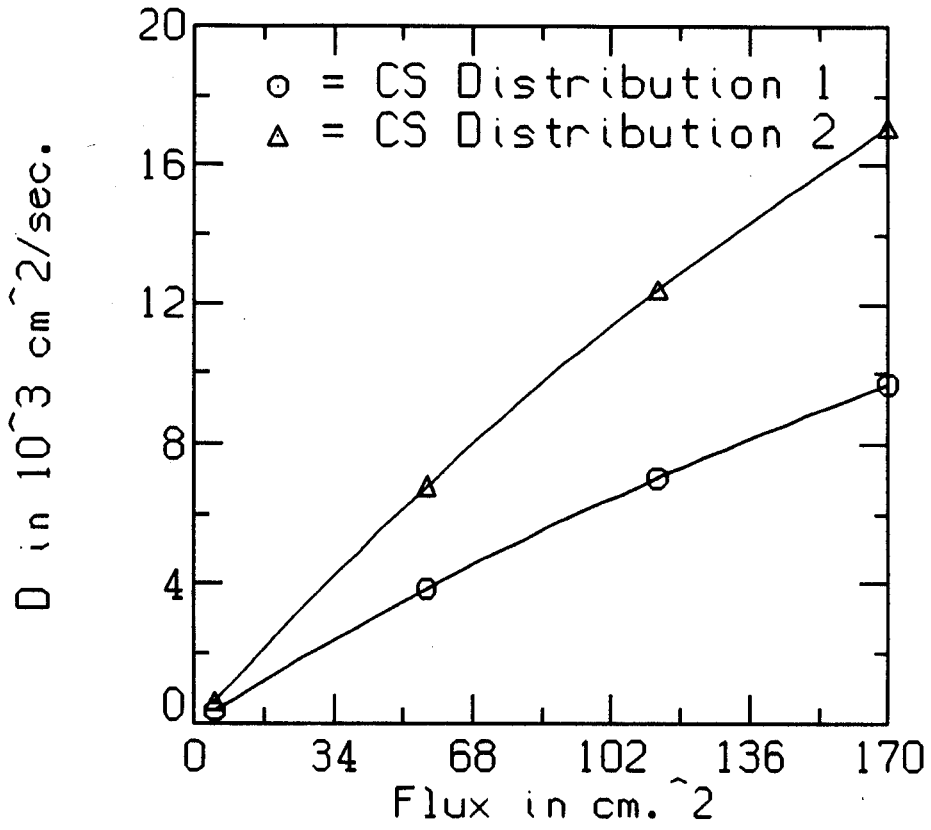

Figure 4-4: The upper limit to the Argon D_{nc} is shown. Charge state distribution 1 is consistent with experimental data. The calculation of D_{nc} is more sensitive to charge state distribution than D_{cl}. (Compare with Figure 4-2.)

4.2 RF Effects

Direct Effects

Low frequency RF waves directly affect ions by causing changes in the magnetic moment μ, where $\mu = \frac{1}{2}mv_{\perp}^2/B$ is the adiabatic invariant associated with the cyclotron motion. If the applied frequency is resonant with the ion cyclotron frequency, ions receive kicks in μ and diffuse in velocity space. If no resonance zone exists in the machine, the effect is much smaller because the electric field seen by the particle averages to zero on a much shorter time scale.

Various authors have calculated the effect of changes in μ on radial diffusion in tokamaks [Whang and Morales, 1983,Riyopoulos, et al., 1986,Chen, 1988]. The start-

ing point for the calculations is often a single particle model, where the change in μ passing through the resonance zone is:

$$\frac{d}{dt}\mu^{1/2} = \frac{qE_+}{\sqrt{2mB}}\cos(k_\perp x_\perp)\cos\theta' \tag{4.20}$$

E_+ is the RF electric field resonant with ions and $\theta' = \theta - (k_\parallel x_\parallel - \omega t)$ is the Doppler shifted wave phase.

Equation 4.20 can be integrated through the resonance to find the nonadiabatic change in μ. Since the parallel adiabatic invariant depends on μ, (in the case of tokamaks the invariant is $\mathbf{P}_\phi$, the canonical toroidal angular momentum, for mirrors it is $\mathcal{J}$), the jumps in μ also lead to motion of the guiding center trajectory. The constancy of $\mathcal{J}$ leads us to expect radial steps in ψ:

$$\delta\psi \simeq -\frac{(\partial\mathcal{J}/\partial\mu)|_{\psi,\theta,\epsilon}}{(\partial\mathcal{J}/\partial\psi)|_{\mu,\theta,\epsilon}}\delta\mu \tag{4.21}$$

All theories of RF induced diffusion calculate a diffusion coefficient for μ proportional to $|E_{RF}|^2$, so we expect

$$D^{RF} = C\frac{(\partial\mathcal{J}/\partial\mu)}{(\partial\mathcal{J}/\partial\psi)}|E_{RF}|^2 \tag{4.22}$$

where C is a constant which contains details of the RF–particle interaction including the FLR Bessel functions and the interaction time in resonance. The three references [Whang and Morales, 1983,Riyopoulos, et al., 1986,Chen, 1988] all contain calculations of this coefficient. The μ and ψ derivatives of $\mathcal{J}$ in Equation 4.22 can be found in a manner similar to the calculation of the θ derivative of $\mathcal{J}$ in Equations 4.11 to 4.13.

Indirect Effects

As shown in Figure 3-17 and seen in the TARA and Phaedrus mirrors [Smith, et al., 1986, Hershkowitz, et al., 1985], the electron confining potential ϕ_0 increases substantially during application of low frequency RF power. If the radial electric field also changes

in magnitude or direction during RF, then the RF power will indirectly affect radial ion transport. The radial particle flux due to diffusion and mobility is:

$$\Gamma = 2\sqrt{\psi}(D\frac{dn}{d\psi} + q\mu n\frac{d\phi}{d\psi}) \tag{4.23}$$

If the RF electric field increases $d\phi/d\psi$ (for example by interacting directly with electrons) without increasing D or μ, then the RF power has indirectly increased the transport rate. This is in contrast with the direct effects described in the previous section, where the RF waves directly interact with ions.

As will be shown in Chapter 5, the potential is consistent with a direct interaction between the RF electric field and the electrons, in agreement with a model proposed by Parks [Parks, 1987].

Parks predicted that the RF power should modify the parallel electron distribution function in a complex way which depends both on normalized RF power $\eta = E_{RF}^2/E_0^2$ and on normalized potential $\Psi = \phi_0/T_{ec}$. Here E_{RF} is the parallel RF electric field, which is nonzero for electrons at finite temperature, and E_0 is a normalization constant which can be calculated from quasi–linear theory.

If a quasilinear theory is valid for the RF–electron interaction, and the perturbation in electron motion by the wave is small, then the wave causes diffusion in velocity space, which can be represented in the large velocity limit as:

$$D(v_\parallel) = \eta v_t/v_\parallel \tag{4.24}$$

where v_t is the electron thermal velocity.

This term can be added to the Fokker–Planck equation and solved in a square well geometry in a manner similar to the solution by Pastukhov [Pastukhov, 1974] for the zero RF power case. From the resulting modified electron distribution function, Parks calculates the normalized potential $\Psi(\eta)$ that will produce a given electron end loss rate ν'. He finds

$$\nu' = \frac{(2 + Z_{avg}^{in})(1 + 2\eta)(1 + 2\eta\Psi)^{1-1/(2\eta)}\nu_e}{2\mathcal{N}(\Psi,\eta)(\Psi - 1)(R + 2\eta\Psi)} \tag{4.25}$$

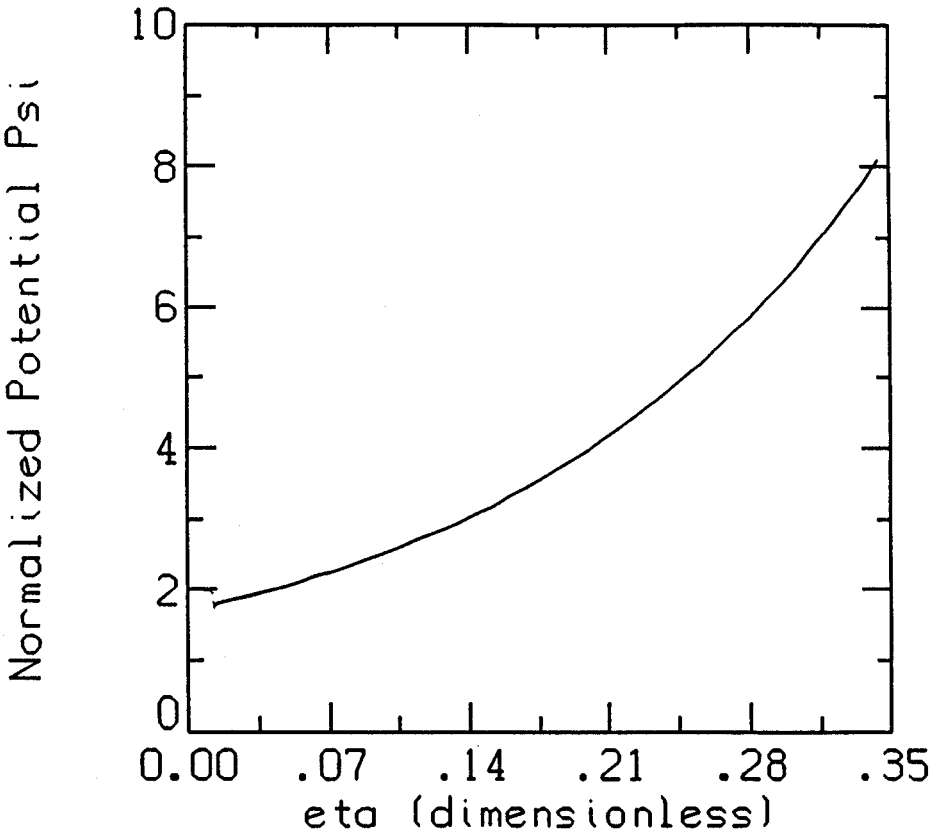

Figure 4-5: Normalized potential $\Psi = \phi_0/T_{ec}$ based on Parks theory is shown.

where for our parameters, $\mathcal{N} \simeq 1.25$, ($\mathcal{N}$ is an integral function defined in [Parks, 1987] which is quite insensitive to the value of its arguments.)

R is the magnetic mirror ratio, and

ν_e is the electron collision frequency.

Figure 4-5 is a plot of the predicted $\Psi(\eta)$ derived from Equation 4.25. Figure 4-5 is based on the assumption that during application of RF power, the electron end loss remains equal to its $\eta = 0$ value to balance the ion end loss. The $\eta = 0$ value is:

$$\nu_{\eta=0} = \frac{(2 + Z^{in}_{avg})\nu_e \exp(-\Psi)}{\sqrt{2\pi}R(\Psi - 1)} \tag{4.26}$$

Another way to state this assumption is to rewrite Equation 4.25 as

$$\nu' = (2 + Z^{in}_{avg})G(\eta, \Psi)\nu_e \tag{4.27}$$

The curve of Figure 4-5 can then be written:

$$G(\eta, \Psi) = G_0 \tag{4.28}$$

with G_0 a constant.

To lowest order, the theory assumes that the average charge state, loss rate (ν') and electron collisionality are independent of RF power. A more complete model includes RF modification of these parameters.

4.3 Basic Equations

The continuity equation with a volume source term S' is:

$$\partial n_i/\partial t + \nabla \cdot \mathbf{\Gamma} = S' \tag{4.29}$$

where $S' = n_e n_0 < \sigma v >_{exc}$ and Γ is the ion particle flux.

If we write the ion flux in terms of its components parallel and perpendicular to the magnetic field, Equation 4.29 becomes:

$$\nabla \cdot \Gamma_{\|}\mathbf{b} + \nabla_{\perp} \cdot \mathbf{\Gamma}_{\perp} = S' \tag{4.30}$$

We can write the first term in Equation 4.30 as:

$$\nabla \cdot (\mathbf{B}\frac{\Gamma_{\|}}{B}) = (\mathbf{B} \cdot \nabla)(\frac{\Gamma_{\|}}{B}) + \frac{\Gamma_{\|}}{B}(\nabla \cdot \mathbf{B}) \tag{4.31}$$

where the last term vanishes by Maxwell's equation. Integrating with respect to $\int dl/B$:

$$\int_{-L(\psi)}^{+L(\psi)} \frac{dl}{B}(\mathbf{B} \cdot \nabla)(\frac{\Gamma_{\|}}{B}) + \int_{-L(\psi)}^{+L(\psi)} \frac{dl}{B}(\nabla_{\perp} \cdot \mathbf{\Gamma}_{\perp}) = \int_{-L(\psi)}^{+L(\psi)} \frac{dl}{B} S' \tag{4.32}$$

The first term of Equation 4.32 is:

$$\int_{-L}^{+L} dl(\mathbf{b} \cdot \nabla)(\frac{\Gamma_{\|}}{B}) = \int_{-L}^{+L} dl\, \frac{\partial}{\partial l}(\frac{\Gamma_{\|}}{B}) = 2\frac{\Gamma_{\|}(L)}{B(L)} \tag{4.33}$$

If we define the integrated source and loss functions S and J:

$$S = Z_{avg}^{end} B_L \int_{-L(\psi)}^{+L(\psi)} \frac{dl}{B} S' \tag{4.34}$$

$$J = 2Z_{avg}^{end}\Gamma_{\parallel}(L) = Z_{avg}^{end}B_L\int_{-L(\psi)}^{+L(\psi)}\frac{dl}{B}(\nabla\cdot\Gamma_{\parallel}\mathbf{b})$$

then Equation 4.30 becomes:

$$(Z_{avg}^{end})^{-1}(S-J) = B_L\int_{-L(\psi)}^{+L(\psi)}(\nabla_{\perp}\cdot\mathbf{\Gamma}_{\perp}) \tag{4.35}$$

where B_L is the magnetic field at which the density drops to zero.

Integrating Equation 4.35 over flux:

$$(Z_{avg}^{end})^{-1}\int_0^{\psi}(S-J)\,d\psi' = B_L\int_0^{\psi}d\psi'\int_{-L(\psi)}^{+L(\psi)}\frac{dl}{B}(\nabla_{\perp}\cdot\mathbf{\Gamma}_{\perp}) \tag{4.36}$$

The right hand side (RHS) of Equation 4.36 can be written:

$$= \int_{-L(\psi)}^{+L(\psi)}dl\int_0^{\psi}d\psi'(\nabla_{\perp}\cdot\mathbf{\Gamma}_{\perp}) + R_1 + R_2 \tag{4.37}$$

where the first remainder term R_1 occurs during the interchange of order of integration and the second remainder term accounts for the difference between dl/B integration and dl integration. R_1 is nonzero because the limits of integration $\pm L$ are functions of ψ. Both remainder terms are small, as is shown later in this section.

The volume element is $dV = \pi\,d\psi\,dl$, so Equation 4.37 is

$$= \frac{1}{\pi}\int dV\,(\nabla_{\perp}\cdot\mathbf{\Gamma}_{\perp}) + R_1 + R_2 \tag{4.38}$$

$$= \frac{1}{\pi}\int \mathbf{\Gamma}_{\perp}\cdot\mathbf{dA} + R_1 + R_2$$

where the divergence theorem has been used.

If we assume diffusive radial transport:

$$\mathbf{\Gamma}_{\perp} = -\mathbf{D}\cdot\nabla_{\perp}n_i - n_i\mu\cdot\nabla\phi \tag{4.39}$$

where $n_i = n_e/Z_{avg}^{in} \equiv n/Z_{avg}^{in}$.

Equation 4.30 can now be written:

$$(Z_{avg}^{end})^{-1}\int_0^{\psi}(S-J)\,d\psi' = \frac{2\sqrt{\psi}}{\pi Z_{avg}^{in}}\int_0^{2\pi}\sqrt{\psi}\,d\theta\int_{-L}^{+L}dl\,[-D(\psi)\frac{\partial n}{\partial\psi} - \mu(\psi)n\frac{\partial\phi}{\partial\psi}] + R_1 + R_2 \tag{4.40}$$

$$= \frac{-4\psi}{Z_{avg}^{in}} \int dl \, [D\frac{\partial n(\psi,l)}{\partial \psi} + \mu n(\psi,l)\frac{\partial \phi(\psi,l)}{\partial \psi}] + R_1 + R_2$$

If we define line average quantities,

$$\partial \bar{n}/\partial \psi \equiv \int_{-L}^{+L} dl \, \frac{\partial n(\psi,l)}{\partial \psi} \tag{4.41}$$

$$\overline{n \, \partial \phi/\partial \psi} \equiv \int_{-L}^{+L} dl \, n\frac{\partial \phi}{\partial \psi}$$

then our basic equation can be written:

$$\frac{Z_{avg}^{in}}{Z_{avg}^{end}} \int_0^{\psi} (S - J) \, d\psi' = -4\psi[D\partial \bar{n}/\partial \psi + \mu \overline{n \, \partial \phi/\partial \psi}] + R_1 + R_2 \tag{4.42}$$

We show below that for Constance $\overline{n \, d\phi/d\phi} \simeq \bar{n}\overline{d\phi/d\psi}$, and $R_1, R_2 \ll$ the main term. Using the Einstein relation between D and μ (valid as long as transport is diffusive in nature):

$$\mu(\psi) = Z_{avg}^{in} D(\psi)/T_i \tag{4.43}$$

we can solve Equation 4.42 for D:

$$D(\psi) = \frac{Z_{avg}^{in} 2 \int_0^{\psi} (S - J) \, d\psi'}{64 Z_{avg}^{end} a\psi(d\bar{n}/d\psi + \frac{\bar{n} Z_{avg}^{in}}{T_i} d\phi/d\psi)} \tag{4.44}$$

Here D is in units of $10^4 cm^2/sec$, T_i is in eV., ψ in cm^2, a in units of $10^{13} cm^{-2}$ as given in Table 3.2, $\bar{n}$ is dimensionless (units absorbed into a) and Z_{avg}^{in} and Z_{avg}^{end} are the average charge states in the plasma and in the end loss:

$$Z_{avg} = \frac{\sum n_i z_i}{\sum n_i} \tag{4.45}$$

The source S in Equation 4.44 is *one half* the total ionization source function in $mA./cm^2$ to allow easy comparison with the end loss. Polynomial coefficients for S, J and $\bar{n}$ are given in Tables 3.3, 3.4 and 3.5.

The assumption that:

$$\bar{n}\overline{\partial \phi/\partial \psi} \simeq \overline{n \partial \psi/\partial \psi}$$

is justified as long as the potential in the plasma region is smooth and does not drop precipitously. We have measured $\phi_1 \ll \phi_0$ so the assumption is justified.

The ratio of the first remainder term to the main term in Equation 4.42 is:

$$R_1 / \int dl\,[Ddn/d\psi + ...] = \frac{\psi}{L}\frac{\partial L}{\partial \psi}\frac{[\partial n/\partial\psi + \bar{n}Z/T_i\partial\phi/\partial\psi]|_{\psi=\bar{\psi},l=1/2[L(\psi)+L(0)]}}{[\partial n/\partial\psi + \bar{n}Z/T_i\partial\phi/\partial\psi]|_{avg}} \quad (4.46)$$

This ratio $\ll 1$ since $n(\frac{L(\psi)+L(0)}{2}) \ll n_{avg}$.

The ratio of the second remainder term to the main term in Equation 4.42 is:

$$R_2 / \int dl\,[Ddn/d\psi + ...] \simeq \frac{1}{5}\frac{L^2}{L_B^2} \leq 5\% \ll 1 \quad (4.47)$$

where the numerical coefficient of 1/5 was found for a quadratic magnetic field and density dependences:

$$B = B_0(1 + Z^2/L_B^2)$$

$$n = n_0(1 - Z^2/L^2)$$

and the actual coefficient will depend on the exact profile.

The functions on the right hand side of Equation 4.44 are all experimentally measurable quantities described in Chapter 3. The diffusion coefficient given by Equation 4.44 is an average ion particle diffusion coefficient which includes all charge states. Measuring the diffusion coefficient separately for each charge state is difficult because it requires the full radial density profile for each ion species.

The importance of radial transport in affecting confinement time can be quantified by comparing the parallel and perpendicular ion lifetimes. These times are defined as:

$$\tau_{\|}(\psi) = \frac{\int_0^\psi \bar{n}\, d\psi'}{2\int_0^\psi J\, d\psi'} \quad (4.48)$$

$$\tau_{\perp}(\psi) = \frac{\int_0^\psi \bar{n}\, d\psi'}{2\int_0^\psi (S - J)\, d\psi'}$$

where $\int_0^\psi \bar{n}\pi\, d\psi'$ is the total number of particles inside a flux surface labelled by ψ. These definitions are consistent with the equilibrium requirement:

$$\tau_s^{-1} = \tau_{\|}^{-1} + \tau_{\perp}^{-1} \quad (4.49)$$

where τ_s is the ionization source time:

$$\tau_s = \frac{\int_0^\psi \bar{n}\, d\psi'}{2\int_0^\psi S\, d\psi'} \quad (4.50)$$

If parallel and perpendicular losses exceed the rate at which particles are ionized,

$$\tau_i^{-1} = \tau_{i\|}^{-1} + \tau_{i\perp}^{-1} > \tau_s^{-1}$$

then equilibrium is lost. We believe this effect is seen during application of RF at high power, as is discussed in Chapter 5.

4.4 Theoretical Predictions

The various radial transport theories presented in this chapter can be used to make predictions about the expected value for transport rates and coefficients on Constance.

Classical transport is an inescapable background process in all magnetic confinement systems, which puts a lower limit on the diffusion coefficient. Neoclassical transport is calculated using magnetic field and plasma models, resulting in a coefficient whose accuracy is difficult to determine. Equation 4.19 provides an upper limit to the neoclassical diffusion coefficient. Figures 4-6 and 4-7(a) and (b) are plots of D_{max} in hydrogen, helium and argon plasmas, where D_{max} is:

$$D_{max}(\psi) \equiv D_{cl}(\psi) + D_{nc}(\psi) \tag{4.51}$$

D_{cl} in is taken from Equation 4.2 and D_{nc} from 4.19. We expect that if the experimentally determined diffusion coefficient is larger than D_{max}, other processes beside classical and neoclassical transport are responsible.

In addition to examining the scaling of the diffusion coefficients with ψ, we can also examine their scalings with ion mass number. These scalings are:

$$D_{cl} \sim m T_i^{-1/2} \sum_{j \neq i} n_j Z_j^2 \tag{4.52}$$

$$D_{nc} \sim m^{1/2} Z^{-2} T_i^{3/2} \psi$$

For our parameters the size of D_{cl} and D_{nc} are similar. Since from Figure 3-26, T_i increases linearly with mass number, and $Z_{avg} \simeq m^{1/3}$, both the classical and

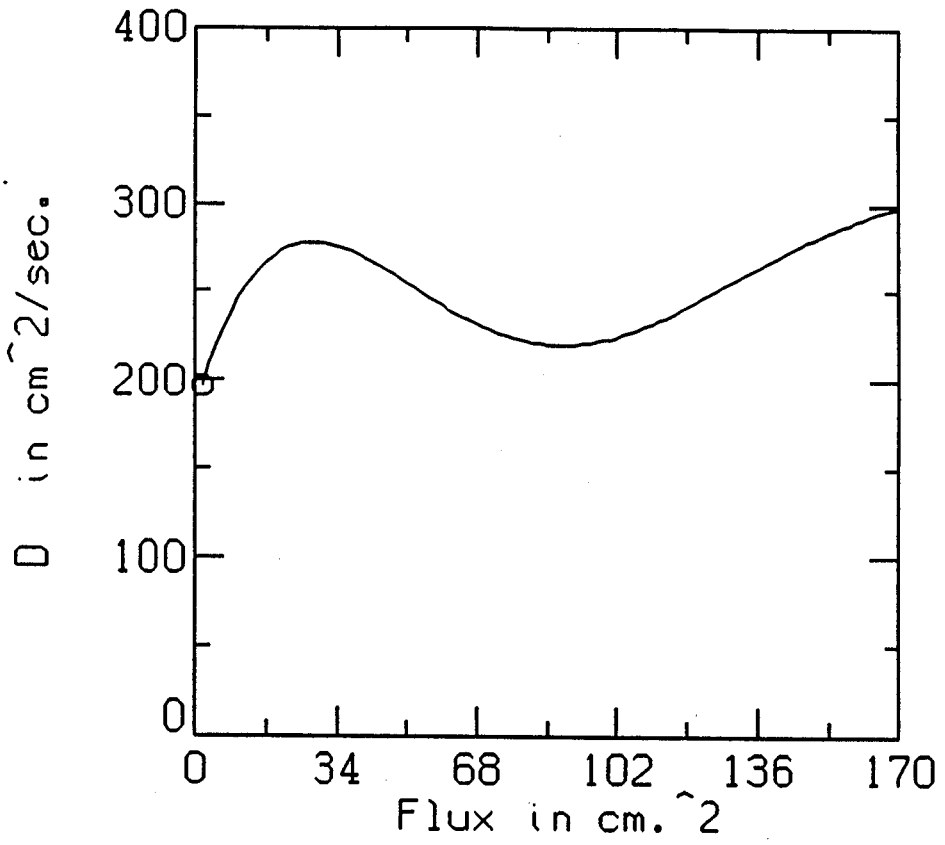

Figure 4-6: The sum of the classical and neoclassical diffusion coefficient D_{max} is shown for a hydrogen plasma in Constance.

neoclassical diffusion coefficients should scale approximately linearly with ion mass. Table 4.1(b), which shows D_{cl} averaged over charge state, also shows this dependence.

The theory outlined in this chapter allows several other predictions. From Section 4.2 we expect the direct effect of low frequency RF waves on radial ion transport to be largest on ions whose cyclotron frequency is resonant with the applied frequency. Indirect effects, such as modification of the radial transport rate via the potential gradient, should afftect the transport rate of both resonant and nonresonant ions. Theory presented in Section 4.2 also predicts the scaling of normalized electron confining potential $\Psi = \phi_0/T_{ec}$ with RF power as shown in Figure 4-5. Equation 4.49 predicts a loss of equilibrium if the perpendicular transport rate exceeds a threshhold value, which occurs when the ionization source cannot keep up with the ion loss rate.

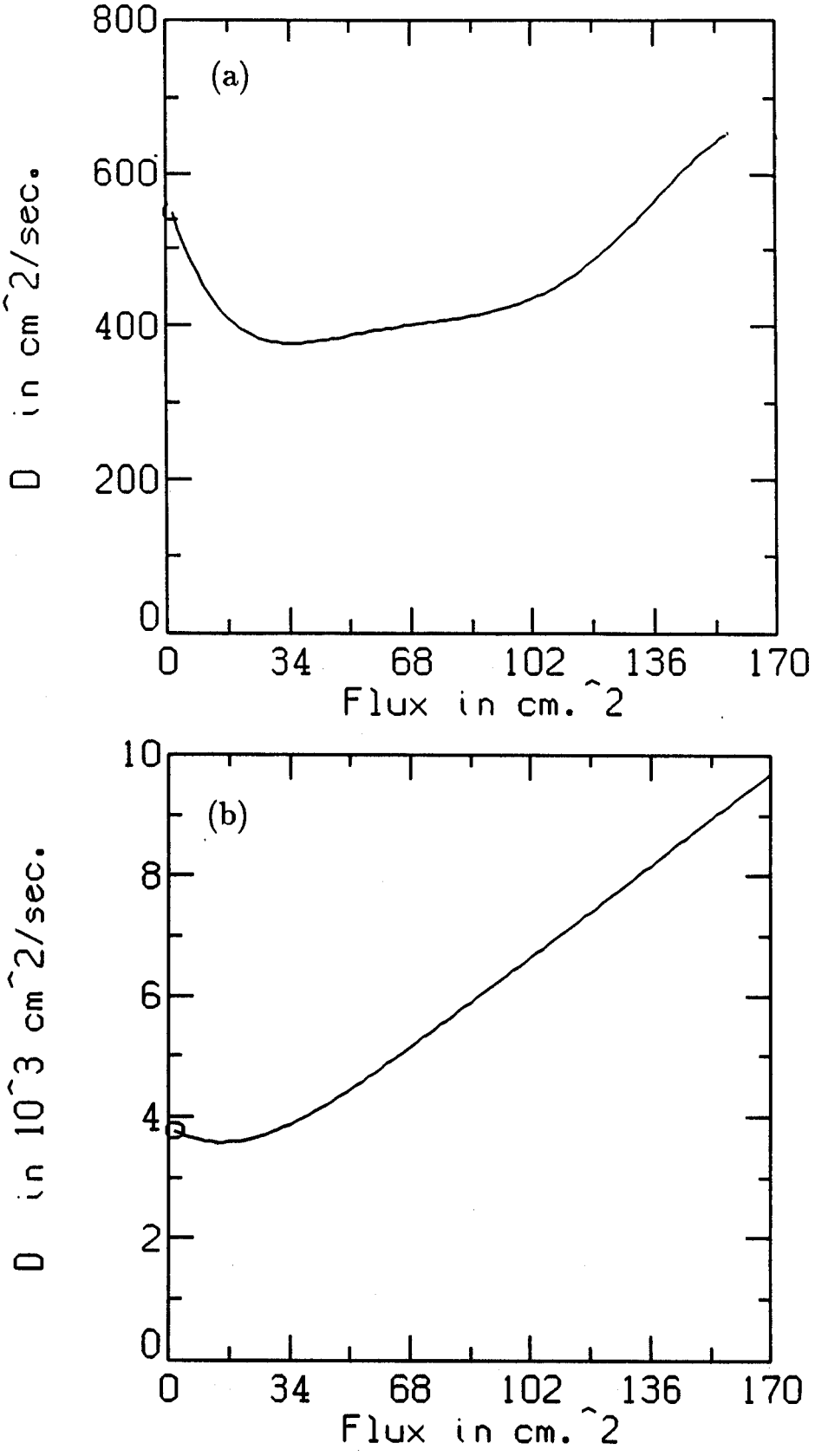

Figure 4-7: D_{max} for (a) helium plasma and (b) argon plasmas are shown.

Chapter 5

Experimental Results

The diagnostics introduced in Chapter 2 and the experimental methods of Chapter 3 produced the experimental results summarized in this chapter. These results are also compared with the predictions of Chapter 4 to see how well experiment agrees with the theory outlined in that chapter.

5.1 Ion Lifetimes

As mentioned in Chapter 1, the presence of hot magnetically confined electrons dramatically increases the ion parallel confinement time in Constance over their collisional value. By measuring the plasma density, source function and ion end loss profiles as described in Chapter 3, we find the lifetimes $\tau_\perp$ and $\tau_\parallel$ for a hydrogen plasma under standard conditions shown in Figure 5-1(a). As shown in Table 4.1, the ν_{eff} for hydrogen corresponds to a scattering time of less than 0.1 ms. The parallel lifetimes of several ms shown in Figure 5-1(a) represent more than an order–of–magnitude increase in parallel lifetime compared to ν_{eff}^{-1}. Experimental work [Petty, 1988] measuring the lifetime of multiple charge states shows that the parallel lifetime in Constance is well described by the Pastukhov formula for ions electrostatically confined by the potential dip ϕ_1 [Pastukhov, 1974]. These long $\tau_\parallel$'s allow the ions to remain in the mirror long enough to make radial transport an important loss mechanism.

Although we measure the source function absolutely, using a calibrated CCD camera, as described in Chapter 3 and Appendix B, when computing $\tau_{\|}$ as accurately as possible we normalize the source function by a constant of order unity to force:

$$\int_0^{\psi_{max}} (S - J)\, d\psi' = 0 \tag{5.1}$$

Equation 5.1 expresses the conservation of ions in Constance. Because of the high T_{ec} and low density, particles once ionized do not recombine inside the plasma, but are lost as end loss at some value of flux $\psi \leq \psi_{max}$. (For 100 eV. electrons and $5 \times 10^{11} cm^{-3}$ density, the recombination time is more than 100 times longer than our particle confinement time.) The source normalization and particle balance are described in detail in Appendix B.

The large perpendicular confinement time at the plasma edge in Figure 5-1(a) is a consequence of Equation 5.1 and the definition of $\tau_{\perp}$ (Equation 4.48). The most important feature of Figure 5-1(a) is that the confinement times $\tau_{\perp}$ and $\tau_{\|}$ are within a factor of two of each other over almost the entire plasma. This quantitatively confirms the qualitative estimates of the previous section.

The same procedure in helium and argon plasmas produced Figures 5-1(b) and 5-2. Note that near the center of an argon plasma, the perpendicular confinement time is actually shorter than the parallel confinement time. The increase in perpendicular transport with ion mass shown in Figure 1-2 makes it plausible that the ratio $\tau_{\perp}/\tau_{\|}$ should be smaller in an argon plasma than in hydrogen or helium.

If we combine the density, end loss and source profiles used to make Figures 5-1 and 5-2 with the derivatives of the density and potential profiles, we can solve for the perpendicular diffusion coefficient using Equation 4.44. The electron confining potential ϕ_0 for helium was shown in Figure 3-16. The ϕ_0 profiles for hydrogen and argon plasmas are shown in Figures 5-3 and 5-4. The data before application of low frequency RF power is shown as circles, and only has a small amount of shot–to–shot scatter.

Before computing diffusion coefficients it is reasonable to ask whether the radial transport measured in this thesis is diffusive in nature. Ideally we would like to vary

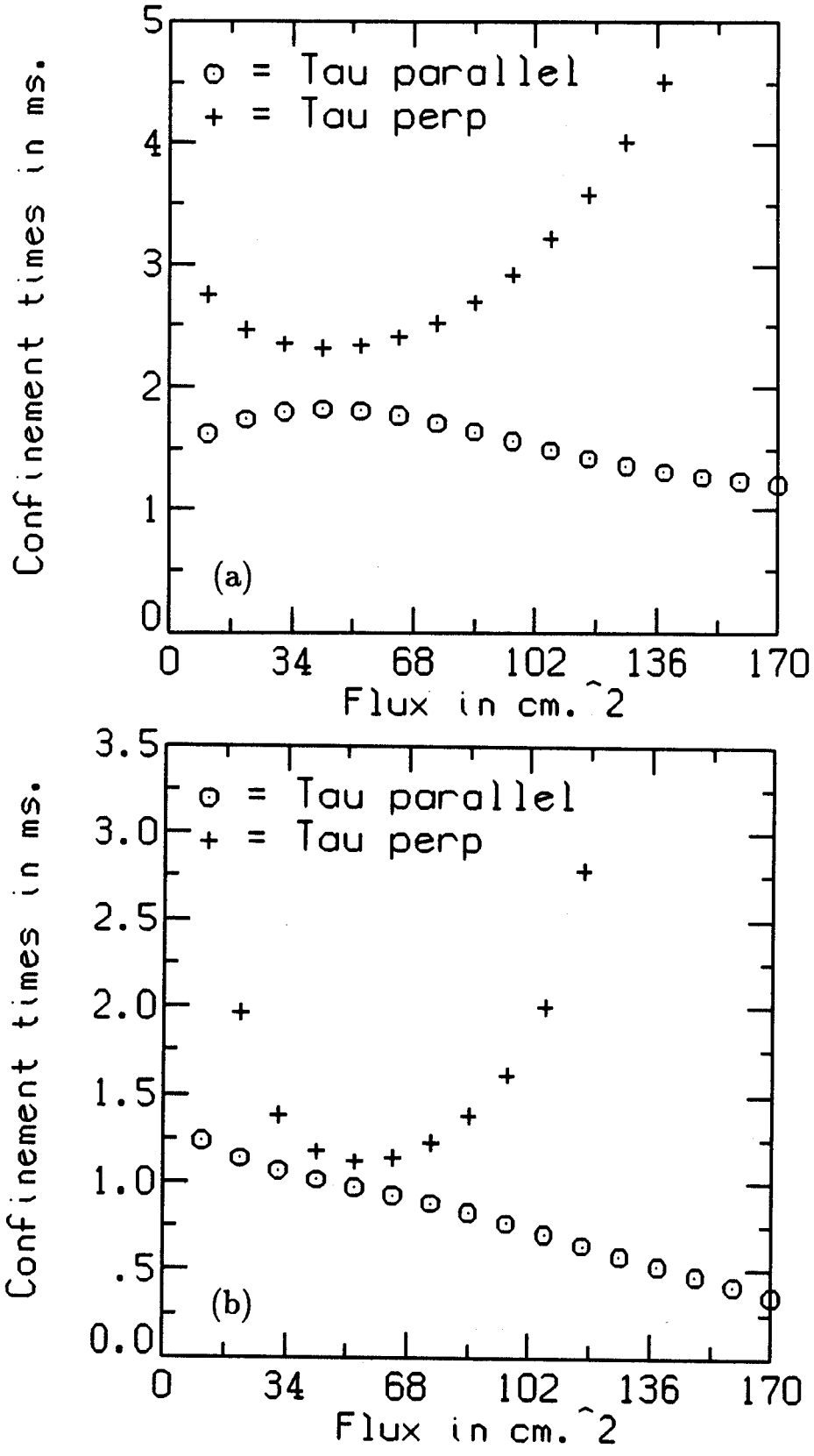

Figure 5-1: Confinement times in (a) hydrogen and (b) helium plasmas are shown.

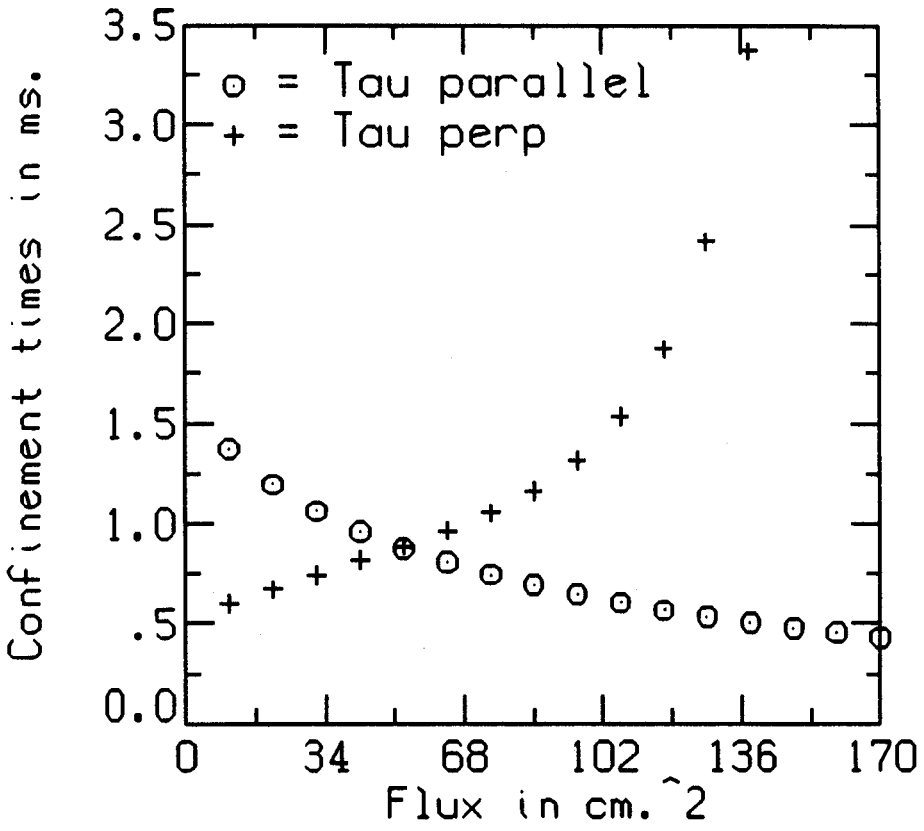

Figure 5-2: Confinement times in an argon plasma is shown.

$dn/d\psi$ and $d\phi/d\psi$ leaving other parameters fixed and see if the radial fluxes follow a Fick's law. (Equation 4.23). We would like to measure this locally using probes or a limiter, or globally (flux average) by measuring source and end loss profiles. The local measurements are desirable because they allow comparison of regions with various values of $d\phi/d\psi$ and $dn/d\psi$. Experimentally they are difficult because they perturb the plasma and it is difficult to collect only the radially directed current. The global measurements require changing the overall $dn/d\psi$ and $d\phi/d\psi$. Application of low frequency RF power increases ϕ by about a factor of two. (See Figures 3-16, 5-3 and 5-4.) RF power also increases $d\phi/d\psi$ by up to a factor of five and T_i by a factor of four, yet we show in this chapter that the diffusion coefficients during RF increase by no more than a factor of two over their pre–RF values, and in many cases stay approximately the same. If the transport were convective, driven by potential

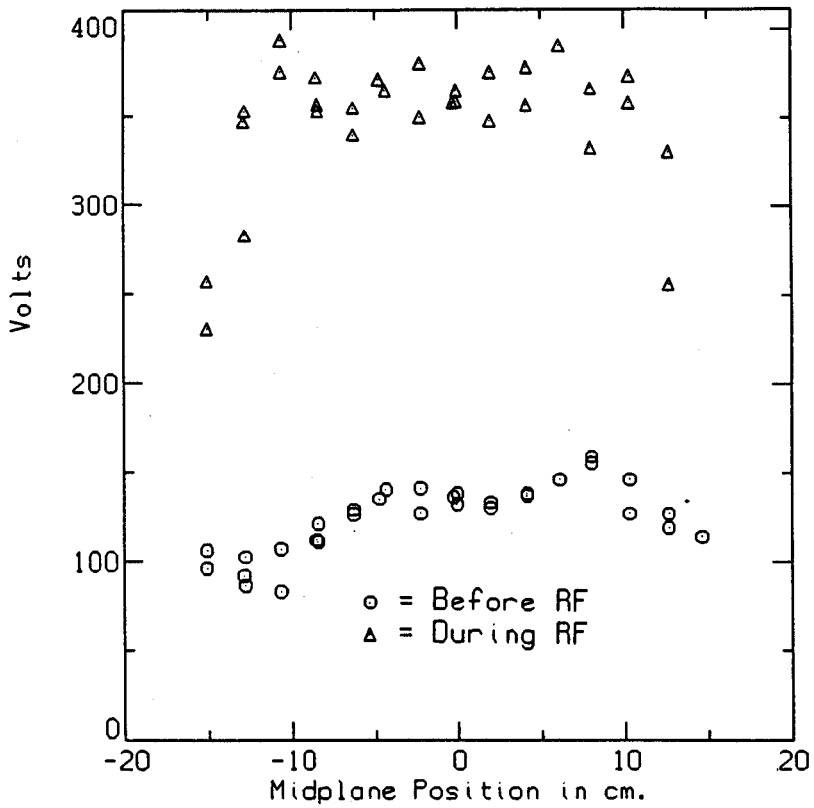

Figure 5-3: The electron confining potential ϕ_0 measured by a electrostatic end loss analyzer in a hydrogen plasma is shown.

gradients, we might expect a larger effect when the potential profile is so changed during application of RF power.

Because this plausibility argument does not constitute experimental proof that the measured transport is diffusive, the diffusion coefficients of the next section are presented with the *caveat* that these are the measured transport coefficients under the assumption that the transport can be described as diffusion (Equation 4.44).

5.2 Diffusion Coefficients

As discussed in the error analysis of section 3.4 about potential measurements, we average $d\phi/d\psi$ over a region of flux in order to reduce the size of the error bars on $d\phi/d\psi$. We divide the plasma column into four regions with the error bars on $d\phi/d\psi$

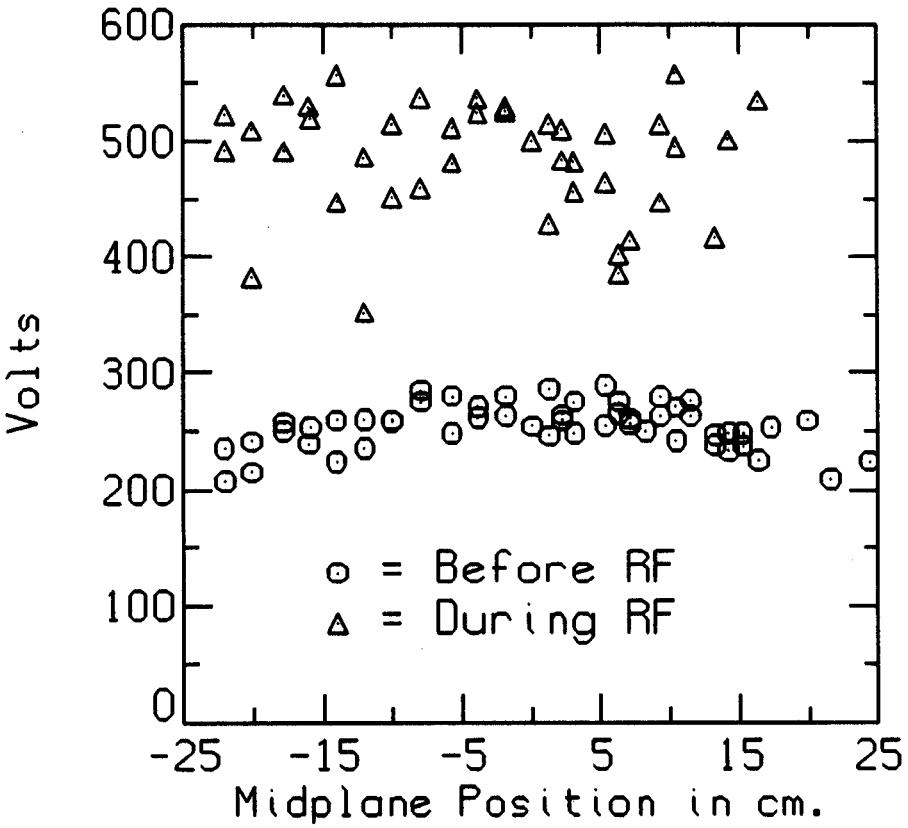

Figure 5-4: The electron confining potential ϕ_0 in an argon plasma is shown.

approximately the same in each region. The regions are: I ($0 < \psi < 33.8cm^2$), II ($33.8 < \psi < 67.6cm^2$), III ($67.6 < \psi < 101.4cm^2$), and IV ($101.4 < \psi < 169cm^2$).

Figures 5-5(a) and (b) and 5-6 show the measured diffusion coefficients calculated using Equation 4.44 and the average values of the various plasma profiles over the four regions of flux for hydrogen, helium and argon plasmas.

Displayed in these figures are two curves, one marked "Without Mobility" and the other labelled "Including Mobility". The mobility term in Equation 4.44 is the contribution to the calculated diffusion coefficient due to the potential gradient $d\phi/d\psi$. The curve marked "Without Mobility" is calculated by setting $d\phi/d\psi = 0$ in Equation 4.44. The curve labelled "Including Mobility" is also the best estimate of the actual value of the diffusion coefficient. When it is smaller than the "Without Mobility" value, both the potential and density gradients are "pushing" ions radially

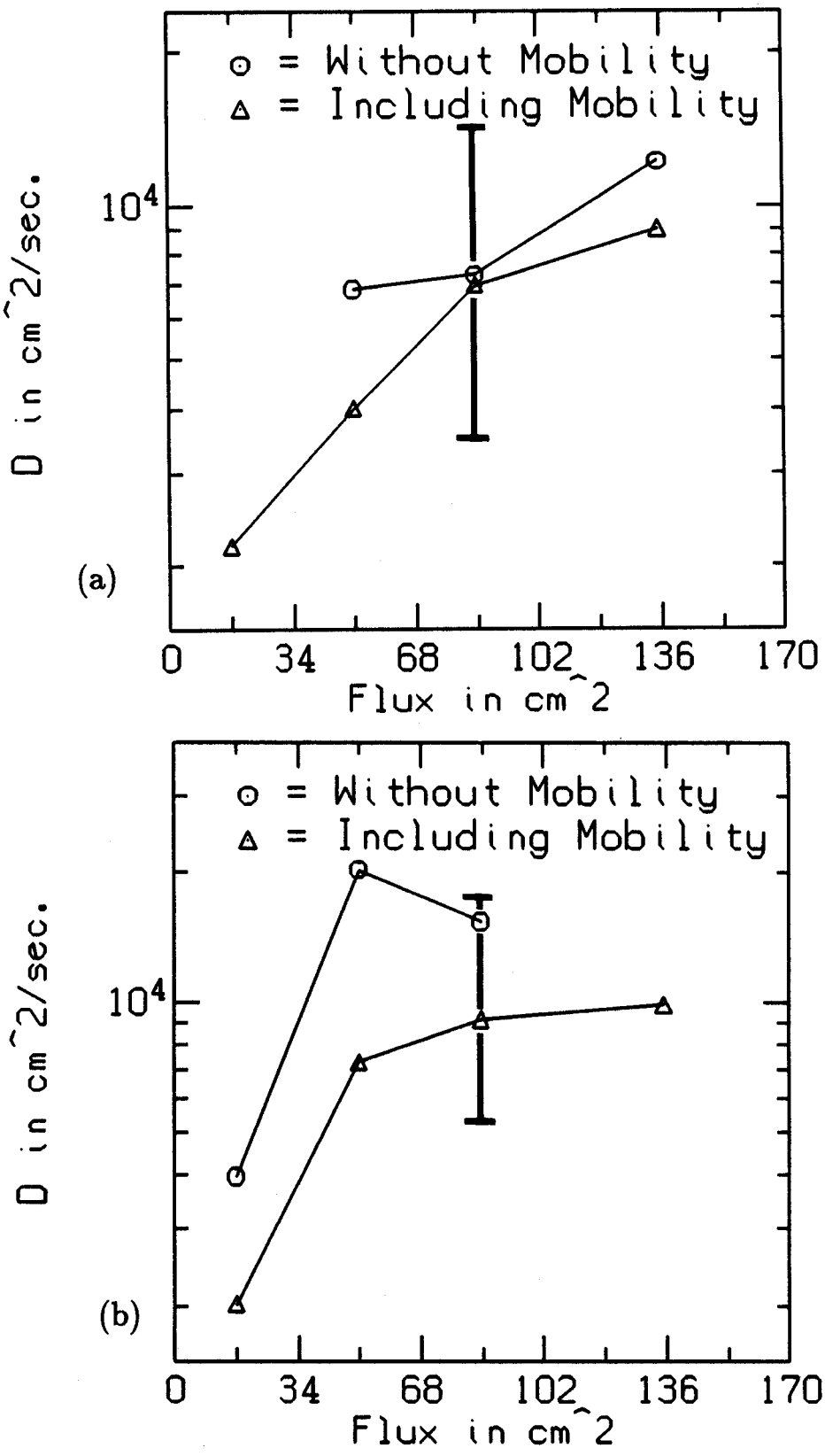

Figure 5-5: (a) Diffusion coefficient for a hydrogen plasma (b) D for a helium plasma.

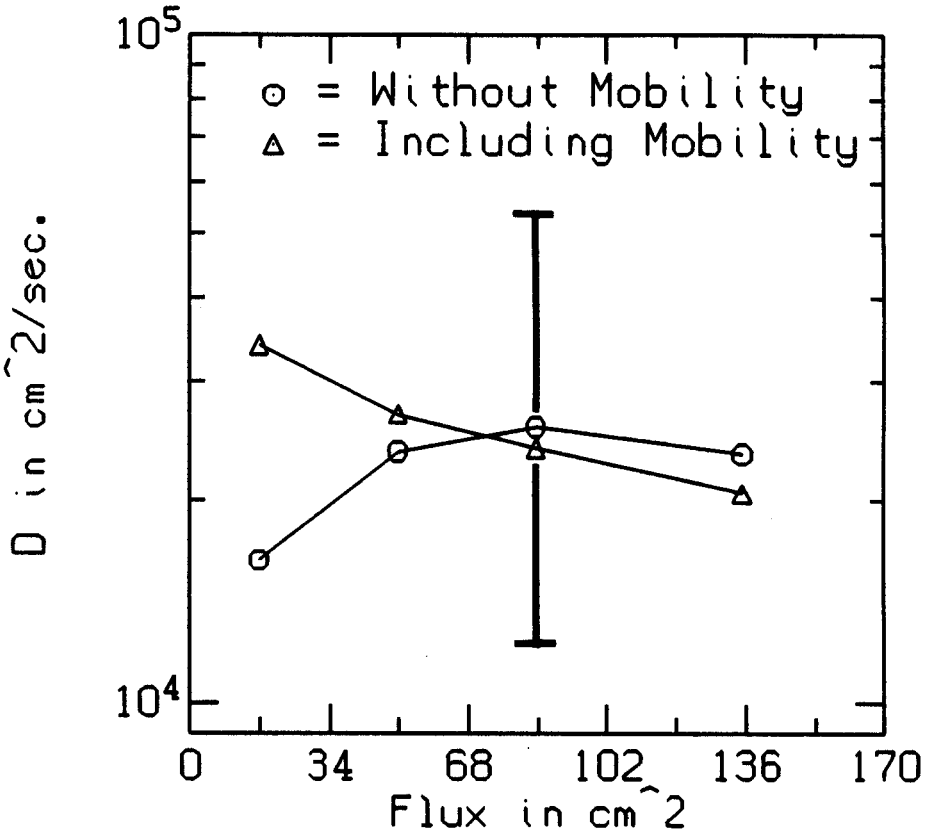

Figure 5-6: The diffusion coefficient for an argon plasma is shown.

outward:

$$\frac{dn}{d\psi} < 0, \ \frac{d\phi}{d\psi} < 0; \ D < D^{no\,\mu} \tag{5.2}$$

When the best estimate for D is greater than the "Without Mobility" value, as is true near the plasma center in argon, it means that the inward force of the potential gradient is partially cancelling the action of the density gradient. As is easily seen from Equation 4.44, a larger D results:

$$\frac{dn}{d\psi} < 0, \ \frac{d\phi}{d\psi} > 0; \ D > D^{no\,\mu} \tag{5.3}$$

$$|\frac{dn}{d\psi}| > |\frac{nZ_{avg}^{in}}{T_i}\frac{d\phi}{d\psi}|$$

The condition on the size of the gradients in Equation 5.3 is required to be able to solve Equation 4.44 when ion transport is radially outward. (Otherwise the denomi-

nator of Equation 4.44 can become zero.) The requirement of Equation 5.3 is always satisfied for the measurements in this thesis.

The average values of the various plasma profiles used to compute the diffusion coefficients of Figures 5-5 and 5-6 are displayed in tables at the end of this chapter. Numerical values for the diffusion coefficients are also given in the tables.

The magnitude of the diffusion coefficients in Figure 5-5 and 5-6 can be compared with the theoretical predictions of Chapter 4 given in Figures 4-6 and 4-7. For all these plasmas, the experimentally measured diffusion coefficient is about a factor of ten larger than the theoretical value. Since the theoretical curves of Figures 4-6 and 4-7 represent the upper limit to the classical and neoclassical diffusion coefficients, *these theories are not sufficient to explain the observed ion radial transport.*

5.3 RF Effects

Low frequency RF power was directed into the plasma using the RF system described in section 2.1 and shown in Figure 2-3. The data in this section was taken using RF fields at a frequency of 1.4 MHz, which is resonant with the ion cyclotron frequency of He^{1+} ions. As predicted in Chapter 4, low frequency RF power increases the radial ion transport rate. Figures 5-7(a) and (b) and 5-8 show the parallel and perpendicular confinement times in hydrogen, helium and argon plasmas. These can be compared with Figures 5-1(a) and (b) and 5-2 to see the effect of RF power on confinement times. RF power decreases $\tau_\perp$ so now all three plasmas have $\tau_\perp < \tau_\parallel$ in the center.

The effect of RF power is also to increase $\tau_\parallel$. This is consistent with the source function remaining approximately the same while $\tau_\perp$ decreases. (See Equation 4.49.) The density and T_{ec} are only slightly perturbed by the RF fields in helium and argon plasmas and somewhat more so in hydrogen.

The diffusion coefficients computed for the period of the shot while 4.4 kV (peak) RF voltage was present on the antenna are shown in Figures 5-9(a) and (b) and 5-10. The diffusion coefficients during RF increases over the pre–RF values of Figures 5-

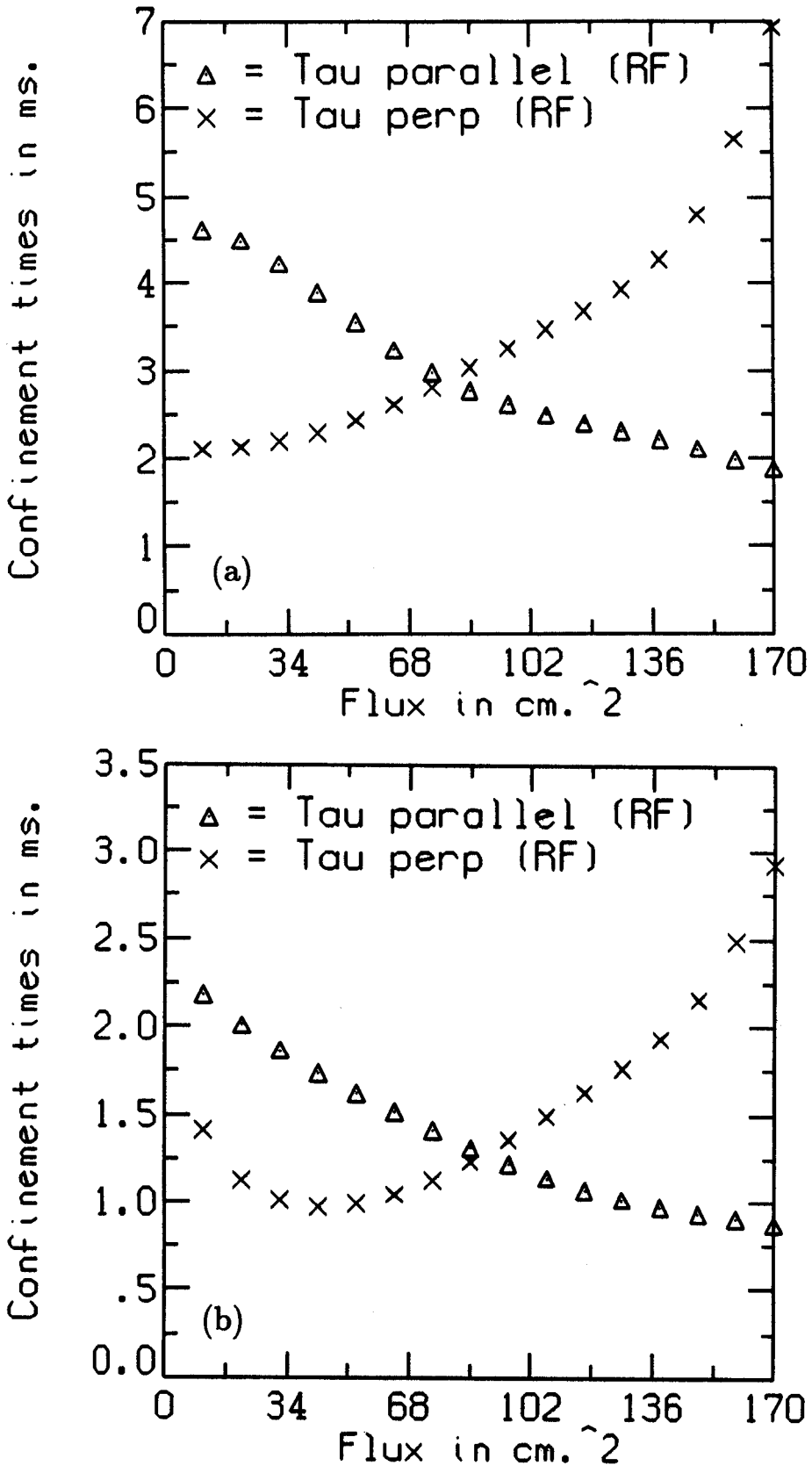

Figure 5-7: Confinement times during application of low frequency RF power in (a) hydrogen and (b) helium plasmas are shown.

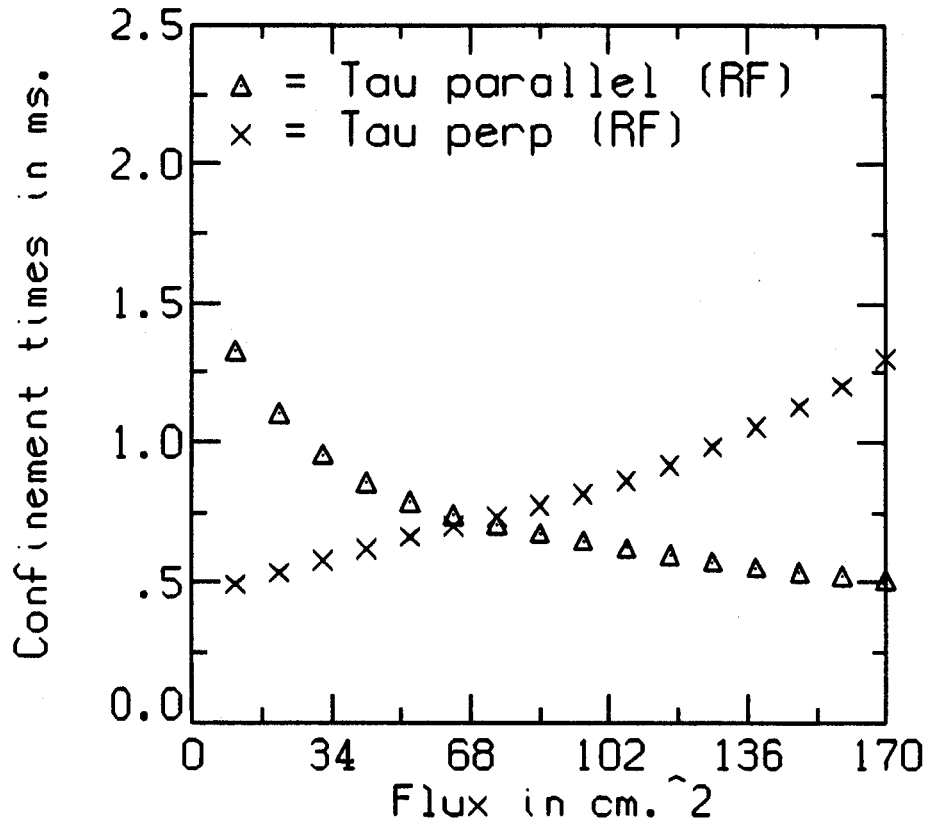

Figure 5-8: Confinement times during application of RF power in an argon plasma is shown.

5 and 5-6. The effect on the diffusion coefficient of the resonant plasma, helium, is approximately twice the effect on hydrogen or argon. To see if this result is an example of the difference between direct and indirect effects as outlined in the previous chapter, data taken at an RF frequency of 5 MHz (resonant with hydrogen ions) was compared with the 1.4 MHz data.

Table 5.1 shows the change in end loss widths and $< x^2 >$ for hydrogen and helium plasmas when RF power is applied. This somewhat qualitative test was used earlier in this chapter to detect the mass scaling of transport rate. To within the error bars of the various measurements, the difference between direct (resonant) and indirect RF effects is not significant.

Part of the reason why it is difficult to detect the direct RF effects is because of the large change in the potential which accompanies RF waves and causes transport via

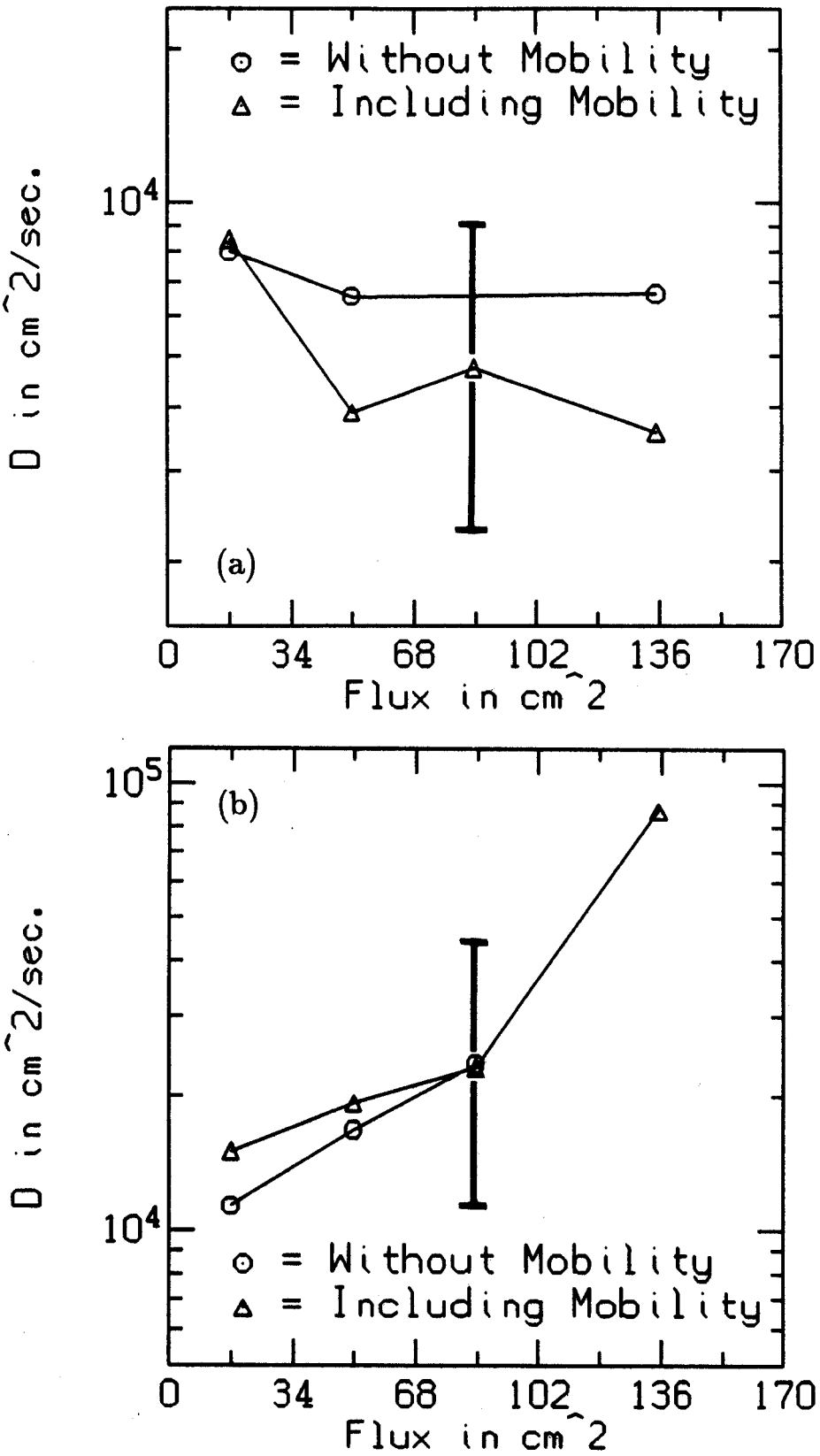

Figure 5-9: Diffusion coefficients for (a) hydrogen and (b) helium plasmas during application of low frequency RF power are shown.

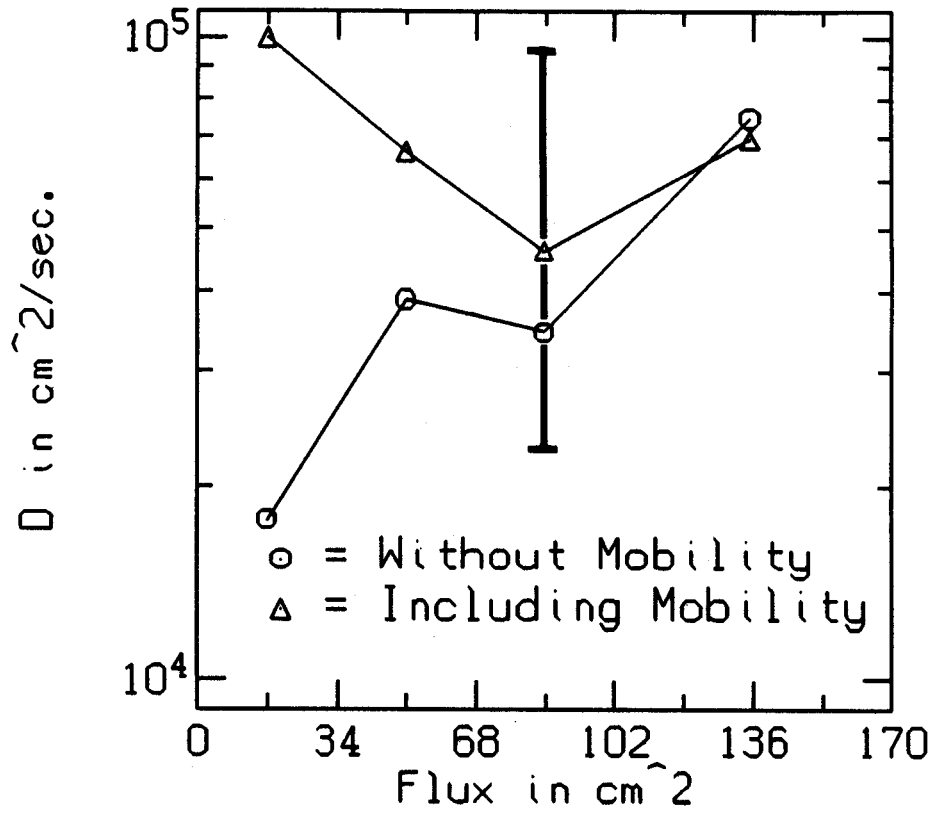

Figure 5-10: Diffusion coefficients for an argon plasma during application of RF power are shown.

ion mobility. As outlined in Chapter 4, a theory to predict the change in normalized potential $\Psi = \phi_0/T_{ec}$ with normalized RF power $\eta = E_{rf}^2/E_0^2$ has been developed [Parks, 1987] and helps explain the large increase in potential during application of RF power.

Figure 5-11 shows the experimentally measured normalized potential $\Psi = \phi_0/T_{ec}$ versus peak RF antenna voltage. The solid curve is the theoretical value replotted from Figure 4-5. In Figure 4-5, the independent variable was η from Equation 4.25. This variable is difficult to directly measure from experiment. It does, however, scale with the square of the easily measurable antenna voltage V_{rf}^2, so we define a normalization constant α:

$$\alpha \equiv \eta/V_{rf}^2 \tag{5.4}$$

The value of α used in Figure 5-11 is a least squares fit between the theoretical

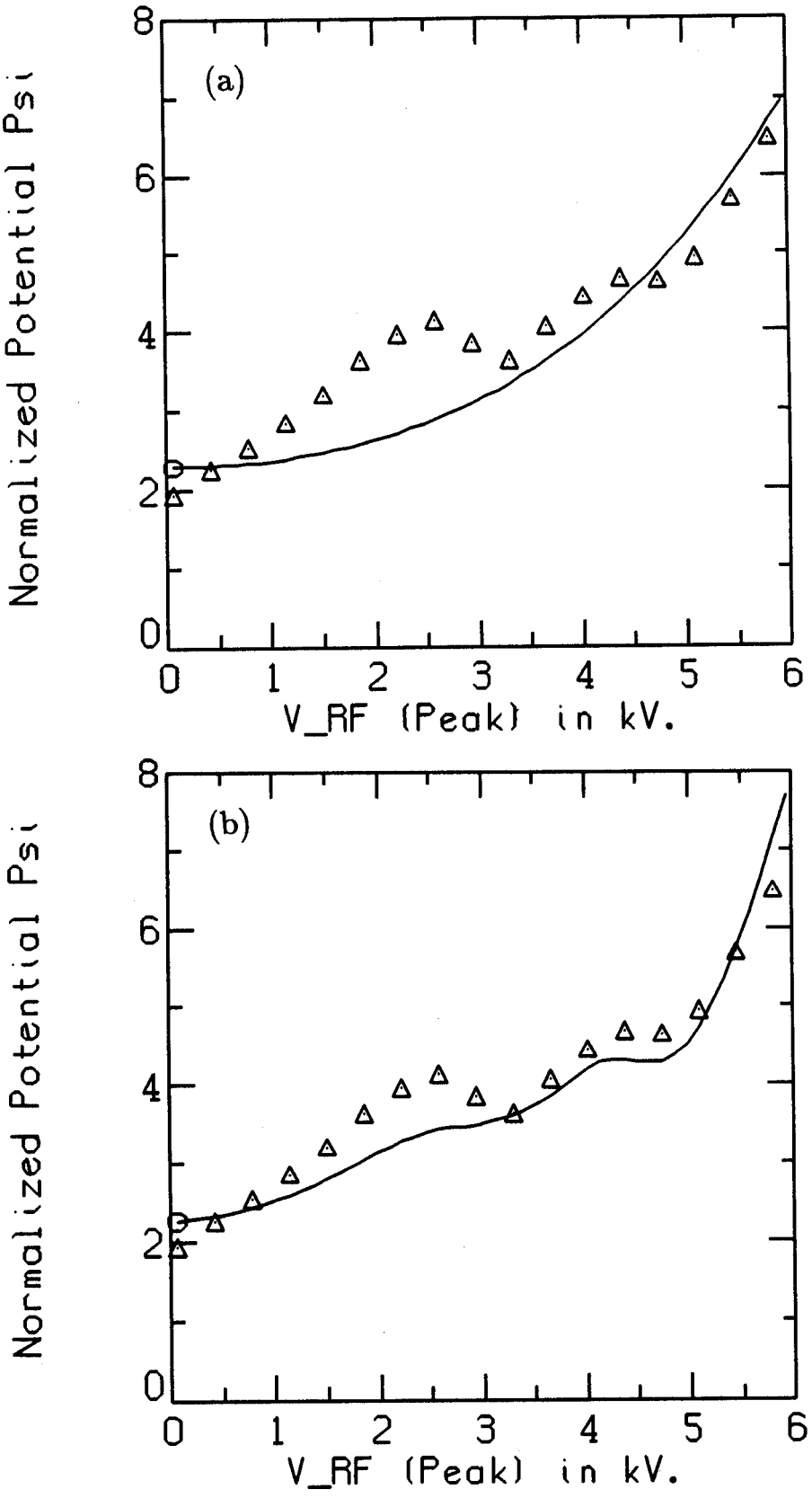

Figure 5-11: The experimental normalized potential $\Psi = \phi_0/T_{ec}$ is shown to compare with the theory outlined in Chapter 4. (a) Zero order theory. (b) Including the change in ν' and ν_e in the theory.

Gas	RF Freq. (MHz)	B_0 (kG)	resonant?	$\Delta FWHM$ (cm) (percent)	$\Delta < x^2 >$ (cm^2) (percent)
H_2	1.4	3.5	no	17	19
H_2	5.0	3.5	no	36	52
He	1.4	3.5	yes	50	65
He	5.0	3.5	no	23	85

Table 5.1: The change in end loss widths during RF for hydrogen and helium plasmas at two RF frequencies is shown.

curve and the experimental data. The value of η thus found for standard operating RF power ($\eta \simeq .14$) is close to that obtained for the similar RF system of RFC–XX–M [Parks, 1987].

As described in Chapter 4, the solid curve of Figure 5-11(a) assumes that the average charge state, loss rate (ν') and electron collisionality (ν_e) are independent of RF power. This is a good zero order approximation, but if we can also use the experimental values for ν' and ν_e we see the fit between theory and experiment for $\Psi(\eta)$ improve. This is shown in Figure 5-11(b).

The perpendicular current density is:

$$J_\perp(\psi) = S(\psi) - J(\psi) \tag{5.5}$$

From Tables 5.2, 5.3 and 5.4 or from comparing the ratio $\tau_\perp/\tau_\parallel$ before and during application of RF power, we find that the fraction of the ionization source which is lost radially, already about 40 percent, increases to 60 percent or more during RF. As mentioned in Chapter 4, if the perpendicular current becomes too large for the ionization source to keep up, equilibrium can be lost.

Figure 5-12 shows a shot where the RF antenna voltage exceeded a threshold

causing a loss of equilibrium. We have coined the term "candle effect" to describe this process: the loss of plasma when the RF power is turned on is analogous to the blowing out of a candle. The figure shows that during candle effect, the cold electrons and most of the plasma density are lost, leaving only the hot electrons. This can be seen in the large drop in microwave interferometer signal and the less severe drop in diamagnetism.

In general, the cold electron density decreases slightly ($<$ 10 percent) when RF power is applied. This decrease scales linearly with RF antenna voltage. When the RF voltage exceeds a well defined threshold, the density decrease is no longer linear with RF voltage, but exhibits a discontinuity in slope. Figure 5-13 shows that the value of RF voltage at which candle effect occurs is a strong function of pressure. A sharp candle effect boundary is reasonable because when plasma is lost, so if the shielding of the RF electric field. With a stronger RF electric field more plasma is lost, causing a self–sustaining loss of equilibrium.

The fraction of the source which is lost perpendicularly from the flux surface ψ during application of RF power is:

$$f(\psi) = J_{\perp}/S(\psi)$$

Since there will always be some parallel losses, we expect a threshold for loss of equilibrium when f exceeds some critical value. Figures 5-14(a) and (b) show the perpendicular fraction f for hydrogen and helium plasmas. The maximum V_{rf} shown is at the threshold for loss of equilibrium. The critical fraction f is between 0.7 and 0.8.

Error Analysis

From Equation 4.44, the computed diffusion coefficient D depends on the measured values of S, J, Z^{in}_{avg}, $d\bar{n}/d\psi$, $\bar{n}$, T_i and $d\phi/d\psi$. The majority of the error is in $d\phi/d\psi$, as discussed in Chapter 3. To a good approximation, the error bars on D when

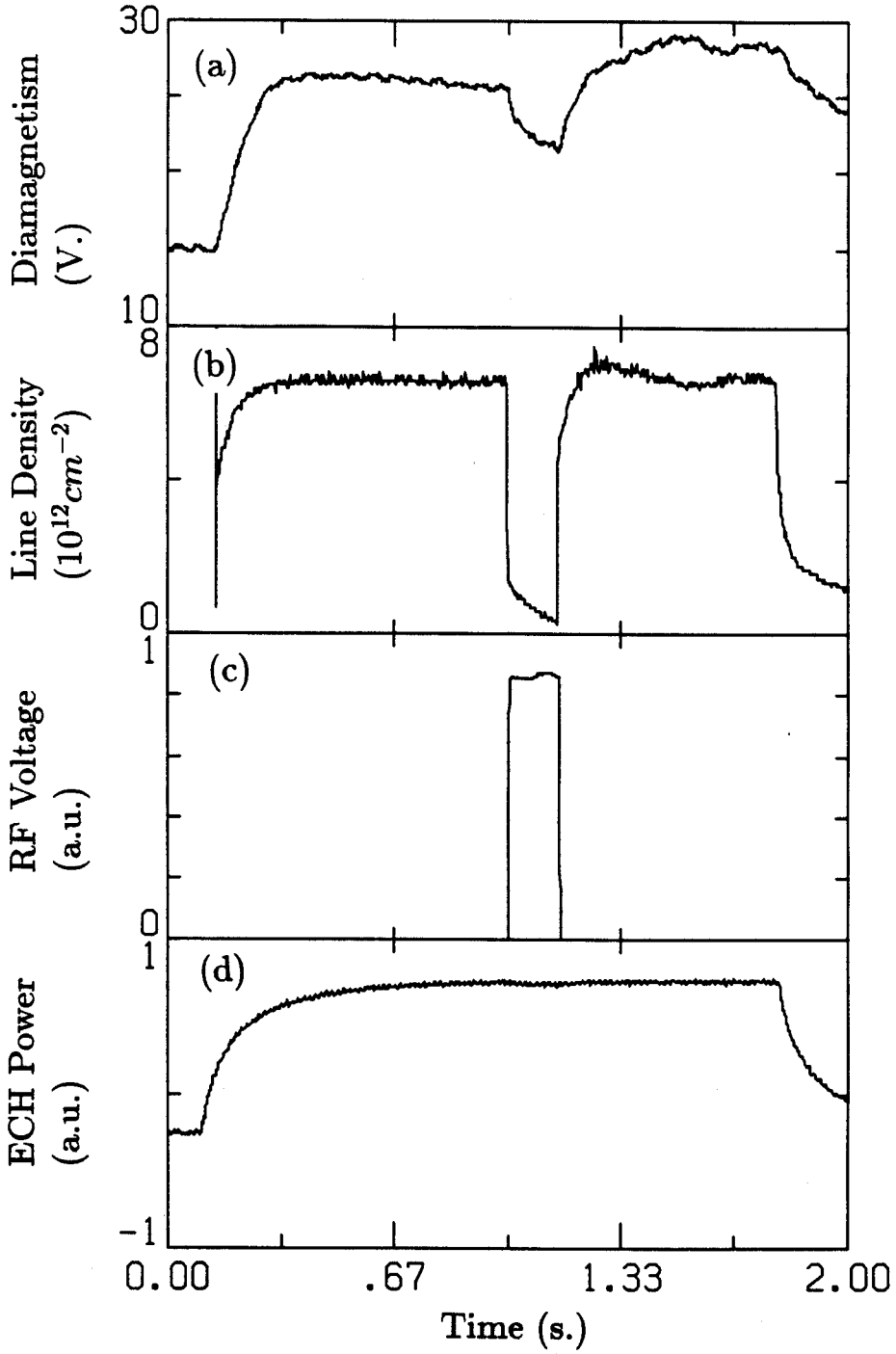

Figure 5-12: When the RF antenna voltage exceeds a pressure dependent threshold, equilibrium is lost. (a) The diamagnetism drops less than (b) the line density measured by interferometer, indicating that cold electrons are lost but hot electrons remain. (c) The RF antenna voltage and (d) Electron Cyclotron (ECH) microwave power signals are also shown.

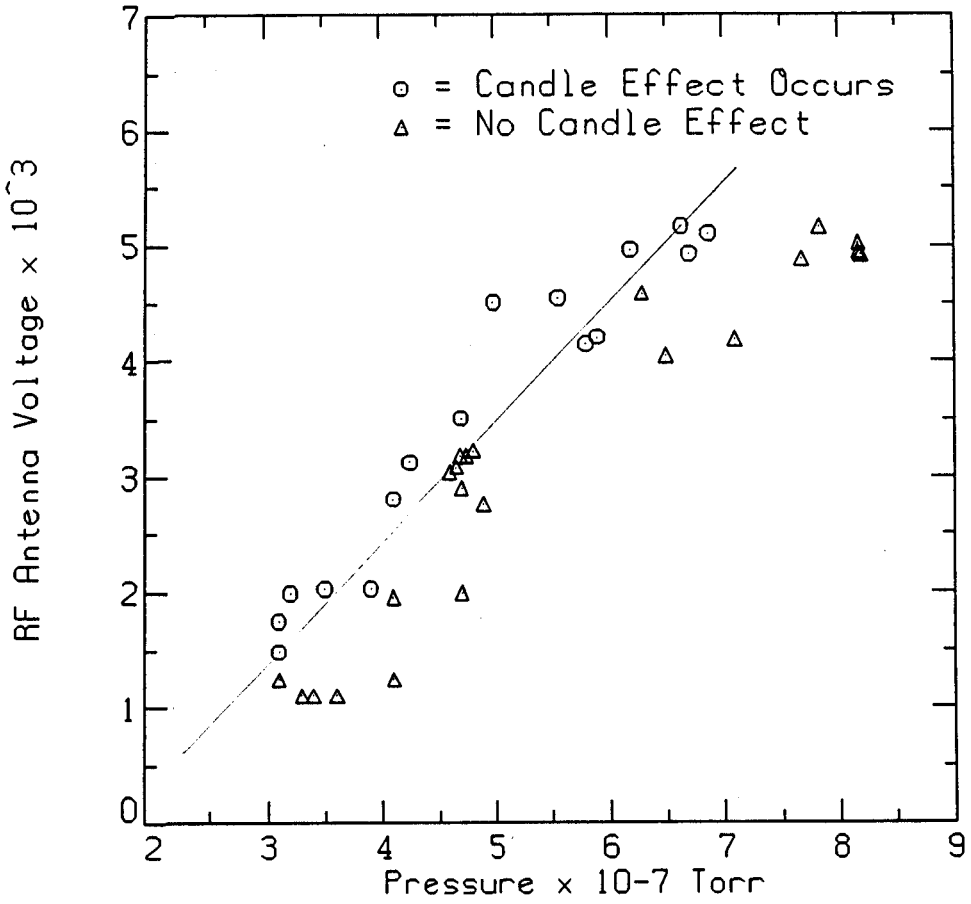

Figure 5-13: Loss of equilibrium (candle effect) occurs when the RF antenna voltage exceeds a pressure dependent threshold, as shown in this figure.

mobility is included is:

$$\frac{\sigma_D}{D} = \frac{\sigma_{\phi'}}{d\phi/d\psi + T_i/\bar{n}Z^{in}_{avg}d\bar{n}/d\psi} \tag{5.6}$$

This gives a diffusion coefficient known within a factor of 2, as shown in Figures 5-5, 5-6, 5-9 and 5-10. Without including the mobility term, the diffusion coefficient is known about a factor of three better. (The error bars can then be computed by combining the error bars on $d\bar{n}/d\psi$, S and J.)

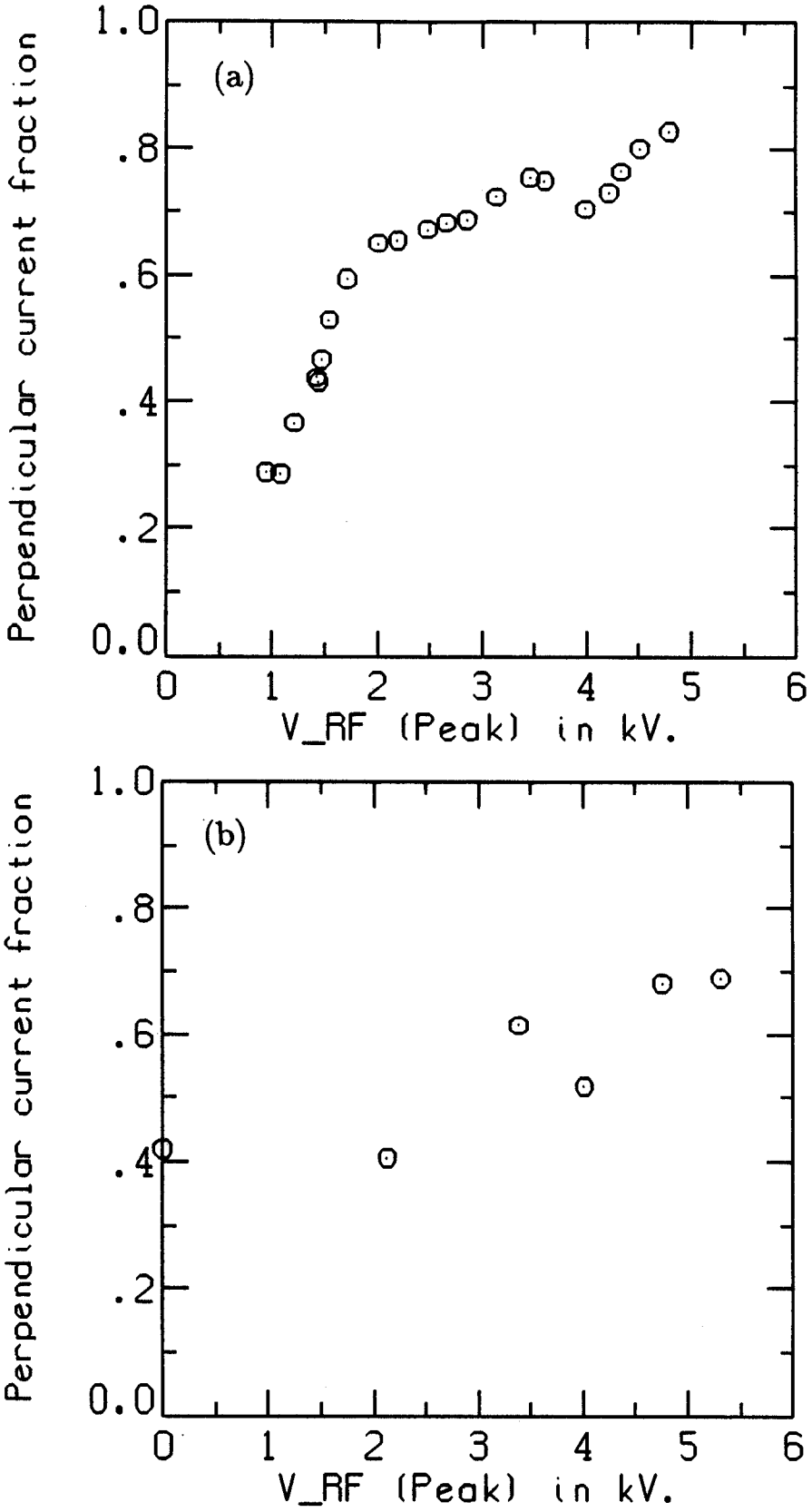

Figure 5-14: The fraction of the ionization source which becomes perpendicular current is shown. The maximum RF antenna voltage points are the threshold for loss of equilibrium. (a) Hydrogen plasma (b) Helium plasma.

Hydrogen Plasma Before RF

ψ $(cm.^2)$	0.–33.8	33.8–67.6	67.6–101.4	101.4–169.
$d\phi/d\psi$ $(V./cm.^2)$	-0.233	-0.757e-1	-0.948e-2	-0.898e-1
$\bar{n}$ (Dimensionless)	0.934	0.643	0.232	0.044
$(d\bar{n}/d\psi)$ $(cm.^{-2})$	0.216e-2	-0.138e-1	-0.883e-2	-0.220e-2
$2 * \int(S-J)d\psi$ $(mA.)$	18.8	58.8	67.0	44.6
D, including μ $(cm.^2/sec.)$	2.2×10^3	4.0×10^3	7.0×10^3	9.0×10^3

Hydrogen Plasma During RF

ψ $(cm.^2)$	0.–33.8	33.8–67.6	67.6–101.4	101.4–169.
$d\phi/d\psi$ $(V./cm.^2)$	0.442e-2	-0.113e0	-0.252e0	-0.504e0
$\bar{n}$ (Dimensionless)	0.771	0.308	0.133	0.025
$(d\bar{n}/d\psi)$ $(cm.^{-2})$	-0.132e-1	-0.103e-1	-0.129e-2	-0.297e-2
$2 * \int(S-J)d\psi$ $(mA.)$	19.2	36.8	34.6	28.6
D, including μ $(cm.^2/sec.)$	8.5×10^3	3.9×10^3	4.8×10^3	3.6×10^3

Table 5.2: The average value of each plasma profile for the four regions of flux are shown for a hydrogen plasma under standard conditions. Also shown are the average values during application of low frequency RF power.

Helium Plasma Before RF

ψ $(cm.^2)$	0.–33.8	33.8–67.6	67.6–101.4	101.4–169.
$d\phi/d\psi$ $(V./cm.^2)$	-0.186	-0.225	-0.196	-0.284
$\bar{n}$ (Dimensionless)	0.502	0.228	0.0811	0.0476
$(d\bar{n}/d\psi)$ $(cm.^{-2})$	-0.0158	-0.00464	-0.00388	0.
$2 * \int (S - J) d\psi$ $(mA.)$	27.4	124.	130.3	75.8
D, including μ $(cm.^2/sec.)$	2.0×10^3	7.3×10^3	9.2×10^3	9.9×10^3

Helium Plasma During RF

ψ $(cm.^2)$	0.–33.8	33.8–67.6	67.6–101.4	101.4–169.
$d\phi/d\psi$ $(V./cm.^2)$	0.116	0.827e-1	-0.168e-1	-0.154
$\bar{n}$ (Dimensionless)	0.623	0.260	0.736e-1	0.396e-1
$(d\bar{n}/d\psi)$ $(cm.^{-2})$	-0.138e-1	-0.798e-2	-0.318e-2	-0.859e-4
$2 * \int (S - J) d\psi$ $(mA.)$	56.8	146.4	136.4	93.2
D, including μ $(cm.^2/sec.)$	1.5×10^4	1.9×10^4	2.3×10^4	8.7×10^4

Table 5.3: The average value of each plasma profile for the four regions of flux are shown for a helium plasma under standard conditions. Also shown are the average values during application of low frequency RF power.

Argon Plasma Before RF

ψ $(cm.^2)$	0.–33.8	33.8–67.6	67.6–101.4	101.4–169.
$d\phi/d\psi$ $(V./cm.^2)$	0.234	0.864e-1	0.382e-1	0.369e-1
$\bar{n}$ (Dimensionless)	0.604	0.239	0.097	0.012
$(d\bar{n}/d\psi)$ $(cm.^{-2})$	-0.180e-1	-0.606e-2	-0.305e-2	-0.880e-3
$2 * \int(S-J)d\psi$ $(mA.)$	40.2	58.8	53.8	22.6
D, including μ $(cm.^2/sec.)$	3.4×10^4	2.7×10^4	2.4×10^4	2.1×10^3

Argon Plasma During RF

ψ $(cm.^2)$	0.–33.8	33.8–67.6	67.6–101.4	101.4–169.
$d\phi/d\psi$ $(V./cm.^2)$	0.498	0.171	0.193	0.673e-1
$\bar{n}$ (Dimensionless)	0.547	0.218	0.999e-1	0.160e-1
$(d\bar{n}/d\psi)$ $(cm.^{-2})$	-0.193e-1	-0.444e-2	-0.312e-2	-0.712e-3
$2 * \int(S-J)d\psi$ $(mA.)$	49.6	75.4	78.4	62.2
D, including μ $(cm.^2/sec.)$	1.0×10^5	6.6×10^4	4.6×10^4	6.9×10^4

Table 5.4: The average value of each plasma profile for the four regions of flux are shown for an argon plasma under standard conditions. Also shown are the average values during application of low frequency RF power.

Chapter 6

Conclusions

6.1 Summary of Results

The major results of this thesis fall into two areas: the measurement of the ion radial transport rate in a nonaxisymmetric mirror and the effect of low frequency RF power on ion transport and plasma parameters.

Radial ion transport is a much more important loss mechanism than expected from the predictions of classical and neoclassical transport theories. The bulk ion parallel and perpendicular confinement times under standard conditions are within a factor of two of each other for hydrogen, helium and argon plasmas. By measuring all the relevant plasma profiles, including density, source function, end loss and ion and electron temperatures, diffusion and mobility coefficients are found. The coefficients are a factor of ten larger than the maximum coefficients predicted by classical and neoclassical theories.

Application of low frequency RF power increases the ion radial transport rate, with the effect increasing with RF antenna voltage. During RF, perpendicular transport becomes the dominant ion loss mechanism. When the RF antenna voltage exceeds a well defined threshold, the ionization source function cannot keep up with perpendicular losses and the equilibrium is lost. The plasma potential is also increased during application of RF power, with the scaling of potential with RF power in agreement

with a theory describing the RF–electron interaction. If we assume that transport during RF is diffusive in nature, then RF power increases transport by increasing the diffusion coefficient, rather than by steepening the potential gradient. The effect is thus a direct effect, rather than an indirect effect via the electrons. Since the transport rate before application of RF power was larger than expected, it is not clear that we are justified in using a diffusive model during RF at all. The effect of RF power on the diffusion coefficient of resonant ion species seems to be larger than on nonresonant species, but the data is inconclusive in this area.

6.2 Observations

In the absence of destructive macroscopic instabilities, it has been assumed that classical and neoclassical transport theories adequately describe radial ion transport in mirror systems. These theories have been used to design experiments, and as a framework for interpretation of results. The Constance B quadrupole mirror represents a counter example for this procedure, because although it is macroscopically stable, [X. Chen, 1988] the measured diffusion coefficients are an order of magnitude larger than expected.

We have found that both diffusion due to the density gradient and mobility due to the potential gradient contribute to ion radial transport, with the former dominating by about a factor of two in most cases.

This is an unexpected result, since if one naively uses $d\phi/d\psi \simeq \phi_0/a$, where a is some radial scale length, then mobility would be by far the most important effect for our low density and ion temperature. However, $\phi(\psi)$ is quite flat throughout most of the plasma, dropping quickly at the edge, and thus $d\phi/d\psi \ll \phi_0/a$.

Previous attempts to test neoclassical theory (i.e. [Hooper, et al., 1985]) have assumed $d\phi/d\psi$ proportional to ϕ_0 and tested the scaling of $\tau_\perp$ with ϕ_0. In fact, this argument motivated the article [Parks, 1987] whose predicted scaling of ϕ_0 with RF power is compared with experiment in this thesis. Although low frequency RF

power increases ion radial transport, the mechanism was unexpected. The potential gradient $d\phi/d\psi$ is not steepened by the RF power, but instead the diffusion coefficient is increased; a direct rather than an indirect effect. Another possibility that should be considered is that the transport during application of RF power is not diffusive in nature, in which case neither the original Park's theory nor the diffusion coefficient presentation of this thesis is applicable.

One reason there are so few quantitative tests of transport theories is because transport measurements are difficult. Transport measurements using probes, limiters and impurity injection on Constance were all attempted before the procedure outlined in this thesis was adopted. For various reasons each method failed to provide believable transport coefficients which could be compared to theory.

Transport measurements require the "tagging" of particles to follow their radial motion. Such experiments fall into two broad categories: time dependent measurements and equilibrium or steady state measurements.

By injecting carbon ions at a single point in space and time and following the ions using spectroscopy and end loss measurements, the time evolution of radial position can be fitted to the time dependent diffusion equation and a diffusion coefficient deduced. This is an example of a time dependent measurement where the impurity test particles are "tagged" by their atomic behavior and q/m ratio.

By modulating the end wall plate potential at a low frequency and measuring the radial ion flux to probes or a limiter, a mobility coefficient can be found. The modulation is done sufficiently slowly so that the plasma is always in equilibrium, and the ions are "tagged" because the modulated potential which pushes them outwards would be expected to occur mainly on field lines which map to the swept end wall plate. This is an example of an equilibrium or time–independent transport measurement. Unfortunately, the carbon arc injection experiment greatly perturbes the plasma, and electron cross field transport makes localization of a $\Delta\phi$ impossible.

The magnetic mirror geometry is, however, well suited to the type of equilibrium transport measurement described in this thesis. The existence of end loss allows

measurement of both the source and loss functions, and when done carefully, allows measurement of the radial dependence of transport coefficients. This is in contrast to toroidal devices, whose loss function is not accessible, and whose transport coefficients may be even more difficult to measure than those in mirrors!

The disparity between classical and neoclassical transport theories and experimentally determined transport rates which, with this thesis is new to mirror systems, has been long recognized by the toroidal community.

The electron energy transport rate for ohmically heated tokamaks exceeds neoclassical theory by an order of magnitude or more, with various turbulence theories attempting to account for the "anamalous" transport [Liewer, 1985]. Ion transport in tokamaks in the 1970's was thought to be within a factor of two of neoclassical, but with better $T_i(r)$ profile measurements and more complete neoclassical theories [Hirshman and Sigmar, 1981] the agreement between theory and experiment for ion transport has in general worsened.

There have been some cases where neoclassical theory seems to well describe ion transport in toroidal systems. Pellet injection in Alcator–C produced a peaked density profile which inhibited sawtooth oscillations and was well described by neoclassical predictions [Greenwald, et al., 1984,Petrasso, et al., 1986]. Collisional plasmas in the Wisconsin Octupole were also well decribed by classical transport theory, in contrast to the anamalous transport observed when the plasma parameters were in a collisionless regime [Navratil, et al., 1979].

Seen in this context, the results of this thesis represent one more example of the failure of classical and neoclassical transport theories to adequately describe radial particle transport in a magnetic confinement geometry.

In addition to its interest to the plasma physics community as a comparison of transport theory with experiment, the specific information in this thesis may be of interest to several groups of researchers. If the mirror confinement concept is ever revived, the material in this thesis has obvious relevance to the design of nonaxisymmetric cells of tandem mirrors. The use of nonaxisymmetric ECR ion sources for high

energy physics and plasma deposition has increased in recent years. Cross field ion transport will limit the confinement time of ions and thus the maximum attainable charge state and ion flux in these sources. Plasma deposition devices run at higher pressures, and ion–neutral collisions should probably determine the perpendicular transport rate in these devices. Finally, some of the experimental methods devised for this thesis may be of interest to other physicists. In particular, the two dimensional T_{ec} measurement using the CCD camera and optical bandpass filters is a novel technique, which we believe has not been used before this study.

6.3 Suggestions for Future Work

The obvious question which remains is: *Why are the radial transport coefficients so large?* Low frequency fluctuations ($\omega \leq \Omega_i$) together with collisions may be responsible. The theory would be similar to that presented by Putvinskij to model enhanced electron radial transport due to flute waves and collisions [Putvinskij and Timofeev, 1975]. A study of low frequency fluctuations in potential and density might shed some light on this issue. Theoretical work is being done [Petty, 1988] to see if ion acoustic wave frequency turbulence could be responsible for both the enhanced radial transport rate and the anomalously high ion temperatures shown in Figure 3-26. The theory may explain the temperature mass dependence as well as the magnitude of the radial diffusion coefficient.

More experiments of the same type as described in this thesis would probably clarify how much stronger is the transport of RF resonant ions than nonresonant ions. Experiments would require several runs at a variety of RF frequencies examining the diffusion coefficients of various ion species.

Appendix A

Atomic Physics

The measurement of cold electron temperature, plasma density and ionization source function all require knowledge of a variety of atomic physics processes. In many cases, the necessary information is the ratio of temperature dependent atomic cross sections. This appendix contains the experimental data and analytical and numerical models used in this thesis for converting raw data into plasma profiles.

A.1 Line Ratios

A partial Grotrian diagram for helium is shown in Figure A-1. The width of the arrows gives an indication of the relative rates of the various processes at T_{ec}= 100 eV. The states $He^*(1s2s|^1S)$ and $He^*(1s2s|^3S)$ are metastable and are populated at a rate much faster than the n=3 and n=4 levels. Thus if these excited atoms are in the plasma for a sufficiently long time, two step population of the n=3 and n=4 levels via metastable intermediate states will occur. Fortunately for our analysis, in Constance the mean free path of these excited atoms is very long compared with the plasma radius:

$$\lambda_{mfp} = \left[\frac{n_e < \sigma v >}{v_{He}}\right]^{-1} \geq \left[\frac{(2 \times 10^{11})(1 \times 10^{-11})}{1.1 \times 10^5}\right]^{-1} = 5 \times 10^4 cm$$

Thus the metastable state atoms hit the wall and become $He(1s^2|^1S)$ and in very few cases contribute to the population of the n=3 and n=4 states. A simplified

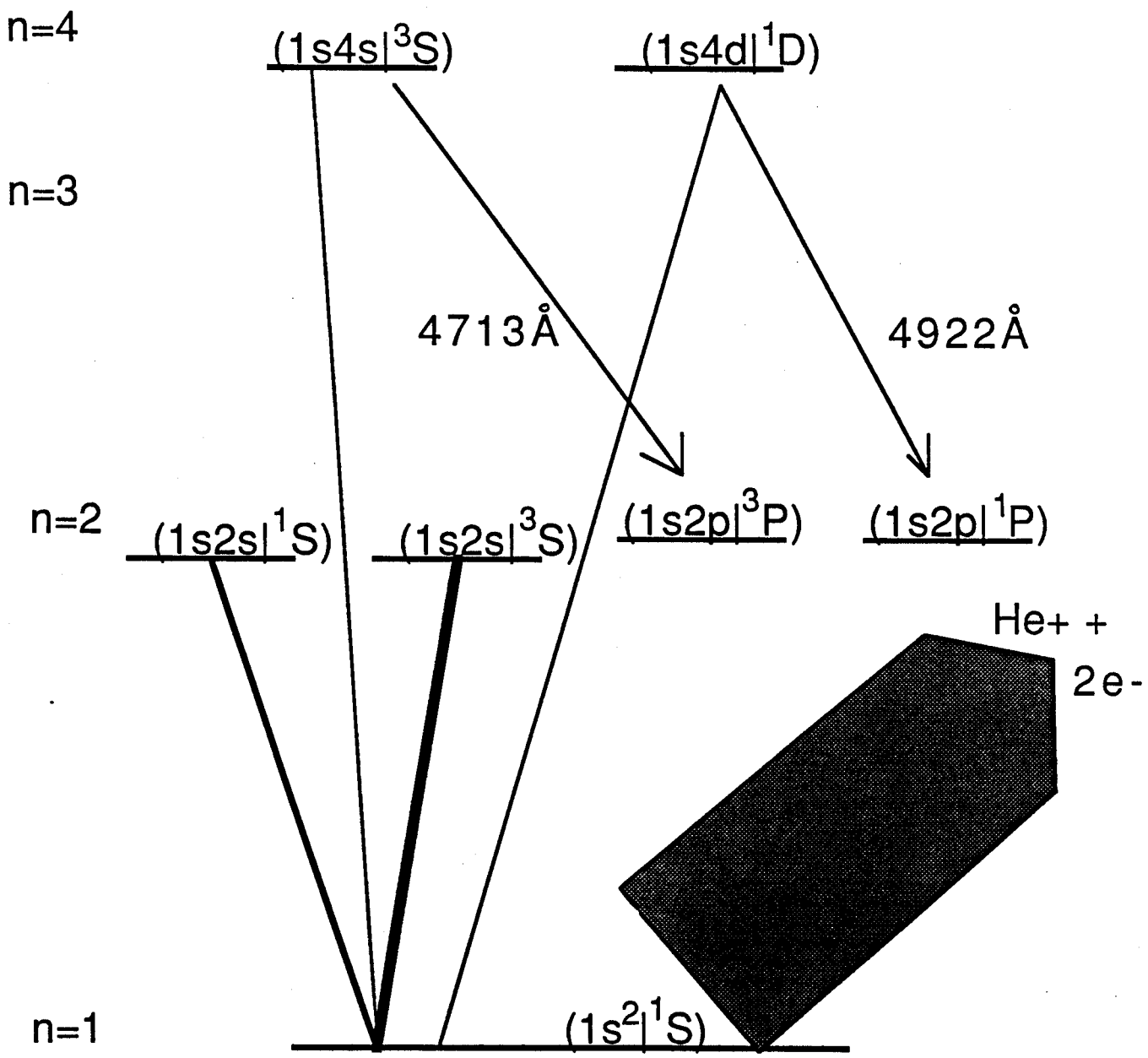

Figure A-1: A simplified Grotrian energy level diagram for helium shows the n=4 states used for electron temperature measurements. Metastable n=2 levels are also shown.

one-step collisional excitation, radiative relaxation model is therefore applicable to Constance.

Figure A-2(a) shows experimental and theoretical electron excitation cross sections for population of the 4^1D state which decays primarily (75 percent) to 2^1P (4922 $\AA$). The theoretical cross section shown is:

$$\sigma_s(u) = 4.0 \times 10^{-19} \frac{u-1}{u^2} cm^2 \tag{A.1}$$

with $u = E_e/E_{thr}$, and the threshold energy is $E_{thr} = 24.0$eV.

This is a simplification of the Born approximation result [Johnson and Hinov, 1969, Janev, et al., 1985]

$$\sigma(u) = 3.5 \times 10^{-16} B(\frac{Ry}{E_{nl}^{exc}}) Y(u) \tag{A.2}$$

$$Y(u) = \frac{1}{u^2}\left[1 - \exp(-tu)\right](u - .8)$$

$$t = 0.8B^{-.7}\left[\frac{Ry}{4E_{ion}^{He}}\frac{E^{exc}}{E_{nl}^{ion}}\right]^{0.3}$$

with Ry=13.6 eV., E_{ion}^{He}=24.59 eV., E_{nl}^{exc}=24.0 eV., and $E_{nl}^{ion} = E_{ion}^{He} - E_{nl}^{exc}$.

The complicated expression A.2 accurately treats the behavior of the cross section at threshold. However, this is not required for our analysis.

Figure A-2(b) shows experimental and theoretical excitation cross sections for the population of the 4^3S state which decays primarily (62 percent) to 2^3P (4713 $\AA$) The theoretical cross section shown is:

$$\sigma_t(u) = 1.01 \times 10^{-18}(u^{-3} - u^{-5}) cm^2 \tag{A.3}$$

with u defined above.

Both theoretical cross sections agree with the experimental data on the position and value of the cross section maximum, and differ by $\leq$ 30 percent over the range $40 \leq E_e \leq 100$ eV. The theoretical curves are the current best estimates [Janev, et al., 1985], have the correct high energy asymptotic limits, and are used exclusively in this thesis.

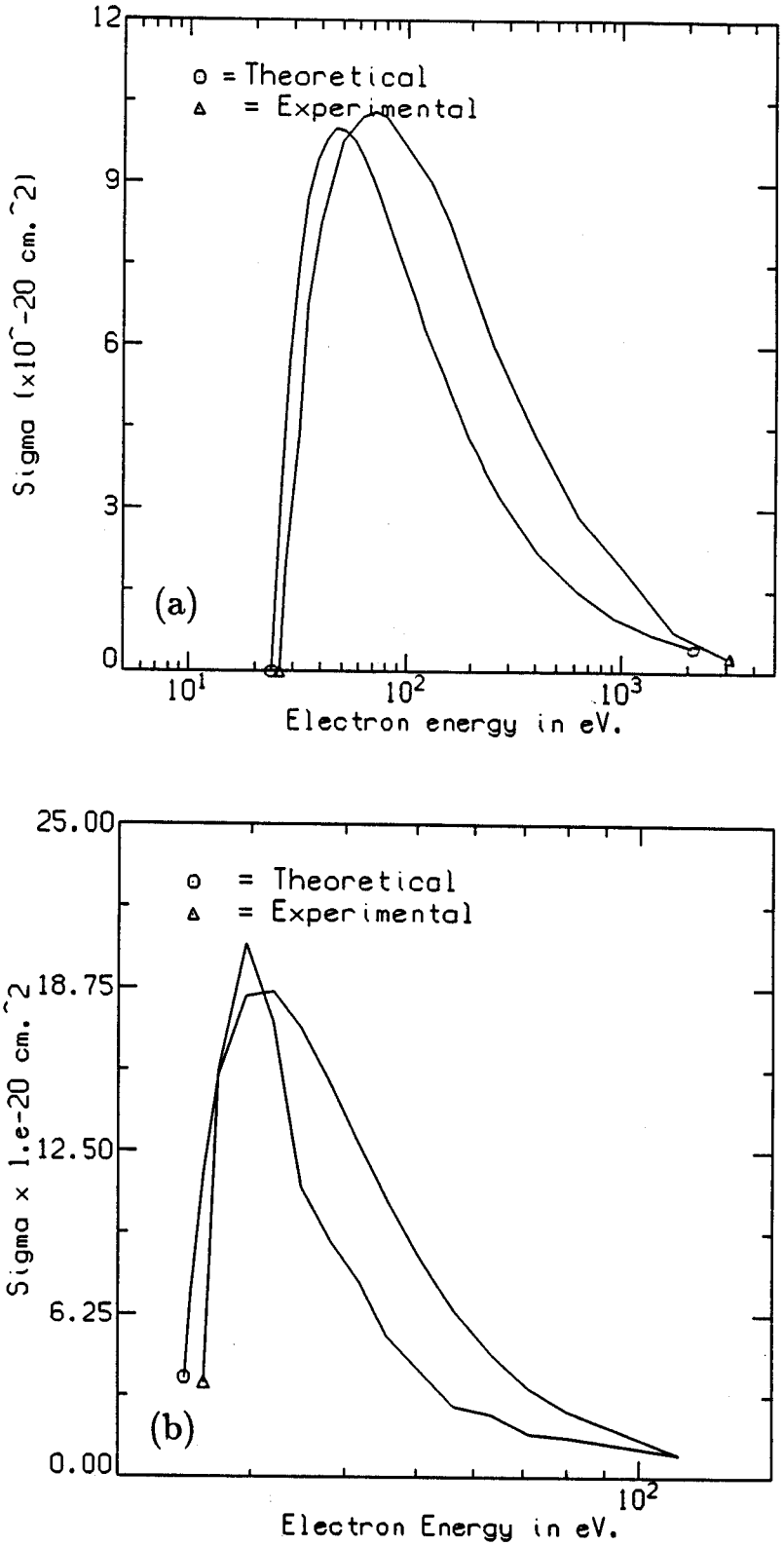

Figure A-2: (a) Excitation cross section for the helium 4922 $\AA$ line. (b) Excitation cross section for the helium 4713 $\AA$ line.

Averaging the experimental cross sections over an assumed cold electron maxwellian velocity distribution requires the evaluation of:

$$< \sigma v >= \frac{2v_{exc}}{\sqrt{\pi}u_0^{3/2}} \int_0^\infty \sigma(u) u \exp(-u/u_0) du \qquad (A.4)$$

where $u_0 = u_{thresh}/u_e$, u_e= electron temperature in eV., and $v_{exc} = 4.19 \times 10^7 \sqrt{24eV.} = 2.05 \times 10^8$ cm./sec.

Substituting expressions A.2 and A.3 into A.4 yields the analytic results:

$$< \sigma v >_s = 9.26 \times 10^{-11} u_0^{-3/2} [E_0(1/u_0) - E_1(1/u_0)] \, cm^3/sec. \qquad (A.5)$$

$$< \sigma v >_t = 2.34 \times 10^{-10} u_0^{-3/2} [E_2(1/u_0) - E_4(1/u_0)] \, cm^3/sec.$$

and an analytic expression for the line ratio:

$$R(u_0) = 2.53 \frac{E_2(1/u_0) - E_4(1/u_0)}{E_0(1/u_0) - E_1(1/u_0)} \qquad (A.6)$$

where $E_n(x)$ is the exponential integral of order n [Abramowitz and Stegun, 1970].

Figure A-3 shows this ratio for electron temperatures of 15eV.–5keV. Figure 3-1 is Figure A-3 with the region from 15–200eV. expanded. A simple extension of Equation A.6 for a bimaxwellian electron distribution is:

$$R(u_0, u_h, f_h) = 2.53 \frac{(\frac{u_0}{u_h})^{3/2} f_h (E_2 - E_4)_h + (1 - f_h)(E_2 - E_4)_0}{(\frac{u_0}{u_h})^{3/2} f_h (E_0 - E_1)_h + (1 - f_h)(E_0 - E_1)_0} \qquad (A.7)$$

where $f_h = n_h/(n_h + n_c)$, and the subscript indicates that the integral should be evaluated for $x = 1/u_0$ or $x = 1/u_h$.

Figures 3-1 and A-3 also include curves for a bimaxwellian distribution function in which half of the density is assumed to be hot electrons with a temperature of 100 keV. The figures shows that the hot component has a negligible effect on the line ratio, and thus the line ratio is a measure of the cold electron temperature.

A standard reference [McWhirter, 1965] uses experimental data [Lees, 1932] to obtain line ratios for the 4713 $\AA$ and 4922 $\AA$ helium lines. Because of the differences

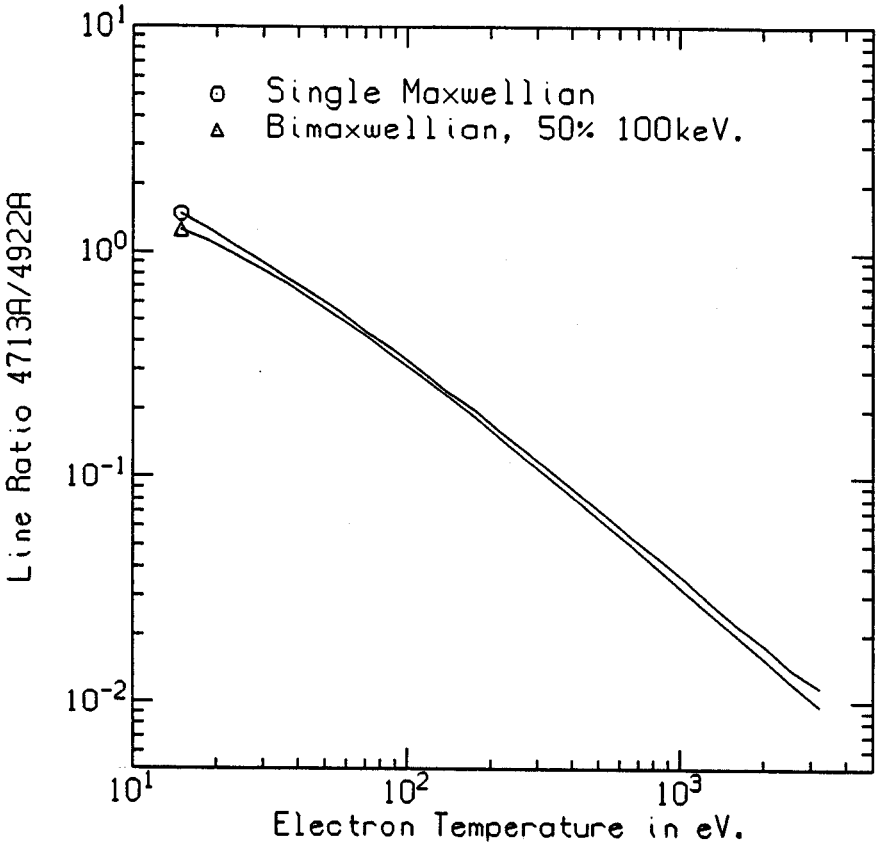

Figure A-3: The analytical expression for the helium line ratio produces this figure.

between the experimental and theoretical curves in Figures A-2(a) and (b), T_{ec} from [McWhirter, 1965] is approximately 60 percent that of Figure 3-1 or A-3.

A.2 Ionization

As discussed in Chapter 3, the conversion from brightness profile to ionization source profile requires the function I/P, the number of ionizations which occur for each photon emission. Figure 3-10 was derived from the ratio of excitation and ionization cross sections. As described in the previous section, two step processes in helium are not important for Constance parameters, allowing the calculation of Figure 3-10 from just two cross sections.

The situation in a hydrogen plasma is more complicated. Because hydrogen is

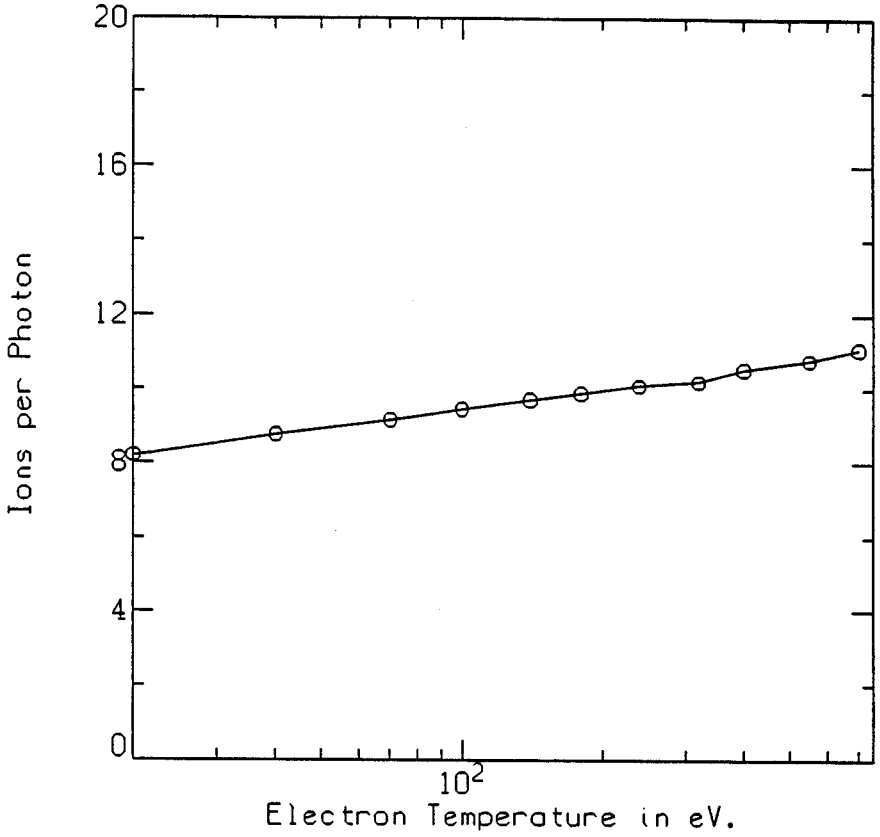

Figure A-4: Ionzations per photon in hydrogen is calculated by a code, incorporating the atomic processes shown in the previous figure.

diatomic, a variety of atomic processes have to be taken into account when calculating I/P. Figure A-4 shows the results of a code which includes the atomic cross sections for all the processes in Figure A-5. The code results agree with a similar calculation in the literature [Johnson and Hinov, 1969]. Figure A-5 is a diagram showing the various paths an H_2 molecule can follow on the way to ionization or excitation to the $n = 3$ state. (Emission of an H_α or L_α photon follows excitation to the $n = 3$ level, with a well known branching ratio.) The width of the arrows in Figure A-5 indicates the relative probability of each path, calculated at $T_{ec} = 100$ eV.

Argon is a simpler system than hydrogen because it is monatomic. The excitation cross section for the 6965 $\AA$ line, taken from [Zapesochnyi and Feltsan, 1965] is shown in Figure A-6. Combining Figure A-6 with the ionization cross section, results in the I/P function shown in Figure A-7.

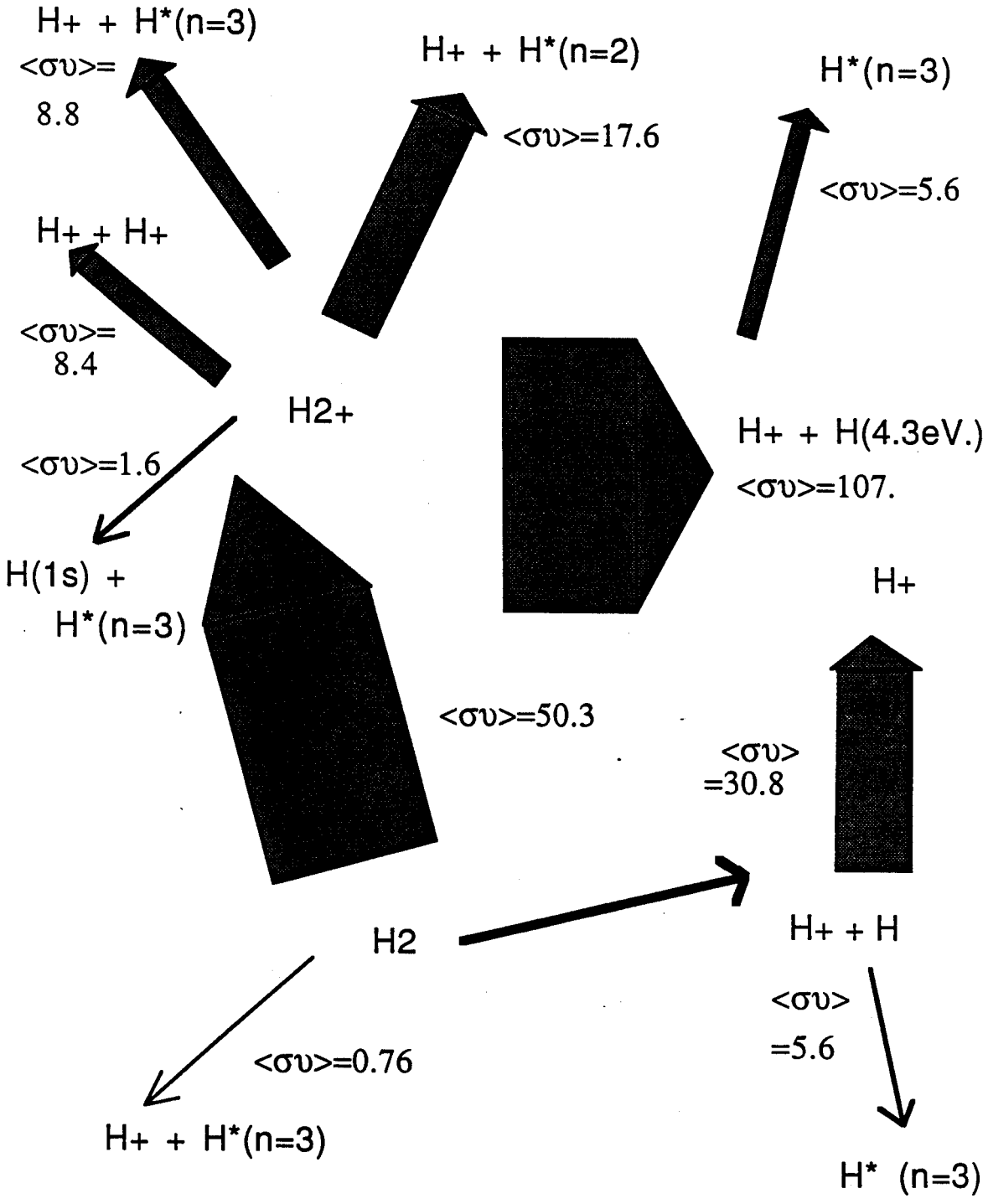

Figure A-5: Atomic processes in hydrogen are shown. The relative probability of a path is proportional to the arrow width.

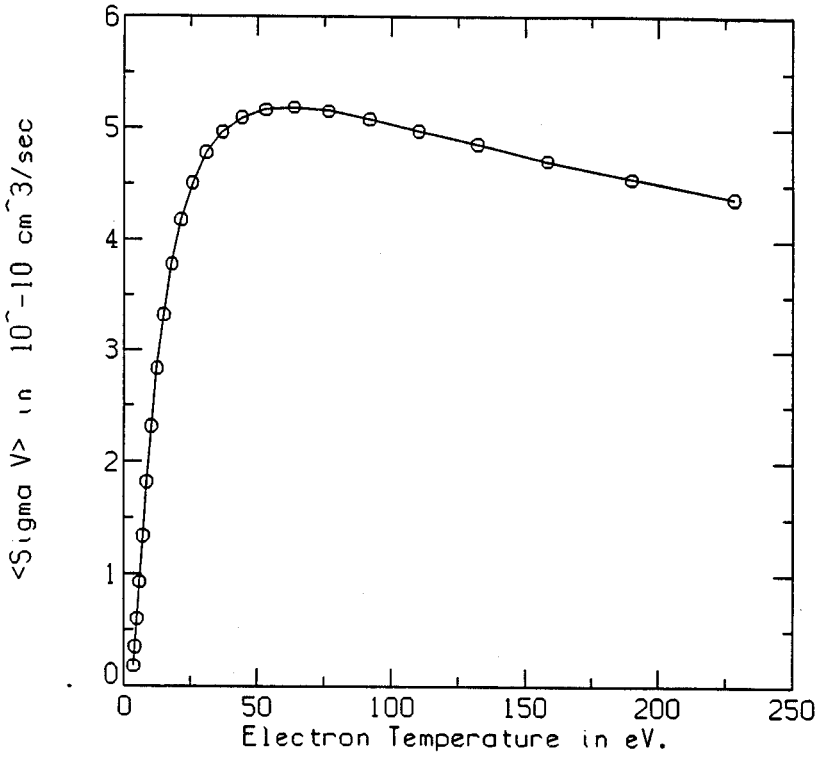

Figure A-6: Argon electron excitation cross section to produce a 6965 $\AA$ photon.

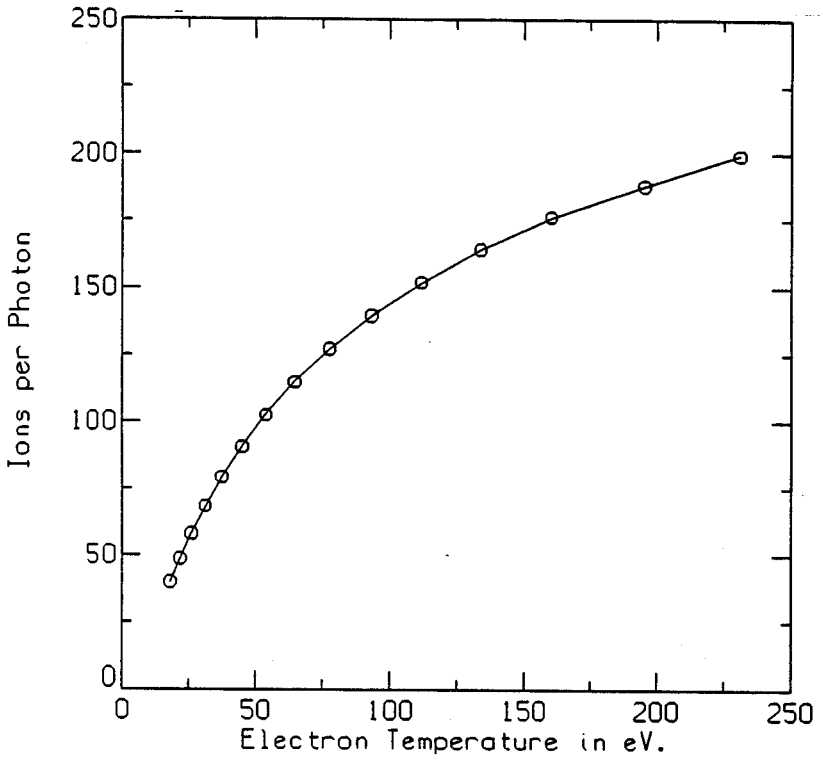

Figure A-7: Argon ionizations per 6965 $\AA$ photon.

Appendix B

Absolute Source Measurements

As discussed in Chapters 2, 3, and 5, the CCD camera was absolutely calibrated to allow an absolute measurement of the ionization source function. This appendix gives details about these absolute source measurements including the camera calibration method, an absolute source calculation and an error analysis.

B.1 Camera Calibration

The camera was calibrated at the three wavelengths used for source measurements in hydrogen, helium and argon plasmas. Figure B-1 shows the transmission as a function of wavelength for the 4922 $\AA$ (He^I line) filter used in both the T_{ec} and ionization source measurements. The filter has a 12.8 $\AA$ FWHM centered at 4924.2 $\AA$ as measured by the Optical Multichannel Analyzer (OMA). After the OMA dark count background is subtracted, the filter response is non–Gaussian with large wings. The effective width is:

$$\Delta\lambda_{eff} = F_{max}^{-1} \int F(\lambda)\, d\lambda = 16.0\AA \tag{B.1}$$

where $F(\lambda)$ is the filter transmission and F_{max} the peak transmission.

In doing the absolute calibration, the number of photons reaching the CCD camera

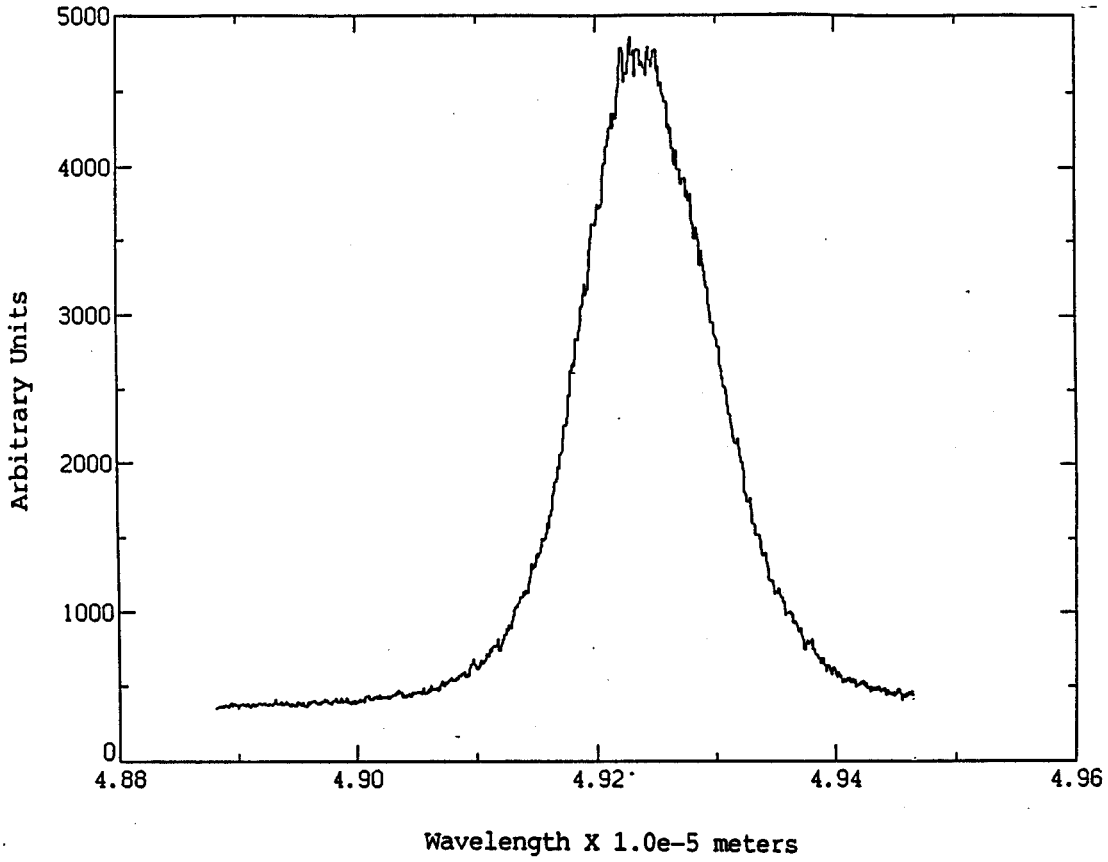

Figure B-1: Transmission of 4922 $\AA$ filter for helium source and density measurements.

from a standard calibrated tungsten lamp is:

$$N = T \int \frac{dE}{d\lambda} \frac{A\, d\Omega}{E_p(\lambda)} \frac{F(\lambda)\, d\lambda}{F_{max}} \tag{B.2}$$

where $dE/d\lambda$ is the lamp power intensity in μW/ster–mm^2–nm.

E_p is the photon energy at λ,

A is the tungsten filament area,

$d\Omega$ is the camera viewing solid angle, and

T is the transmittance at F_{max}, (approximately 50 percent).

The emission from the tungsten lamp $dE/d\lambda$ was taken from a calibration curve tracable to NBS.

Because the filter has a narrow pass band compared with the rate of change of

$dE/d\lambda$, we can approximate Equation B.2 as:

$$N = T\frac{dE(\lambda_0)}{d\lambda}\frac{A\,d\Omega}{E_p(\lambda_0)}\int\frac{F(\lambda)}{F_{max}}d\lambda = T\frac{dE(\lambda_0)}{d\lambda}\frac{A\,d\Omega}{E_p(\lambda_0)}\Delta\lambda_{eff} \tag{B.3}$$

For the 4922 $\mathring{A}$ filter, 1.34×10^9T photons cause a 3900 pixel–level CCD camera response. At 4921.93 $\mathring{A}$ (the actual He^I wavelength) the filter response is 0.92T, because the filter transmission maximum is not quite centered on the line. The factor of T cancels when we do the measurements, so we do not bother to measure T. Combining numbers, we find the value of 3.43×10^5 photons/pixel–level given in Table 2.1. Similar calculations give the other values in that table.

B.2 Total Source Calculation

For helium and argon plasmas at low back–fill pressure, the light intensity is too low to use the CCD camera directly. (In hydrogen the H_α line is so bright that the image intensifier is never needed.) An image intensifier is used to increase the light to observable levels. The light level as a function of back–fill pressure is measured using a photomultiplier tube and the visible transmission filter to calculate the gain of the image intensifier. This allows absolute source measurements at low light levels.

Figure B-2 shows the measured light level as a function of pressure for the 4922 $\mathring{A}$ helium line. The continuum background has already been subtracted for the data shown. The solid curve is the least square power law fit:

$$L = 0.025P^{0.98} \tag{B.4}$$

where P is in units of 10^{-7} Torr. and L in Volts. An exponent near one is expected because both n_e and $< \sigma v >_{exc}$ are fairly independent of pressure in the equation for the light emission rate:

$$L \propto n_e P < \sigma v >_{exc} \tag{B.5}$$

Thus if we measure light using the unassisted CCD camera at high pressure, we can scale the overall total light level to low pressure. For argon plasmas, the exponent in Equation B.4 for the 6965 $\mathring{A}$ line is 2.16.

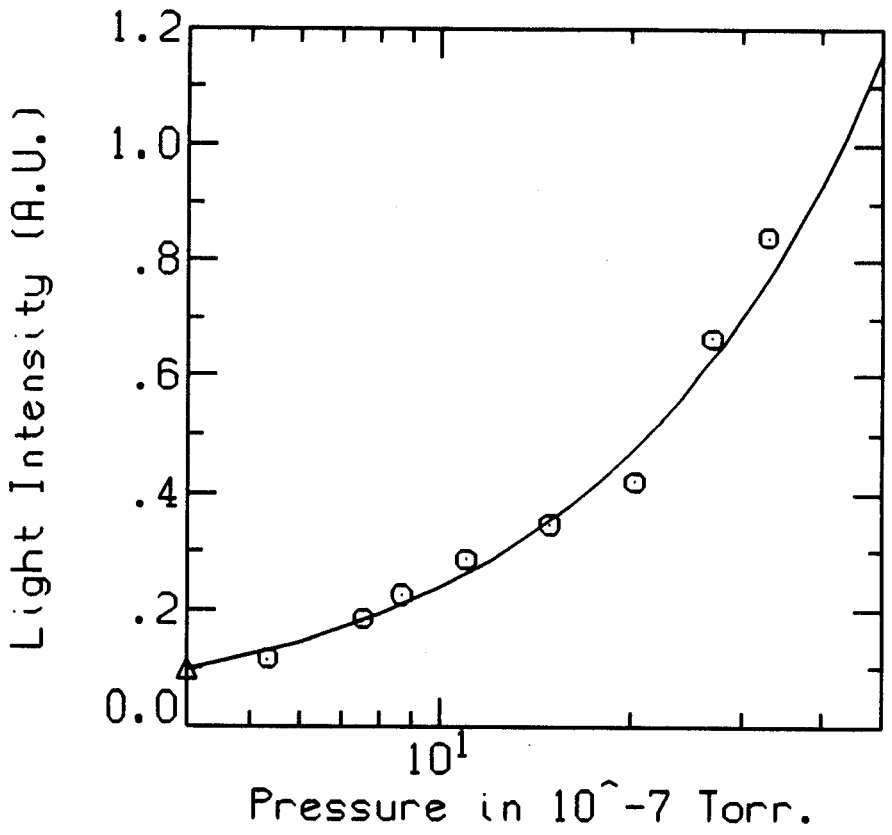

Figure B-2: Light Emission from a helium plasma at 4922 $\AA$ as a function of gauge pressure and a least square fit is shown.

One more factor needs to be computed before calculating the total ionization source. We define the average ionizations per photon $< I/P >$ as:

$$< I/P >= \frac{\int I/P(T_{ec})\, B(\psi)\, d\psi}{\int B(\psi)\, d\psi} \tag{B.6}$$

where $B(\psi)$ is the measured average brightness on the flux surface ψ. This definition allows us to correctly convert from the total camera response (in pixel-levels) to the total ionization source. Values of $< I/P >$ for our standard conditions in the three plasmas are shown in Table B.1.

As an example, the camera response to a high pressure shot ($P = 2.55 \times 10^{-6}$ Torr.) was integrated. The total camera response was 7.8×10^4 pixel-levels for the 200 ms integration time, with a solid angle of 7.65×10^{-5} ster. Standard operating conditions are a pressure of 5.0×10^{-7} Torr. Scaling the light level using Equation B.4,

Plasma	λ ($\AA$)	$< I/P >$
Hydrogen	6563. (H_α)	10.2
Helium	4922.	846.
Argon	6965.	183.

Table B.1: Average ionizations per photon are shown.

the response at low pressure is down by a factor of five. Combining these numbers with the value of $< I/P >$ from Table B.1, one finds 620 mA. total ionization source for helium under standard conditions. This is within 20 percent of the measured total integrated end loss.

Similar calculations for hydrogen and argon do not show this close agreement between absolutely measured ionization source and total end loss. In a hydrogen plasma, the measured source is a factor of two to three times smaller than the end loss, and in argon the result is another factor of three smaller. The reason for this discrepancy and its significance is described in the next section.

B.3 Error Analysis

The main source of uncertainty in the absolute source function measurement is in the absolute magnitude of the two or more cross sections required in calculating the number of ionizations per photon I/P. Knowledge of the absolute value of a cross section is much more difficult than that of its T_{ec} dependence. For example, in a hydrogen plasma the relative contribution of atoms and molecules to ionization adds uncertainty to I/P. The extremes of fueling completely via atoms to complete fueling by molecules cause I/P to range from 10 to 22. The flat shape of $I/P(T_{ec})$ is, however,

almost completely independent of the exact ionization path.

Measuring the absolute excitation cross section for the argon 4p (6965 $\mathring{A}$) line is very difficult. One author [Peterson and Allen, 1972] notes that inconsistencies exist between the two types of absolute cross section data for the 4p argon levels, and that the largest cross section reported in [Zapesochnyi and Feltsan, 1965] (and used in this thesis) is barely seen in the energy loss data. The measured shapes of these cross sections can be compared with theoretical predictions, and are in agreement.

The conclusion of this error analysis is that the close agreement between the measured source function and end loss in helium is fortuitous; a disparity of 50 percent would have been possible. The disagreement in hydrogen between measured absolute source function and end loss is explainable by uncertainties in atomic physics and plasma processes. The disagreement (by an order of magnitude) in argon probably implies an error in the absolute cross section for the 6965 $\mathring{A}$ line given in [Zapesochnyi and Feltsan, 1965].

The shapes of the cross sections are much better known, and lead to I/P profiles which although wrong in absolute magnitude, probably have the correct dependence on T_{ec}. Thus while it is not possible at this time to "prove" particle–balance ($\int (S - J)\, d\psi = 0$) using the absolute source measurement, once particle–balance is assumed, the shape of S and various transport calculations which follow can be calculated with some degree of confidence.

Bibliography

[Abramowitz and Stegun, 1970] Abramowitz, M. and Stegun, I. *Handbook of Mathematical Functions* Chapter 5, *Exponential Integrals*, National Bureau of Standards (1970).

[Allen, et al., 1987] Allen, S., Correll, D.L., Hill, D.N., Kaiser, T.B. and Heifetz, D.B., Nucl. Fusion *27* (1987) 2139.

[Baldwin, 1980] Baldwin, D.E., *Model for Ion Confinement in a Hot–Electron Tandem Mirror Anchor*, Lawrence Livermore Report UCID-18802 (1980)

[Bernstein, 1971] Bernstein, I.B. in *Advances in Plasma Physics*, Vol. 4., (Simon, A. and Thompson, W.B., Eds.), Wiley (1971) 311.

[Bevington, 1969] Bevington, P.R., *Data Reduction and Error Analysis for the Physical Sciences*, McGraw–Hill (1969)

[Braginskii, 1965] Braginskii, S.I. *Transport Processes in Plasmas* in *Reviews of Plasma Physics*, Vol. 1., (Leontovich, M.A., ed.), Consultants Bureau, N.Y. (1965) 283.

[Brau, et al., 1988] Brau, K., Irby, J.H., Sevillano, E., Casey, J.A., Golovator, S.N., Goodman, D.L., Horne, S. and Post, R.S., Nucl. Fusion Lett. (to be published)

[Chen, 1974] Chen, F.C., *Introduction to Plasma Physics*, Plenum Press, N.Y., (1974) 166.

[Chen, 1988] Chen, L., and Hammett, G.W., Nucl. Fusion *28* (1988) 389.

[X. Chen, 1988] Chen, X., Ph.D. dissertation, Dept. of Physics, M.I.T., reprinted as MIT Plasma Fusion Center Report PFC/RR–88–6, (1988).

[Cho, et al., 1986] Cho, T., Ichimura, M., Inutake, M., et al. IAEA Conf. on Plasma Phys. Cont. Nucl. Fusion, Kyoto, Japan, IAEA–CN–47/C–I–2 (1986) 243.

[Cohen, et al., 1983] Cohen, B.I., Cohen, R.H., and Rognlien, T.D., Phys. Fl. *26* (1983) 808.

[Cohen, et al., 1979] Cohen, R.H., Nucl. Fusion *19* (1979) 1579.

[Corrigan and von Engel, 1958] Corrigan, S.J.B. and von Engel, A. Proc. Phys. Soc. (London) 72 (1958) 786.

[Devoto, 1986] Devoto, S. *GCDRIFT Users Manual* (Unpublished Livermore Laboratories Memorandum) (1986) and private communication, 1989.

[Dimov, et al., 1976] Dimov, G.I., Zakaidakov, V.V., Kishinevskii, M.E., Sov. J. Plasma Phys. *2* (1976) 326.

[Drake, et al., 1982] Drake, R.P., Hooper, E.B., Jr., Karmendy, C.V, et al. Phys. Fl. *25* (1982) 2110.

[Ferron, et al., 1983] Ferron, J.R., Hershkowitz, N., Breun, R.A., Golovato, S.N. and Goulding, R., Phys. Rev. Lett. *51* (1983) 1955.

[Fowler, et al., 1977] Fowler, T.K., Logan, B.G., Comments Plasma Phys. Controll. Fusion *2* (1977) 167.

[Fredian and Stillerman, 1986] Fredian, T.W. and Stillerman, J.A., Rev. Sci. Instrum. *57* (1986) 1907.

[Fujimoto, 1978] Fujimoto, T., J. Quant. Spec. Radiat. Trans. *21* (1978) 439.

[Garner, 1986] Garner, R.C., Ph.D. dissertation, Dept. of Physics, M.I.T., reprinted as MIT Plasma Fusion Center Report PFC/RR–86–23, (1986).

[Goodman, et al., 1986] Goodman, D.L., Freidberg, J.P. and Lane, B., Phys. Fl. *29* (1986) 3365.

[Greenwald, et al., 1984] Greenwald, M., Gwinn, D., Milora, S., Parker, J., Parker, R., et al., Phys. Rev. Lett. *53* (1984) 352.

[Haste, et al., 1968] Haste, G.R., Dunlap, J.L., Lazar, N.H., et al., Oak Ridge National Lab Reports ORNL–TM–4401 (1968), ORNL–TM–4545 (1969) and ORNL–TM–4688 (1970).

[Hershkowitz, et al., 1985] Hershkowitz, N., Nelson, B.A., Johnson, J., Ferron, J.R., Persing, H., Chen, V., Golovato, S.N., Callen, J.D. and Woo, J., Phys. Rev. Lett. *55* (1985) 947.

[Hirshman and Sigmar, 1981] Hirshman, S.P. and Sigmar, D.J., Nucl. Fusion *21* (1981) 1079.

[Hokin, 1987] Hokin, S.A., Ph.D. dissertation, Dept. of Physics, M.I.T., reprinted as MIT Plasma Fusion Center Report PFC/RR–87–17, (1987).

[Hooper, et al., 1985] Hooper, B., Cohen, R.H., Correll, D.L., Gilmore, J.M., and Grubb, D.P., Phys. Fl. *28* (1985) 3609.

[Janev, et al., 1985] Janev, R.K., Langer W.D., Evans K., and Post, D.E.. *Atomic and Molecular Processes in Hydrogen–Helium Plas-*

mas Princeton Report PPPL–TM-358 (1985), also available as Springer–Verlag textbook (1988).

[Johnson and Hinov, 1969] Johnson, L.C. and Hinov, E., Phys. Rev. *187* (1969) 143.

[Kingston and Lauer, 1966] Kingston, A.E. and Lauer, J.E. Proc. Phys. Soc. *88* (1966) 597.

[Kuthi, et al., 1988] Kuthi, A., Olson, L., Lam, K.L., Zwi, H. and Wong, A.Y., Phys. Fl. *31* (1988) 1787.

[Lee, 1978] Lee, Y.C., Lawrence Livermore Report UCID-17992 (1978)

[Lees, 1932] Lees, J.H., Proc. Royal Soc. (London) *137* (1932) 173.

[Lieberman and Lichtenberg, 1983] Lieberman, A.J. and Lichtenberg, M.A., *Regular and Stochastic Motion*, Springer– Verlag (1983) Chapters 3 and 5.

[Liewer, 1985] Liewer, P.C., Nucl. Fusion *25* (1985) 543.

[Mauel, 1985] Mauel, M.E., Internal Laboratory Memorandum (1985).

[McWhirter, 1965] McWhirter, R., *Spectral Intensities* in Huddleston, R. and Leonard, S. *Plasma Diagnostic Techniques* Academic Press (1965)

[Myra and Catto, 1982] Myra, J.R. and Catto, P.J., Phys. Rev. Lett. *48* (1982) 620.

[Navratil, et al., 1979] Navratil, G.A. and Post, R.S., Comments Plasma Phys. *5* (1979) 29.

[Northrop, 1963] Northrop, T.G., *The Adiabatic Motion of Charged Particles*, Interscience (1963) Chapter 1.

[Okamura, 1986] Okamura, S., Nucl. Fusion *26* (1986) 1491.

[Parks, 1987] Parks, P.B., Phys. Fl. *30* (1987) 3212.

[Parks, 1988] Parks, P.B., Private Communication.

[Pastukhov, 1974] Pastukhov, V.P. Nucl. Fusion *14* (1974) 3.

[Persing, et al., 1988] Persing, H., Breun, R.A., Brouchous, D.A. and Wen, Y.J., Bull. Amer. Phys. Soc. *33* (1988) 1905.

[Peterson and Allen, 1972] Peterson, L.R. and Allen Jr., J.E., Jour. Chem. Phys. *56* (1972) 6068.

[Petrasso, et al., 1986] Petrasso, R.D., Sigmar, D.J., Wenzel, K.W., Hopf, J.E., Greenwald, M., Terry, J.L. and Parker, J., Phys. Rev. Lett. *57* (1986) 707.

[Petty, 1987] Petty, C.C., Rev. Sci. Instrum. *59* (1988) 601.

[Petty, 1988] Petty, C.C., Private Communication.

[Post, 1987] Post, R.S., Brau, K., Golovato, S., Sevillano, E., Smith, D.K., Guss, W., Irby, J., Myer, R. and Sullivan, J., Nucl. Fusion *27* (1987) 217.

[Putvinskij and Timofeev, 1975] Putvinskij, S.V., Timofeev, A.V. Zh. Ehskp. Teor. Fiz *69* (1975) 221.

[Riyopoulos, et al., 1986] Riyopoulos, T., Tajima, T., Hatori, T. and Pfirsch, D., Nucl. Fusion *26* (1986) 627.

[Rognlien and Cutler, 1980] Rognlien, T.H. and Cutler, T., Nucl. Fusion *20* (1980) 1003.

[Ryutov and Stupakov, 1978] Ryutov, D.D., and Stupakov, G.V., Sov. Phys. Dokl. *23* (1978) 412.

[Sackett, 1978] Sackett, S.J., Lawrence Livermore National Laboratory Report UCRF–52402 (1978).

[Simonen, et al., 1984] Simonen, T.C., Allen, S.L., Baldwin, D.E., et al. in Plas. Phys. and Contrl. Nucl. Fusion Res. (1984) (*Proc 10th Int. Conf. London, 1984*) Vol. 2, IAEA Vienna (1985) 255.

[Smith, et al., 1986] Smith, D.K., Brau K., Goodrich P., et al., Phys. Fl. *29* (1986) 902.

[Tsushima, et al., 1986] Tsushima, A., Mieno, T., Oertl, M., Hatakeyama, R., and Sato N., Phys. Rev. Lett. *56* (1986) 1815.

[Watari, et al., 1978] Watari, T., Hatori, T., Kumazawa, R., et al., Phys. Fl. *21* (1978) 2076.

[Whang and Morales, 1983] Whang, J., and Morales, R., Nucl. Fusion *23* (1983) 481.

[Zapesochnyi and Feltsan, 1965] Zapesochnyi, I.P. and Feltsan, P.V., Opt. Spektrosk. *20* (1965) 521. [Opt. Spectrosc.] *20* (1966) 291.

[Zhil'tsov, et al., 1979] Zhil'tsov, V.A., Kosarev, P.M., Likhtenshtejn, V.Kh., Panov, D.A., Skovoroda, A.A. and Shcherbakov, A.G., IAEA Conf. on Plasma Phys. Cont. Nucl. Fusion, Innsbruck 1978, IAEA–CN–37/S–2 (1979) 469.